TEMPERATURE DEPENDENCE OF RESISTIVITY AND HALL COEFFICIENT IN Cu$_2$ZnSnS$_4$ ABSORBERS FOR THIN FILM SOLAR CELLS

A Thesis Submitted to
the Graduate School of Engineering and Sciences of
İzmir Institute of Technology
in Partial Fulfillment of the Requirements for the Degree of

MASTER OF SCIENCE

in Department of Physics

by
Fatime Gülşah AKÇA

July, 2017
İZMİR

We approve the thesis of **Fatime Gülşah AKÇA**

Examining Committee Members:

_____

Assoc. Prof. Dr. Gülnur AYGÜN ÖZYÜZER
Department of Physics, İzmir Institute of Technology

_____

Prof. Dr. Mustafa EROL
Department of Physics Education, Dokuz Eylül University

_____

Assist. Prof. Dr. Enver TARHAN
Department of Physics, İzmir Institute of Technology

14 July 2017

_____   _____

Assoc. Prof. Dr. Gülnur AYGÜN ÖZYÜZER   **Prof. Dr. Lütfi ÖZYÜZER**
Supervisor, Department of Physics,   Co-adviser Department of Physics,
İzmir Institute of Technology   İzmir Institute of Technology

_____   _____

Prof. Dr. R. Tuğrul SENGER   **Prof. Dr. Aysun SOFUOĞLU**
Head of the Department of Physics   Dean of the Graduate School of
       Engineering and Sciences

ACKNOWLEDGEMENT

ABSTRACT

TEMPERATURE DEPENDENCE OF RESISTIVITY AND HALL COEFFICIENT in Cu_2ZnSnS_4 ABSORBERS for THIN FILM SOLAR CELLS

Solar energy is the most powerful clean energy source to act on the current energy needing all over the world. The utilization of green energy systems should be promoted since these energy systems benefit consumers, industry and the environment effectively for the developing countries. This advancement can be solely achieved if renewable energy sources become more accessible. It means that not only cheaper but also handy clean energy systems are needed. In spite of relatively high efficiency obtained by using c-Si, Si solar modules require high budget for manufacturing. The high production cost of c-Si, PV industry is lead to search for cheaper candidate materials like Cu_2ZnSnS_4 (CZTS) as absorber layer in solar cells.

The aim of the thesis is to investigate electrical properties of CZTS p-type intrinsic semiconductor compound on soda lime glass substrates, including the temperature dependent electrical conductivity, carrier concentrations and mobility extracted from Hall Effect measurements. Firstly, the metal precursor films were fabricated in multi-target sputtering system, then they were sulfurized inside the tubular furnace in order to obtain the CZTS compound.

X-ray diffraction and Raman spectroscopy measurements revealed the formation of kesterite structure. A good crystallinity and grain compactness of the films were determined by scanning electron microscopy (SEM). Electrical properties were measured by van der Pauw techniques. Hall effect measurements showed the p-type semiconductor behavior for all samples at room temperature. Also, optical properties including absorption coefficient, spectral transmission, and optical band gap were determined to characterize CZTS thin films.

ÖZET

İNCE FİLM GÜNEŞ HÜCRELERİ için Cu_2ZnSnS_4 ABSORBLAYICILARINDA ÖZDİRENÇ VE HALL KATSAYISININ SICAKLIĞA BAĞLILIĞI

Güneş enerjisi, tüm dünyanın ihtiyaç duyduğu mevcut enerjiyi harekete geçirmek için en güçlü ve temiz enerji kaynağıdır. Yeşil enerji sistemlerinin kullanılması teşvik edilmelidir, çünkü bu sistemler gelişmekte olan ülkeler için tüketicilere, sanayiye ve çevreye etkili bir şekilde yarar sağlayacaktır. Bu ilerleme yalnızca yenilenebilir enerji kaynakları daha ulaşılabilir hale gelirse başarılabilir. Bu, ucuz ve kullanışlı temiz enerji sistemlerine ihtiyaç duyulduğu anlamına gelir. C-Si kullanılarak nispeten yüksek bir verim elde edilmesine rağmen, Si güneş modülleri üretimi için yüksek bütçeye ihtiyaç duyulmaktadır. c-Si 'nin yüksek üretim maliyeti, PV endüstrisi Cu_2ZnSnS_4 (CZTS) gibi soğurucu tabaka olarak daha ucuz aday malzemeleri aramaktadır.

Tezin amacı, soda lime cam alttaş üzerine CZTS p-tipi yarıiletken bileşiğinin, Hall Etkisi ölçümlerinden yararlanılarak sıcaklığa bağlı elektriksel iletkenlik, taşıyıcı konsantrasyonlar ve hareketlilik dâhil olmak üzere elektriksel özellikleri incelemektir. Bu çalışmada ilk olarak filmler, çoklu hedef saçtırma sisteminde büyütüldü ve daha sonra bunlar sülfürleme sistemi ile büyütme tamamlandı.

X-ışını kırınımı ve Raman spektroskopisi ölçümleri, kesterit yapının oluşumunu ortaya koymuştur. Filmin iyi bir kristallenme ve tane yoğunluğu, taramalı elektron mikroskopisi ile gözlemlendi. Elektriksel özellikleri van der Pauw tekniği ile hesaplanmıştır. Hall etkisi ölçümleri, tüm örneklerin p-tipi yarıiletken özelliği göstermiştir. Ayrıca, soğurma katsayısını, spektral iletimini ve optik bant boşluğunu içeren optik özellikleri CZTS ince filmler karakterize etmek için belirlenmiştir.

To My Family …

TABLE OF CONTENTS

LIST of FIGURES

LIST of TABLES

CHAPTER 1

INTRODUCTION

Energy economy of nearly all countries especially the industrialized countries is based on the stored energy which is mainly fossil energy in the form of coal, oil and natural gas, likewise nuclear energy in the form of the uranium isotope U^{235} (Wurfel, 2005). Fossil fuels which have fundamental reserves release harmful gases to the atmosphere and this causes the climate changes and air pollution. As a result of this, ecosystem is in danger. For that reason, the use of this energy resources should be restricted. As is known, the result of the gather of carbon-based gases in the atmosphere causes earth warming which is known as the greenhouse effect. An effect like global warming can cause fatal consequences that lead to detrimental losses for nature and living area (Rai, 2002). When it comes to nuclear power, the biggest drawback for this energy source is the permanent damages for both humanity and the environment because of nuclear explosions.

Lots of countries have altered their focus from conventional energy sources to renewable energy sources such as solar, wind, geothermal, biomass and hydropower. Among the other renewable energy sources, solar energy has capacity to be scaled up to supply terawatts of electricity consumed by the world. The sun sends the electromagnetic radiation to the earth and this energy is about 120,000 TW. 0.16 % of the world's land with 10 % efficient solar conversion systems would supply 20 TW of power, which is almost twice the world's present consumption rate of fossil energy (Mkavi et al., 2013). Besides the unlimited amount of energy possessed by the sun, solar panels are used in rural areas, as well as in space applications such as spacecraft. Therefore, solar energy applications has more advantage than other renewable energy sources (King et al., 2002) (Figure 1.1).
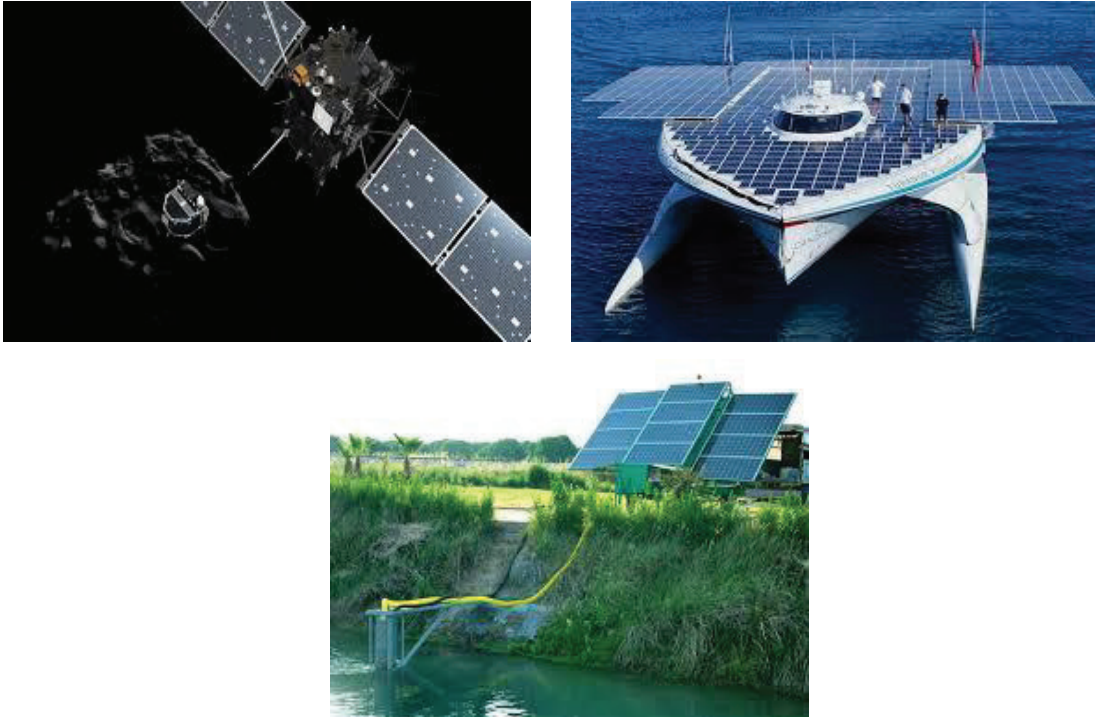
Figure 1.1. The use of solar application on different areas

Compared with consumption of annual global energy, the amount of energy can be learned. With this point of view, world energy consumption (from 1990 to 2040 years) can be seen for the member countries of Organization for Economic Cooperation and Development (OECD) and outside of nations the OECD (non-OECD) in Figure 1.2. There are changes of energy consumption between 2000 and 2010 as 114 quadrillion Btu (410 quadrillion Btu in 2000 and 524 quadrillion Btu in 2010) and anticipated along this view increasing is to 630 quadrillion Btu in 2020 and 820 quadrillion Btu in 2040 (quadrillion btu is equal about 1.056×10^{18} joules). In conclusion, we can infer that solely 0.01% of the annual solar energy which is reaching Earth could provide the all world's energy needed.
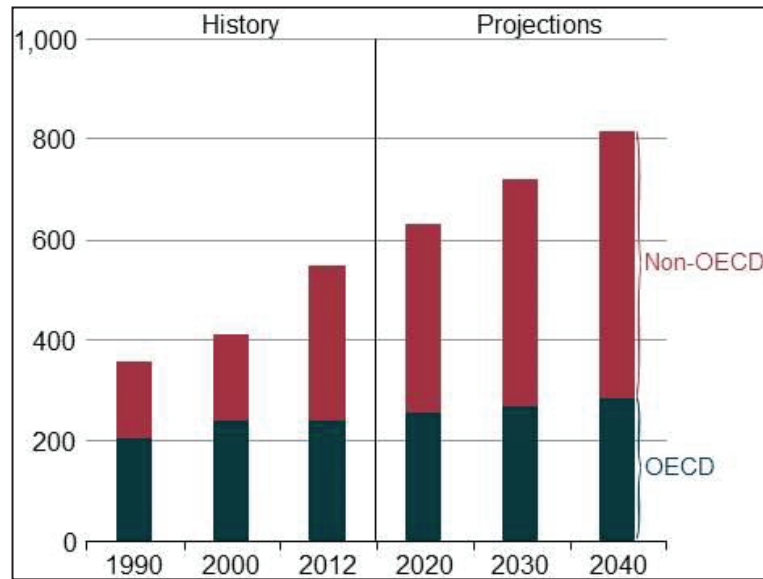
Figure 1.2. World energy consumption, 1990-2040
(Source: International Energy Outlook 2016)

In addition, not all solar radiation can absorbed by the earth unfortunately, because some solar radiations are missed till reaching the Earth, for instance 30% of solar radiation is reflected to space and 20% of them are absorbed by clouds. Nonetheless, 0.1% of them can sufficient to provide the energy necessity in the world if just 10% of them are usable. There are cheaper and practical energy systems that are necessity to provide the energy demand of world as an innocuous and cost competitive way. Through many ways, solar power is more preferable than other energy sources as an economic and powerful one. There are some benefits to use renewable energy, such as to cut the emission of greenhouse and less addicted to received energy. Additionally, novelty of technology can be induced by augmenting the renewable energy industry. Although there are many different kinds of renewable energy resources, some of them have boundaries that are hydropower, wind and geothermal energy. Among them, solar photovoltaic (PV) can be accepted as the most promising energy system, which has a possibility to backup for fossil energy.

This thesis is related to almost new compound semiconductor material for use in PV energy systems. Cu_2ZnSnS_4 (I-II-IV-VI group semiconductor compound), which is abbreviated to 'CZTS', is almost newly explored material which have been in development for PV energy systems since the 1970s (Luque, 2003), and have reached mass production in recent years. The aims of this thesis are to using magnetron sputtering technique for fabricated all CZTS thin films, observe the effect of temperature on

3

electrical properties, investigate the effect of crystalline structure on electrical properties and investigate the effect of sulfurization duration time and precursor stacking on the opto-electronic properties of CZTS films. The contribution of this study to the literature can be considered as follows. At low temperatures, how the effect of temperature on electrical properties and to examine contributing of it to physics. Hence, it can provide information about the opto-electrical characteristics of solar cells located on the satellite.

1.1. Thin film photovoltaics

In the thin film solar cell, even if the used semiconductor materials change, the structure and working principle of solar cell are similar. Figure 1.3 demonstrates layer orders and the types of layers in the cross- section of the thin film solar cell.

Metal Grid	
AZO	250 nm
ZnO	80 nm
CdS	70 nm
CIGS/CZTS	1-2 um
Mo	750 nm
Glass	3 mm
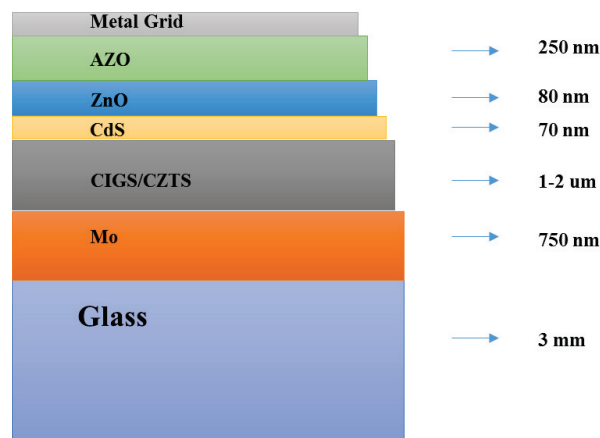
Figure 1.3. Layer orders in the cross-section of thin film solar cell

The important layer in the solar cells is absorber layer which provides being the electron-hole pairs. Si, $Cu(In,Ga)Se_2$ (CIGS), CdTe, CZTS and CZTS(e) are the main semiconductor compound materials used as the absorber layer. Among these layer, although the thin film solar cells based on Si are high efficient cells, it has a disadvantage. Si is indirect bandgap semiconductor, so the absorption coefficient near its band edge is low. On the other hand, the thin film solar cells based on CIGS and CdTe have recently demonstrated to have the highest efficiencies 20.8% (Jackson et al., 2014) and 20.4% (First Solar Press Release, 2014), respectively. These materials include indium and tellurium and which have limited reserve and they are toxic elements. As a result, in the recent studies, researchers prefer semiconductor CZTS for including the non-toxic and

earth-abundant element. The following layer is buffer layer in solar cell. In the thin film solar cell based on CZTS absorber layer, generally have been used CdS as buffer layer. The buffer layer assumes to complete p-n junction, as well as, to protect the absorber layer from damage like shunting due to the deposition of other layer. The next layer is i:ZnO which is the supporter layer for buffer layer. That is, this layer increases the shunt resistance. Finally, an n-type transparent window layer is deposited like Al doped ZnO (AZO). Therefore, p-n junction is completed with window layer.

1.2. Cu_2ZnSnS_4 (CZTS): properties, history and device efficiencies

The CZTS layer is an absorbing layer which is the result of displacement the CIGS absorber layer by the two group IIIA elements (In or Ga) by one Zn and one Sn atoms (Figure 1.4) (Lewerenz and Jungblut, 1995).
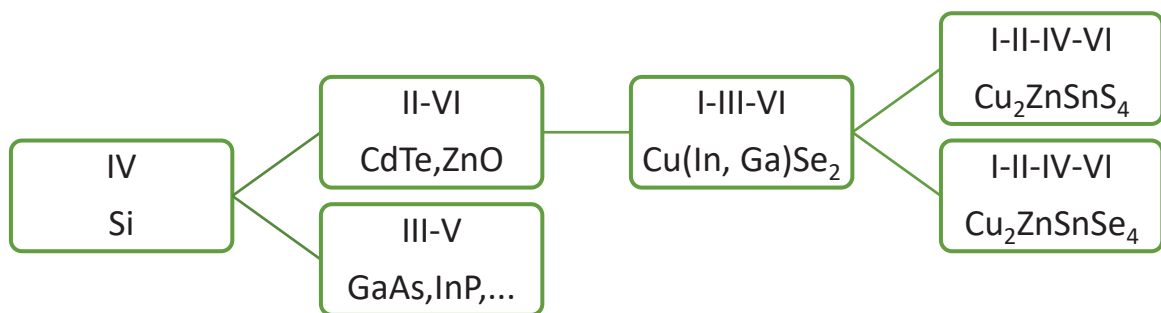
Figure 1.4. New absorber layers obtained with the displacement of elements

Therefore, it can be clearly seen that the properties of CZTS and CIGS materials are similar. CZTS has high band-gap energy around 1.5 eV, a large absorption coefficient ($\geq 10^4$ cm^{-1}) in the visible range of spectrum (Riha et al., 2009). CZTS is a self-doped p-type semiconductor compound which is referred to as kesterite structure (space group 14) (Figure 1.5).
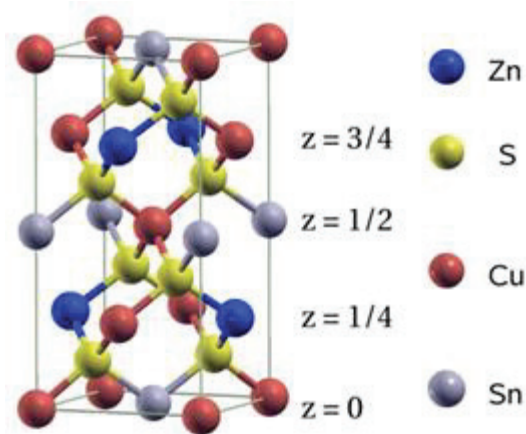
Figure 1.5. Kesterite crystal structure
(Source: Morales-Acevedo, 2013)

Figure 1.6. is shown a ternary phase diagram. This ternary phase diagram was developed (Scragg, 2010) by using the based on the research by Olekseyuk et al. (Olekseyuk et al., 2004). Despite of the fact that CZTS is a quaternary compound, by assuming to always get right amount of sulfur in samples, the phase diagram can be degraded to three constituent (Flammersberger, 2010).
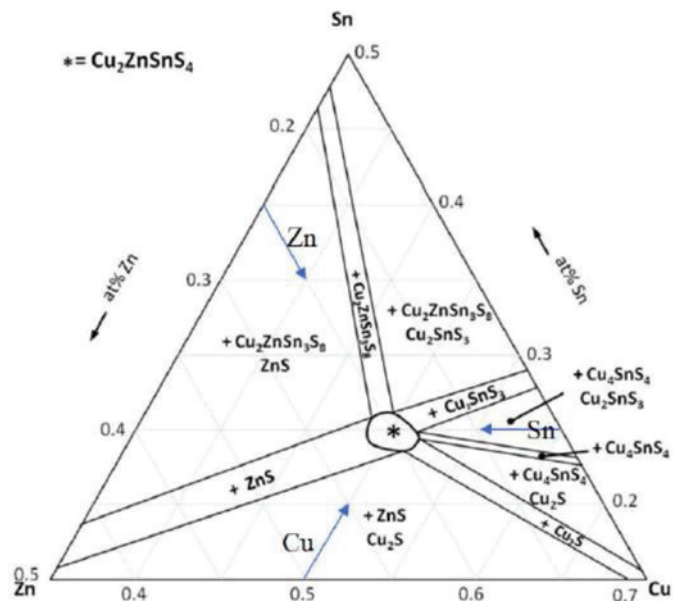
Figure 1.6. Ternary phase diagram of CZTS
(Source: Scragg, 2010)

This diagram describes that each field represents CZTS formation addition to the related second phase formation, depending the atomic composition of associated with element. In this diagram, there are ten field which shows the feasibility of second phase formation is high. The eleventh region in the middle, which is marked with a star, is where the pure CZTS formation is possible.

According to Shockley–Queisser theoretical calculations, approximately 32.4% maximum solar conversion efficiency is expected from CZTS solar cells (Shockley and Queisser, 1961). Despite having such high theoretical content, the maximum efficiency to 9.6% was measured from the CZTS layer produced by using elemental sulfur in laboratory conditions (Kato et al., 2012). The maximum efficiency of $Cu_2ZnSn(S, Se)_4$ (CZTS (e)) produced using sulfur and selenium together is about 12.6% (Wang et al., 2014). It means that more research is needed to be done with this newly explored material to improve its higher efficiency.

CHAPTER 2

THEORETICAL CONSIDERATION

In chapter 1, we had information about solar cell. In this chapter, we will discuss theoretical consideration based on solar cell after information of semiconductor behavior. A solar cell is device that converts solar radiant energy directly into electrical energy. Sunlight shining on the solar cell produces both a current and a voltage to generate electric power. This process requires firstly, when photon with energy equal to or higher than band gap of the solar cell semiconductor is absorbed, consequently electrons in the semiconductor become excited and they promote from valence band (E_v) to conduction band (E_c). Therefore, it is leaving a free space (hole) in the valence band and electron-hole pair is created. However, electrons in the p-type material, and holes in the n-type material are meta-stable and will only exist, on average, for a length of time equal to the minority carrier lifetime before they recombine. If the carrier recombines, then the light-generated electron-hole pair is lost and no current or power can be generated.

2.1. Material Types

2.1.1. Conductors

The electrons in the conductor material flow easily because there is no resistivity against to electron motion. Metals are very good conductor because the energy level between the conduction and valance band is very close and in most cases the conduction and valance band is overlapped.

2.1.2. Insulators

Insulator which is a material opposed to conductor due to the fact that it is generally made of nonmetals that have very few or no free electron and has very high band gap between conduction and valance band which is in the range of 4 - 5.5 eV.

2.1.3. Semiconductors

Semiconductors are divided into two groups that are elemental and compound semiconductors. Elemental semiconductors are comprised from group 4A elements, whereas compound semiconductor consists of combinations of group 3-5A and group 2-6A elements. As you can see from Table 2.1, there are many elements and compounds as an example of mostly used semiconductor materials.

Table 2.1. List of some semiconductor materials

Elemental Semiconductors	
Si	Silicon
Ge	Germanium
Compound Semiconductors	
AlP	Aluminum phosphide
AlAs	Aluminum arsenide
GaAs	Gallium phosphide
InP	Indium phosphide
ZnO	Zinc oxide
ZnS	Zinc sulfide
CdSe	Cadmium selenide
CdTe	Cadmium telluride

Table 2.2. A portion of the periodic table

1A	2A	3A	4A	5A	6A
		B	C	N	O
		Al	Si	P	S
Cu	Zn	Ga	Ge	As	Se
Ag	Cd	In	Sn	Sb	Te
Au	Hg				
...	...				

Elemental semiconductors, group 4A, have diamond crystal structure. Among these, silicon is the most commonly used in microelectronics as indirect band gap

semiconductor. The reason for that, Si atom has four valance electrons for bonding and others are bound to the nucleus. Si atom has four chemical bonds and each four atom has two electrons which bond is called covalent bonding that refers to share the electrons in atoms. This type atomic bond likes as closed valance energy shell similar to hydrogen molecule. There is an important difference between the bonding of hydrogen and elemental semiconductor is that, hydrogen molecule is shaped like no additional electron to more bond, whereas silicon atoms shape to have additional bonds via present valance electrons. For silicon, four nearest neighbors are formed the covalent bonds, conform to the tetrahedral crystal and the diamond structure.

It is possible to produce an alloy mixing semiconductors. Zinc blende (sphalerite) or wurtzite structure are crystallized in binary compound direct band gap semiconductors. The zinc blende structure differs from the diamond structure because of two different atoms in the lattice.

There is a way to form the ternary (three-element) or more complex quaternary (four-element) semiconductor compounds supplying flexibility with using different elements. $Ga_x In_{1-x} As$, subscript shows the fraction of the lower atomic number element component, can be given as an example. Additively, Vegards's law can be calculated as shown in equation 2.1. In this equation, A and B refer to two semiconductors with the lattice constant a_A and a_B by the lattice constant of an alloy $A_x B_{1-x}$.

$$a_{all} = xa_A + (1-x)a_B \qquad (2.1)$$

All semiconducting materials have their own unique band structure. Schrödinger equation solution for an electron in a semiconductor crystal give the energy versus effective momentum relation (E-k relation). In a semiconductor lattice, the E-k diagram that represents the range of energy and momentum that an electron within a crystal lattice can have (Figure 2.1) describes the states of electron and hole.

In semiconductor physics, the band gap of a semiconductor is always one of two types, a direct band gap or an indirect band gap. The minimal-energy state in the conduction band and the maximal-energy state in the valence band are each characterized by a certain crystal momentum (k-vector) in the Brillouin zone. If the k-vectors are the same, it is called a "direct gap". If they are different, it is called an "indirect gap". The band gap is called "direct" if the momentum of electrons and holes is the same in both the

conduction band and the valence band; an electron can directly emit a photon. In an "indirect" gap, a photon cannot be emitted because the electron must pass through an intermediate state and transfer momentum to the crystal lattice.
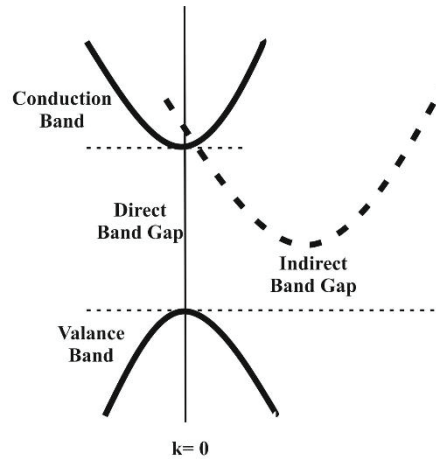
Figure 2.1. The valance band, direct band gap and indirect band gap conductions as schematic representation

A photon of energy E_g can produce an electron-hole pair for a direct band gap, because the electron does not need to be given very much momentum. Moreover, an electron must also pass a significant change in its momentum for a photon of energy E_g to produce an electron-hole pair for an indirect band gap. For this is possible, it requires like an electron to interact not only with the photon to gain energy, but also with a lattice vibration called a phonon in order to either gain or lose momentum.

It requires three entities to interrupt such as an electron, a photon and a phonon for indirect process. This is similar to chemical reactions, where, in a particular reaction step, a reaction between two molecules will proceed at a much greater rate than a process which involves three molecules.

Direct band gap compound semiconductor materials have preferable properties. Because the direct band gap ensures good optical and better electron transport in the conduction band.

2.1.3.1. Mobile Carriers: Intrinsic Carriers

There is no current flow in semiconductors because of filled valance band and empty conduction band. In addition to this, electron transportation could happen the holes

11

which are created in the valance band. Like this, in conduction band, current is flowed by electrons which are called mobile carriers. Mobile carrier density is calculated as the total of p and n, p is the holes density in the valance band and n is the density of electrons in the conduction band.

There are two ways to place mobile carriers into valance conduction or valance band. The thermal energy is enough for dislodging an electron from valance band to conduction band for exciting at above the absolute zero kelvin in pure semiconductors that are formed as electron-hole pair. Additionally, mobile carriers can be created by the formed crystallographic defects.

A n_i and p_i (i refers to intrinsic) refer to pure semiconductor electron and hole density, respectively. The conduction band contains the holes and valance band contains the intrinsic carrier concentrations (electrons). In conduction band, intrinsic carrier concentration is a function of the band gap and temperature. *N(E)* refers to the density of state (DOS) number of states per unit volume in addition to $N_C(E)$, $N_v(E)$ refers to energy for conduction and valance band, respectively.

The energies at close to extrema points of conduction and valance band, DOS has a quadratic E dependence (Figure 2.2 (a)). The electrons' concentration in the conduction band is,

$$n = \int_{E_C}^{\infty} N_e(E) f(E) dE \tag{2.2}$$

N_e *(E)* refers to the electron density near to the conduction band edge and *f(E)* refers to the Fermi function.
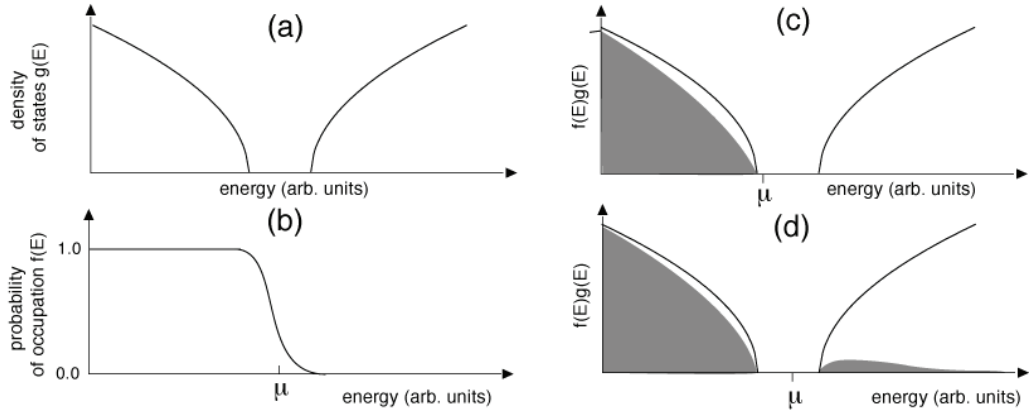
Figure 2.2. a) Schematic drawing density of states for a semiconductor. (b) Fermi-Dirac distribution. (c) Occupied density of states (grey area) for the chemical potential only above the valence band maximum. (d) Occupied density of states for the chemical potential close to the middle of the gap. Note that the temperature in (c) and (d) is much higher than room temperature to make the existence of excited carriers visible.

It is possible to calculate the conduction band DOS from equation (2.2) by using appropriate expressions,

$$n = \frac{1}{2\pi^2}\left(\frac{2m_e^*}{\hbar^2}\right)^{3/2} \int_{E_C}^{\infty} \frac{(E-E_C)^{1/2}}{\exp\left(\frac{E-E_F}{k_BT}\right)+1} \tag{2.3}$$

$$= 2\left(\frac{m_e^* k_B T}{2\pi\hbar^2}\right)^{3/2} exp[(E_F - E_C)/k_B T] \tag{2.4}$$

The terms in the denominator can be neglected when Fermi level is far from band edge, which is called as Boltzmann approximation. It is valid for n is small enough ($<10^{17}$ cm^{-3}) and obtain,

$$n = N_C exp[(E_F - E_C)/k_B T] \tag{2.5}$$

N_C refers to the DOS at the conduction band edge,

$$N_C = 2\left(\frac{m_e^* k_B T}{2\pi\hbar^2}\right)^{3/2} \tag{2.6}$$

We can calculate the valance band DOS using same approximation (E_F-E $\gg$ k_BT) with the same mathematical calculation,

$$p = 2\left(\frac{m_h^* k_B T}{2\pi\hbar^2}\right)^{3/2} exp[(E_V - E_F)/k_B T] \tag{2.7}$$

$$= N_V exp[(E_V - E_F)/k_B T] \tag{2.8}$$

$$N_V = 2\left(\frac{m_h^* k_B T}{2\pi\hbar^2}\right)^{3/2} \tag{2.9}$$

N_V refers to the DOS at the valance band edge.

As mentioned above, hole concentration is equal to the electron concentration in intrinsic semiconductors. When multiply the n and p, equation 2.10 is reached.

$$np = 4\left(\frac{k_B T}{2\pi\hbar^2}\right)^3 \left(m_e^* m_h^*\right)^{3/2} exp\left(-E_g/k_B T\right) \tag{2.10}$$

When the band gap decreases, the carrier concentration increases exponentially as dependent on the temperature. As a result of independent of the position of the Fermi level, which is called, as the law of mass action, it can be seen in eq. 2.10. In this case, n is increased with decreasing p and vice versa.

Fermi level position can be attained when n=p,

$$E_{Fi} = \frac{E_C + E_V}{2} + \frac{3}{4} k_B T ln \left(m_h^*/m_e^*\right) \tag{2.11}$$

The Fermi level become closer to the mid gap for intrinsic semiconductors as seen in Equation 2.10.

2.1.3.2. Doping: Extrinsic Carriers

Introducing impurity atoms can change pure semiconductor electron and hole density. Electron transformation happens with this way. Electrical properties of the semiconductors can be modified by impurity atoms and it is possible to make proper

integrated electronic circuits (transistors, detectors, diodes etc.) with these atoms. Donor and acceptor are the kinds of dopants atoms. Donor is explained as impurity atoms donate an electron from valance band to the conduction band and called as n-type semiconducting. Besides, acceptor is explained as atoms accept an electron from the valance band and there is occurred hole in the valance band that p-type semiconducting happened.

For elemental semiconductors; P, As and Sb (group V) elements, B, Al, Ga element are example for n type and p type impurities, respectively. For example, considering the GaAs compound semiconductor, it should be doping elements from group VI in order to group V element As for n-type GaAs. Extra electron in the compound and n type conductivity can be provided by this way. In a similar way, group III element Ga change place with group II element as acts like acceptor.

If focus on pentavalent (donor) atom doping in Si, donor atom's outer electrons bond to s Si atom, then other fifth electrons are positively charged ion to attracted which is called coulombic attraction. This attraction is substitute for the dielectric constant of the material.

Doping atom in Si is the solution for the lowest energy,

$$E_d = E_C - \frac{e^4 m_e^*}{2(4\pi\varepsilon)^2 \hbar^2}$$
(2.12)

E_d, ε refer to donor energy level dielectric constant, respectively.
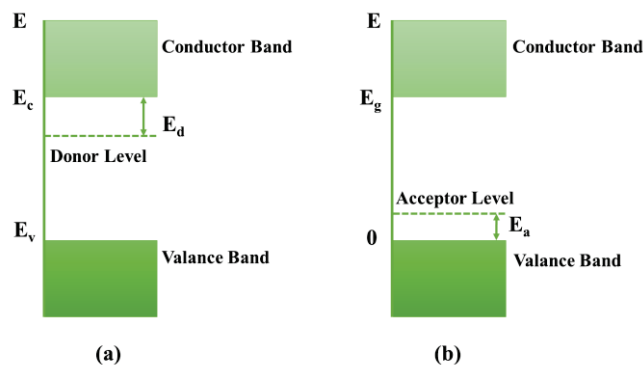
Figure 2.3. Schematic description of (a) donor level, (b) acceptor level

Fig 2.3(a) shows the ground state and energy level of material, which is measured from this band edge. Additionally, Figure 2.3(b) shows the acceptor impurity doping of the band diagram that in host semiconductor.

2.1.3.3. p-type and n-type Semiconductors

Type and concentration of impurities determine the semiconductor conductivity. There are two impurity, donor and acceptor, depends on the position of the atoms in the band gap. If electron donate to the conduction band, it is called as donor whereas if electron accept the electron from valance band, it is called as acceptors, which creates a holes. Hence, doped and ionized semiconductors include free charge carriers. N-type semiconductor is that ionizers supply the free electron in a semiconductor whereas p-type semiconductors is that ionizers include free holes in a semiconductor.

2.2. Performance parameters of a solar cell

In order to characterize a solar cell, we have to consider some parameters. As an example; short circuit current from I-V measurement belong to solar cell, solar cell efficiency etc. These parameters will be summarized in this chapter.

2.2.1. Characteristic of Current-Voltage

Firstly we have to consider a simple I-V characteristic of diode in order to understand I-V characteristic of a solar cell. Diode can be produced by taking ohmic contact from p-n junction each side. I-V characteristic of a diode is given below. I (V) is defined as;

$$I(V) = I_0 \left(e^{\frac{qv}{nkT}} - 1 \right) \tag{2.13}$$

I represents net current, V is a voltage, I_0 is adverse – feeding saturation current, n is ideal factor, k is Boltzmann constant and T represents temperature. In Figure 2.4, current-voltage characteristic of a diode is shown.
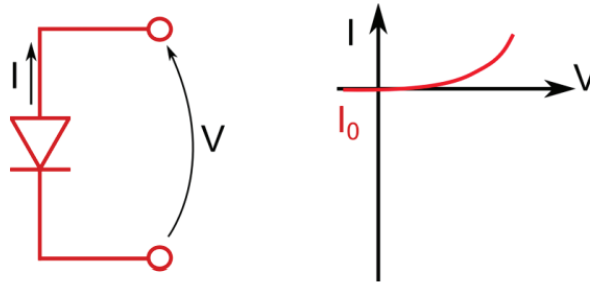
Figure 2.4. I-V Characteristic feature of a standard diode
(Source: Altamura, 2014)

Ideality factor (n) which belongs to a diode can be retain from I-V graph. This ideality factor is close to 1 value in ideal solar cells because of recombination mechanism. For this reason; when we want to define recombination mechanism in solar cell, alteration in ideality factor is played a huge role.

The working principle of solar cell is similar to the diode and both work with the logic of p-n junction. With a single difference, which one side (p-side) of the junction in the p-n junction is used as the light absorbing layer.
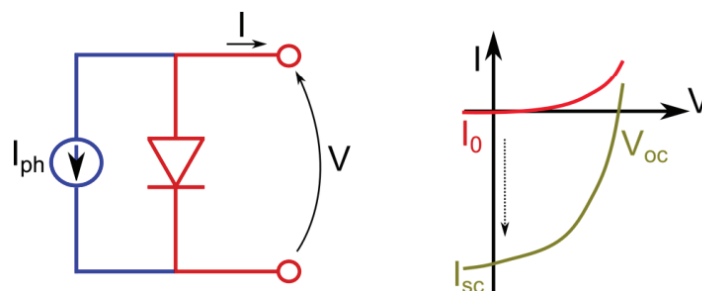
Figure 2.5. Model and I-V curve of a solar cell under light
(Source: Altamura, 2014).

Figure 2.5 shows I-V curve of a solar cell under light, additional electron-hole pairs are created giving rise to the named photogenerated current (I_{ph}) which could be model as a current generator in parallel to the standard diode.

2.2.1.1. Open Circuit Voltage (Voc)

The short circuit current I_{SC} corresponds to the short circuit condition when the impedance is low and is calculated when the voltage equals 0. I(0) is defined as;

$$I \text{ (at V=0)} = I_{SC} \tag{2.14}$$

I_{SC} occurs at the beginning of the forward-bias sweep and is the maximum current value in the power quadrant. For an ideal cell, this maximum current value is the total current produced in the solar cell by photon excitation.

$$I_{SC} = I_{MAX} = I_\ell \tag{2.15}$$

for forward-bias power quadrant.

2.2.1.2. Short Circuit Current (I_{OC})

The open circuit voltage (V_{OC}) occurs when there is no current passing through the cell.

$$V \text{ (at I=0)} = V_{OC} \tag{2.16}$$

V_{OC} is also the maximum voltage difference across the cell for a forward-bias sweep in the power quadrant.

$$V_{OC} = V_{MAX} \tag{2.17}$$

for forward-bias power quadrant

2.2.3. Fill Factor (FF)

The Fill Factor (FF) is actually a measure of quality of the solar cell. Calculated by comparing the maximum power to the theoretical power (PT) which would be output at both the short circuit current and open circuit voltage together (equation 2.18). FF can also be interpreted graphically as the ratio of the rectangular areas depicted in Figure 2.6.

$$FF = \frac{P_{max}}{P_\tau} = \frac{I_{mp}.V_{mp}}{I_{SC}.V_{OC}} \tag{2.18}$$
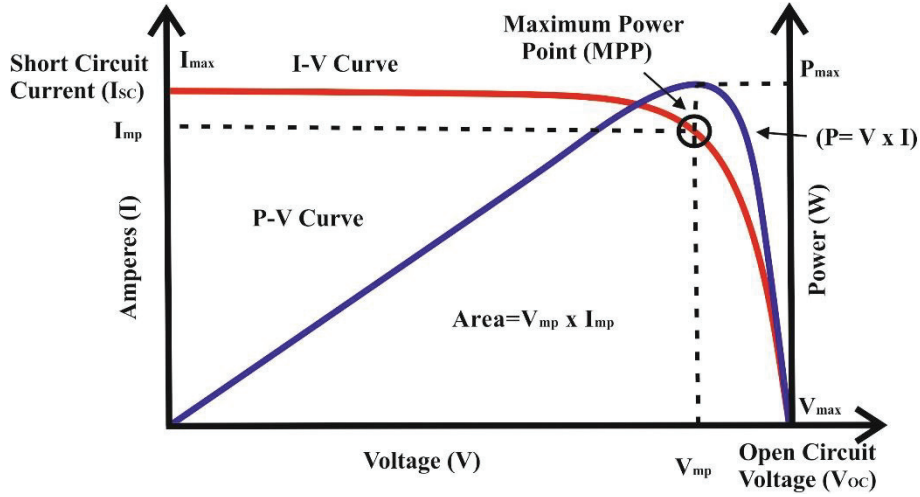
Figure 2.6. Getting the Fill Factor from I-V sweep

2.2.4. Efficiency (η)

Efficiency is the ratio of the electrical power output (P_{out}), compared to the solar power input (P_{inc}), into the photovoltaic cell. P_{out} can be taken to be P_{MAX} since the solar cell can be operated up to its maximum power output to get the maximum efficiency.

$$\eta = \frac{P_{max.}}{P_{inc.}} = \frac{V_{oc} \times I_{sc} \times FF}{P_{inc}} \tag{2.19}$$

P_{inc} is taken as the product of the irradiance of the incident light, it is measured in W/m^2 or in suns (1000 W/m^2), with the surface area of the solar cell [m^2]. The maximum efficiency (η_{MAX}) found from a light test is not only an indication of performance of the device under test, but, like all of the I-V parameters, can also be affected by ambient conditions, for example, which are temperature and the intensity and spectrum of the incident light. For this reason, it is recommended to test and compare photovoltaic cells using same lighting and temperature conditions.

In this chapter that we have the necessary theoretical knowledge for solar cell. Now that we can examine our experimental work in chapter 3.

CHAPTER 3

EXPERIMENTAL PROCEDURES

In this study, we fabricated CZTS absorber layer on soda lime glass (SLG) with dc magnetron sputtering and the post-deposition sulfurization process. We perform metallic precursor deposition layer by layer with layering order Cu, Sn, Zn, and Cu, respectively. Then these layers are heated up in a Sulfur (S) and Argon (Ar) atmosphere. In order to complete the p-type semiconducting compound absorber layer, which is CZTS. We used CZTS on SLG for structural characteristic properties, optical and electrical characterizations. Additionally, we used different substrates such as Mo coated glass and Ti foil to make both structural characteristic properties and procedure of device.

3.1. Substrate Preparation

CZTS absorber layers have been fabricated on SLG. The SLG substrates were cleaned by subsequent ultra-sonication in acetone, ethanol and distilled water and then dried under a nitrogen stream, and then cleaned under plasma. Also, we used another two types of substrates which are Ti foil and Mo coated glass for making the thin film solar cells. Ti foil was chemically etched with diluted HF and distilled H_2O. The aim of making chemical etching to remove the oxidized layer.

3.2. Metallic Precursors Fabrication

In the first stage of the fabrication, by using a multi-target magnetron sputtering system, Cu-Sn-Zn-Cu metallic layers were deposited. We used different substrate, which are soda lime glass, Mo coated glass and 100 μm thick and ≥99.9% trace metal basis Ti foils supplied by Sigma-Aldrich. The Cu-Zn-Sn layers were fabricated on these substrates via sulfurization of the stowed metallic precursors which were deposited by multi target dc magnetron sputtering from 2-inch-targets of Cu (99.999%), Zn (99.99%), Sn (99.999%) and again Cu (99.999%) at room temperature, respectively (Figure 3.1).
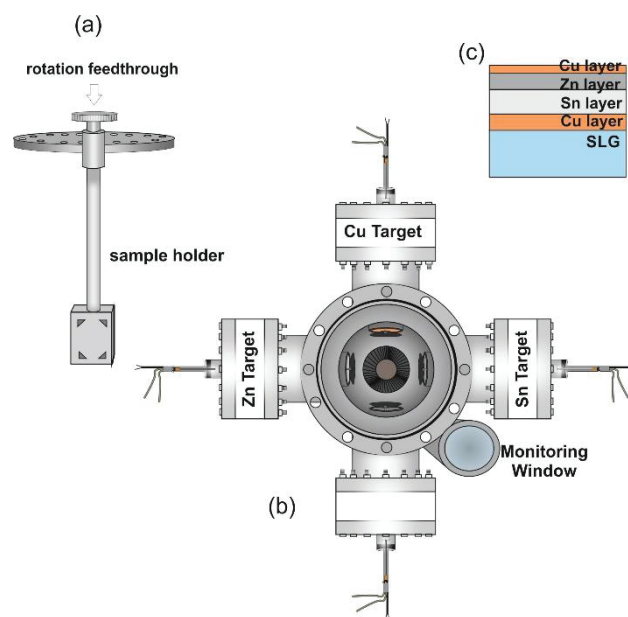
Figure 3.1. (a) The drawing of sample holder apparatus, (b) Schematic diagram of multi-targeted sputtering system (Source: Yazici et al., 2015), (c) The drawing of sputtered metallic thin film layers on SLG

In this procedure, the base pressure was achieved below 10^{-6} Torr when the sputtering was started. Operating pressure was supplied at 1.5×10^{-2} Torr, and also among target to substrate distance was fixed at 8 cm. The samples were obtained using a single sputtering run with a double-faced of sample holder apparatus (Fig. 3.1 (a)). In this manner, we deposited sequentially layered metallic precursors in the Cu/Sn/Zn/Cu layer ordering (Fig. 3.1 (c)) on SLG substrate and we also deposited same composition (Cu/Sn/Zn/Cu) on Mo coated glass and Ti foils. Besides that we used the S-containing precursor as ZnS. The S-containing precursor were produced identically with metallic precursors like Zn/Sn/Cu. In this procedure, the base pressure was achieved about 4.5×10^{-6} Torr when the sputtering was started. Operating pressure was supplied at 5.5×10^{-3} Torr. At that time, the substrate temperature was varied from 200 °C to 250 °C. ZnS layer was deposited by RF magnetron sputtering at 40W during 20 minutes. For SLG/ZnS/Sn/Cu layer stacking, we grown Sn and Cu respectively on ZnS. The target thicknesses values were 210, 290 and 175 nm for SLG/ZnS/Sn/Cu layers, respectively. For SLG/Cu/Sn/Zn/Cu layer stacking, the deposition times were regulated to different minutes for Cu, Sn, Zn and Cu targets by tuning sputtering powers. The target thickness values were 120, 290, 165 and 55 nm for SLG/Cu/Sn/Zn/Cu layers, respectively (Figure 3.2).
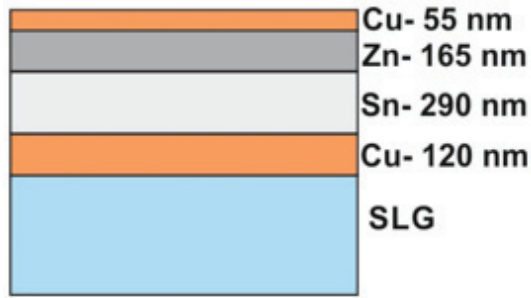
Figure 3.2. Illustration of the sample orders

Furthermore, some samples were grown as double layer stacking. If we give a brief information about this growth process, the first precursor was deposited like Cu/Sn/Zn/Cu layer ordering and then was formed by sulfurization process. The second precursor was deposited on the first layer similar to the first layer and then again this precursor was formed by sulfurization. Therefore, we will have the opportunity to examine both the 15 minute sulfurized sample and the double layered sample. The sulfurization process will be explained at section 3.3. We preferred double layer stacking because of without voids on surface and small grain size. Therefore, we expect better electrical properties.

3.2.1. Magnetron Sputtering Technique

To deposit materials onto a substrate as a thin film, many varied techniques are used which are classified as vacuum and non-vacuum. Sputtering is the most common one to deposit the thin films among these techniques. Magnetron sputter, is used in this thesis, is a kind of physical vapor deposition technique. In this technique, the working principle is based on ejecting atoms from target (deposited materials) onto substrate by condensing ejected atoms. In detail working principle, target is bombarded with energetic ions, especially Argon (Ar^+) as an inert gas. This process is occurred in high vacuum at a pressure of 1 mTorr. To create the plasma, hot gas phase that has ions and electrons, between the target and substrate DC voltage is placed. In addition, generally DC power supply is used to deposit conductor target. On contrast, RF power supply is used for insulating and semiconducting materials as a target. Charged Ar ions are accelerated to target and collision is occurred with the target atom. Subsequently, ejected target atoms are travelled onto the substrate and settled. This process cycle is continued, the released

electrons are accelerated to the substrate, by create more ions and electrons. Also, efficiency of sputtering is an important matter due to the fact that more released atoms provides more sputtering yield, which is increased proportional. Alongside working principle, rough and turbo molecular pump are used to reach the high vacuum value in mechanics. Mass flow controller (MKS) is used to control gas flow. Baratron is used to measure the pressure of the vacuum chamber on the contrary; thermocouple is utilized to measure the base pressure.

3.3. Sulfurization Process

The second stage of the growth is sulfurization of the metallic precursors by annealing them in a Sulfur (S) and Argon (Ar) atmosphere. Annealing temperature perform between 500 and 600 °C. The sulfurization procedure was accomplished in a Lindberg/Blue M tube furnace. We used a quartz glass tube. 600 mg of sulfur powder (99.98%) in the graphite box was placed at the upstream entry of the furnace and the metallic precursors on the graphite holder was located middle of the oven (Figure 3.3). The sulfur powder was heated to around 140 ºC for formation of sulfur vapor. Using a MKS 647C mass flow controller, 73 sccm Ar gas flow was directed into this tube as the carrier gas during the sulfurization process. The pressure was controlled at the atmospheric level.
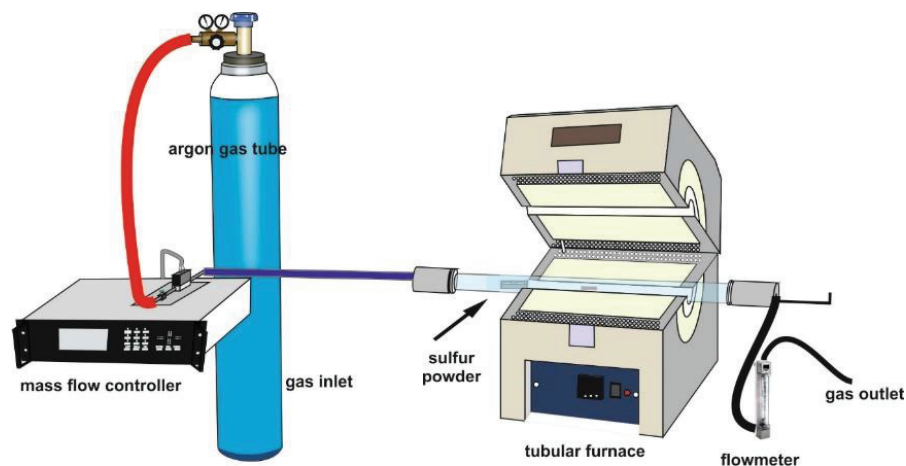
Figure 3.3: Illustration of sulfurization process

First of all, we set the furnace from room temperature to 270 ºC and the sulfur started to melt at that temperature of furnace. Afterwards, the furnace temperature was

raised to 550 ºC at the heating rate of 49 ºC/min. At that time, the films were exposed the sulfur and Ar gases during forty five minutes. Finally, the samples were given up natural cooling in Ar atmospheres. Figure 3.4 indicates the sulfurization process parameters of the CZTS-C films as a graph in detail.
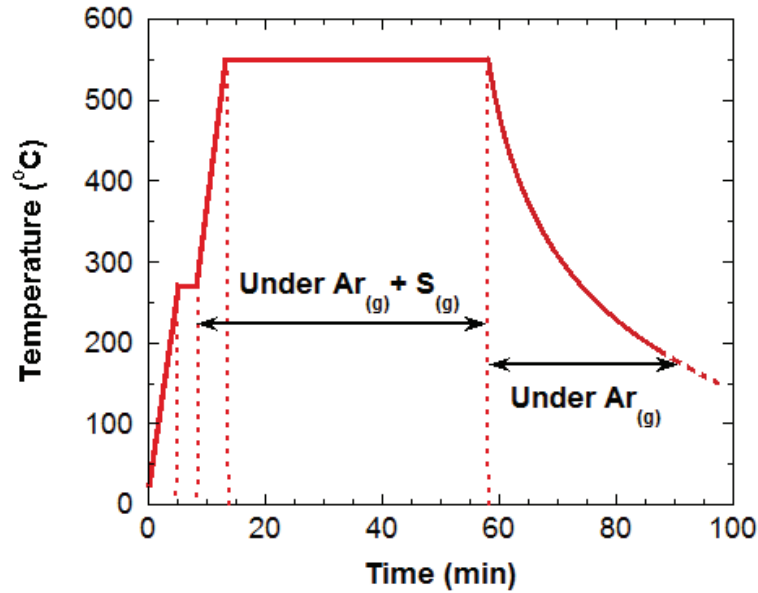
Figure 3.4: Sulfurization process of the deposited thin films

On the other hand, we observed secondary phases on the surface due to the sulfurization time and we changed this procedure. When the sulfurization time was reduced, we detected the least secondary phases on the surface. Moreover, the double layer samples were formed at 550 ºC during 15 minute in $Ar_{(g)}$ and $S_{(g)}$ atmosphere. We can consider bilayer deposition.

3.4. KCN Etching

We observed secondary phases like CuS in the CZTS-A film. The secondary phases will have negatively affected the efficiency to solar cell devices. Consequently, KCN etching to remove the CuS phases was used. First of all, we prepared the diluted solution which included 10 g KCN and 90 ml dH_2O. Then, the some CZTS films were left into the solution at 3 minutes and to clear into distilled water (Olgar et al., 2016).

3.5. Device Production

On the basis of the obtained CZTS semiconducting films, solar cell with the structure of Ti or Mo foil/CZTS/ZnOS/ZnO/AZO were fabricated. In this part, ZnOS layer around of the 40 nm thick was deposited by RF magnetron sputtering. Then other step was growth of ZnO layer which the layer thickness was about 50 nm with RF sputtering. AZO layer was grown nearly 250 nm by DC magnetron sputtering.

3.6 Characterization Methods

3.6.1. Scanning Electron Microscopy (SEM)

The growth morphology was researched using a scanning electron microscope (SEM; FEI-QuantaFEG 250) which was equipped with Energy Dispersive Spectroscopy (EDS; Oxford X-act). SEM measurements is most important electron-optical method to investigate of the morphology of films. We can see the crystal formation by the method in directly. The working principle is similar to optical microscope. The optical microscope uses light, but the SEM uses electrons, which are the focused scanned electron beam, to produce images of the sample. The advantage of the SEM analysis is that we can see the material in an atomic level with a higher resolution by usage of smaller wavelength. The basic principle is that a beam of electrons is generated field emission gun for this microscope. The electron beam is accelerated through a high voltage (e.g.: 15 kV) and pass through a system of apertures and electromagnetic lenses to produce a thin beam of electrons, and then the beam scans the surface of the sample. The electron beams having energies ranging from a few thousand to 10 keV, smaller wavelength than light are utilized.

3.6.2. Energy Dispersive X-Ray Spectroscopy (EDX)

EDX analysis of the samples gave us fundamental information about the stoichiometry of the CZTS semiconductor compounds. EDX measurements ensure to investigate composition of the samples. The operational principle of EDX is that the electron beam generates X-rays within the sample. Many of X-rays have energies

characteristic of the elements which emitted them. That is, this procedure is that the bombardment of the sample with electrons and excitation of the bound electrons to leave the atomic shells. Consequently, these vacant shells are the filled up from outer shells via electrons. Every element has a characteristic atomic structure, the specific energies are produced and send through to detector for determined the content.

3.6.3. X-Ray Diffraction (XRD) Analysis

The crystal structures of deposited the CZTS samples were measured by X-ray diffraction (XRD; Philipps X'Pert Pro). The XRD was operated in the Bragg-Brentano focusing geometry from 20º to 80° on a Phillips X'Pert Pro X-Ray diffraction, with CuK_α radiation (λ=1.5406 Å) using a step size of 0.016° and a time step of 15 min. The working principle based on the diffraction of X-Ray waves by a crystal lattice. Namely, the wavelength of the wave should be in the range of lattice constants, so as to take place in the material. It is well-known that, XRD analysis is an incompetent technique with alone for structural characterization of CZTS, because of the formation of analogue crystal structured second phases during the synthesis of CZTS compound. For this reason, Raman scattering analysis was also needed to get a complete and reliable analysis.

3.6.4. Raman Spectroscopy

Raman spectroscopy is an effective spectroscopic technique in the investigation of the material having complex structure. The Raman modes of CZTS samples were measured with with a confocal micro-Raman spectroscopy system (S&I Mono Vista) equipped with a 100 mW Melles-Griot Ar ion laser operating at 514 nm. Also, all measurements were performed with an Olympus BX51 down-looking microscope with 5x, 10x, 50x, and 100x objectives, and a 750 mm focal length monochromator (Princeton Instrument, Acton SP2750 0.750mm Imaging Triple Grating Monochromator) containing 600 grooves/mm holographic grating at room temperature. Raman signal was collected with a high resolution CCD camera with 1600x200 pixels. To be able to see the Raman active phonon modes of CZTS films and the vibrational modes of some other possible phases via this measurement. According to the working principle, to base on the inelastic scattering of monochromatic light. It also bases on the light-matter interaction. The

frequency of the monochromatic light changes after its interaction with the sample, due to inelastic scattering takes place.

The photons of the monochromatic light absorbed by the sample and the reemitted with a shifted frequency. Comparing the original monochromatic frequency of this shift is called Raman Shifts. These shifting give information about the vibrational and rotational frequency transitions in molecules.

3.6.5. Transmission and Reflection Analysis

A PerkinElmer Lambda 950 UV/VIS/NIR spectrometer was used for optical measurements of the CZTS samples. Transmission and reflection measurements were used to measure for band gap calculations. The CZTS film thicknesses were measured via Veeco DEKTAK 150 surface profilometer.

3.6.6. Electrical Characterization

For investigating electrical and optical properties, we fabricated the CZTS samples on SLG. Therefore, van der Pauw measurements, which are Keithley 2182A nanovoltmeter, Keithley 7001 switch system, Keithley 220 programmable current source, and Lakeshore 450 Gaussmeter and Phywe 06480.01 electromagnet devices for Hall effect measurements were used to measure sheet resistance, resistivity, hall coefficient, mobility and carrier concentration of the CZTS semiconductor materials. The sheet resistance at room temperature, temperature dependence resistivity and Hall effect were measured via the cryostat system (Figure 3.5). The system was cooled with liquid nitrogen from room temperature 300 K to 80 K. Hall effect measurement was done under 1640 G permanent magnetic field (Figure 3.5).
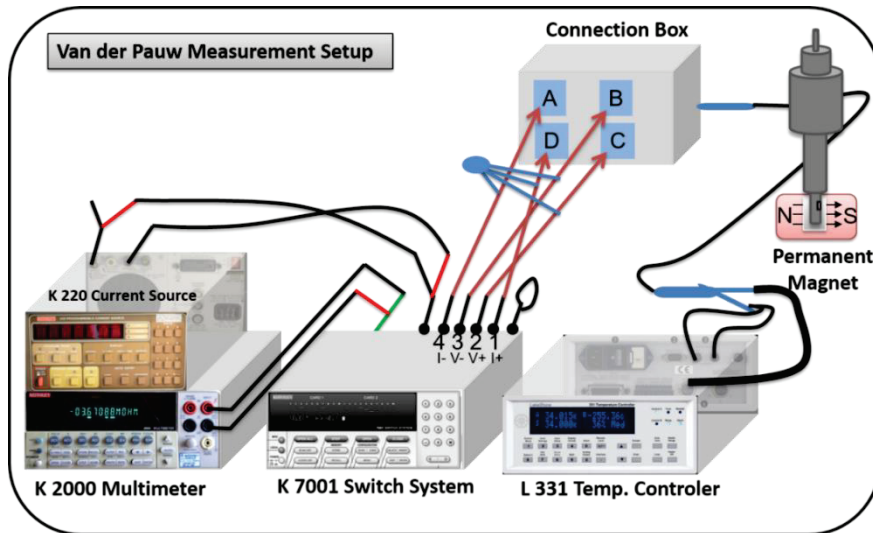
Figure 3.5. The schematic representation of Cryostat system

In Figure 3.6, the basic configuration for resistivity and Hall voltage measurement is shown. The each intersection of a row and a column is named as a crosspoint. This crosspoint is indicated as a small circle on the diagram. Using suitable programing, a particular row can be connected to prefer a column by closing the acceptable crosspoint. Source and measurement devices are connected to the columns while samples are connected to the rows. For example, we suppose to apply a current through terminal 1 and 2 to the sample and the voltage of the sample is measured among terminal 3 and 4 using program.
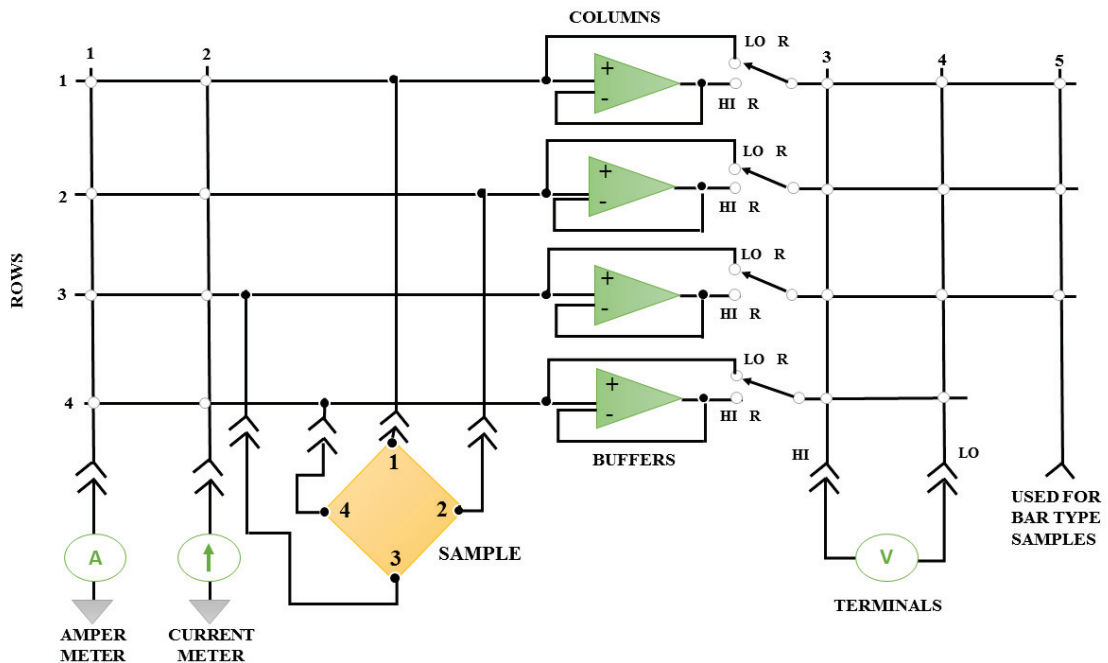
Figure 3.6. Measurement configuration for resistivity and Hall voltage measurement

3.6.6.1. Resistivity

The resistivity is defined as ρ and it can be computed from calculated mobility and carrier concentration values in semiconductor.

$$\rho = \frac{1}{q(n\mu_n + p\mu_p)} \qquad (3.1)$$

In which n and p are the free electron and hole concentration. μ_n and μ_p are the electron and hole mobility, respectively. Usually, the carrier concentration and mobility are not known. So, we must try to find alternative methods for measurement of resistivity.

3.6.6.1.1. The Four-Point Probe Technique

One of the most common methods is the four-point probe technique for measuring the resistivity.
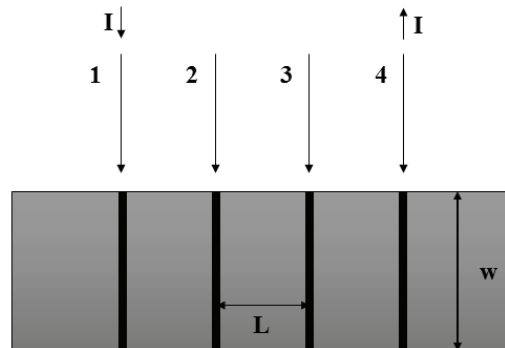
Figure 3.7. A collinear four point probe

The four point probe includes four thin collinearly placed conductor wires probes which are made to contact the sample under test in Fig 3.7. Current (I) flows between the outer probes which are entering probe 1 and leaving probe 4, and voltage V is measured between the two inner probes, ideally without drawing any current.

$$\rho = R * \frac{t*w}{L} \ \Omega.\,cm \qquad (3.2)$$

R: Sheet resistance (**Ω)**

t: thickness of the thin film on substrate (**cm)**

w: the width of sample (**cm)**

L: probe spacing (the between 2 and 3 probes) (**cm)**

3.6.6.1.2. The Van der Pauw Technique

The van der Pauw technique is commonly used to measure the resistivity and the Hall coefficient of a sample. The van der Pauw technique allows us study with the small size samples compared with the four point probe measurement. The current is applied between two terminals while the voltage is measured between to opposite terminals, as seen Figure 3.8. A total of eight measurements are taken with each possible terminal and current convention.
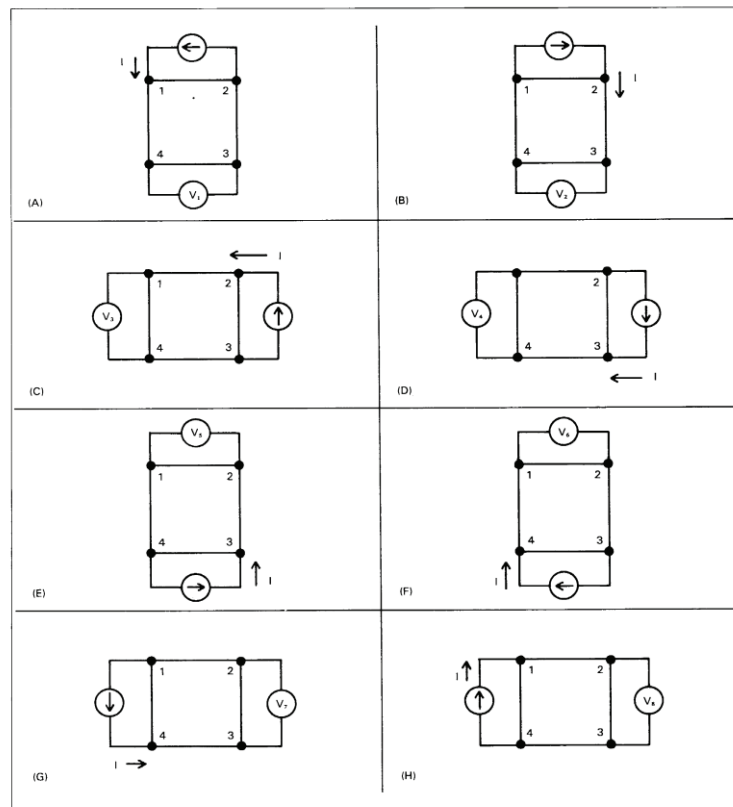
Figure 3.8. The configuration of resistivity measurement
(Source: Hall Effect Card Instruction Manual)

To measure the resistivity values, current and the voltages values through the sample can be measured using Table 3.1. Two values of resistivity, which are ρ_A and ρ_B, are calculated as follows (equation 3.3 and 3.4).

$$\rho_A = \frac{1.1331 * t_s * f_A}{I}(V_2 + V_4 - V_1 - V_3) \tag{3.3}$$

$$\rho_B = \frac{1.1331 * t_s * f_B}{I}(V_6 + V_8 - V_5 - V_7) \tag{3.4}$$

In there, t_s is thickness of the sample in cm, f_A and f_B are geometrical factors based on sample symmetry, I is curren111t in amperes, V_1-V_8 are the measured voltages. The average resistivity, ρ_{Avg} value can be determined as follow (equation 3.5).

$$\rho_{Avg} = \frac{\rho_A + \rho_B}{2} \tag{3.5}$$

Table 3.1. Crosspoints for resistivity measurements

Voltage Designation	Crosspoints Closed (Column and Row)				Applied Current	Measured Voltage
V_1	1, 2	2, 1	3, 3	4, 4	1-2	3-4
V_2	2, 2	1, 1	3, 3	4, 4	2-1	3-4
V_3	2, 2	1, 3	3, 4	4, 1	2-3	4-1
V_4	2, 3	1, 2	3, 4	4, 1	3-2	4-1
V_5	2, 3	1, 4	3, 1	4, 2	3-4	1-2
V_6	2, 4	1, 3	3, 1	4, 2	4-3	1-2
V_7	2, 4	1, 1	3, 2	4, 3	4-1	2-3
V_8	2, 1	1, 4	3, 2	4, 3	1-4	2-3

3.6.6.2. Mobility

The term of mobility is used to characterize how an electron or a hole can move through samples. So, we can know that it influence the samples behavior whether they are metal or semiconductor.

The mobility of the carriers in a semiconductor material is also effected by the presence of charged impurities. Impurity scattering is caused by crystal defects like ionized impurities. At low temperatures, carriers move more slowly, thus there is more time for them to interact with charged impurities. For this reason, as the temperature decreases, impurity scattering increases, and the mobility decreases. This is just the opposite of the effect of lattice scattering (holes).

At very high temperatures,

$$n = p = n_i \tag{3.6}$$

The semiconductor becomes "intrinsic" at very high temperatures. At the other extreme of very low temperature, fermi energy (E_F) may rise above the donor energy (E_d), and most of the donor (or acceptor, in the case of p-type material) atoms can remain no ionized.

The fifth electrons stay with the donor. This phenomenon is known as freeze-out. In this case, if the doping is convenient enough to form an impurity band, the dopants are not totally ionized. Freeze-out is a matter when semiconductor devices are operated at, for example, the liquid–nitrogen temperature (80 K) in order to conclude low noise and high speed.

3.6.6.3. Hall Effect

The number and type of charge carriers like electrons or holes, the resistivity and the mobility with a relatively simple measurement can be determined Hall effect measurement.

When applying a magnetic field, a conductor perpendicular to the current flow direction produces an electric field perpendicular to the current and the magnetic field. In the p-type semiconductor sample, the current and holes flow in y-direction, the magnetic field is in the z-direction.
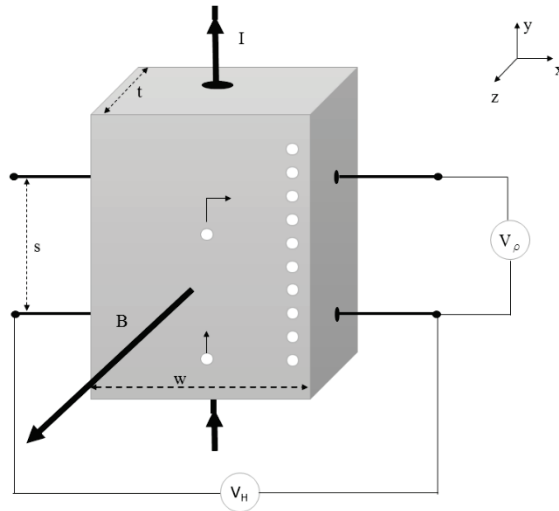
Figure 3.9. A schematic representation of the Hall effect in a p-type sample.

In Figure 3.10, the configuration of Hall voltage measurements is shown. The current is applied and then the voltage is measured across the diagonal of the sample. The eight measurements are necessary both ± I (positive and negative current) (Table 3.2), and ± B (positive and negative magnetic flux).
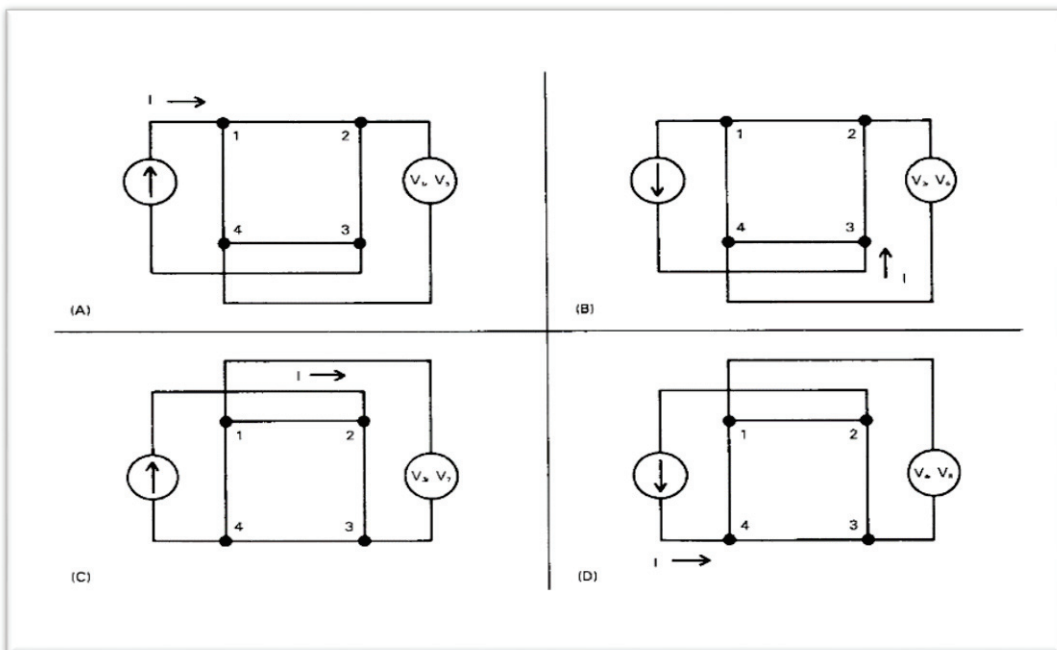
Figure 3.10. The configuration of Hall voltage measurement
(Source: Hall Effect Card Instruction Manual)

For Hall voltage measurements, we calculated two Hall coefficient, R_{HC} and R_{HD}, using the voltages as follows:

$$R_{HC} = \frac{2.5*10^7 t_s}{B*I}(V_2 - V_1 + V_5 - V_6) \tag{3.7}$$

$$R_{HD} = \frac{2.5*10^7 t_s}{B*I}(V_4 - V_3 + V_7 - V_8) \tag{3.8}$$

Then, the program calculated the average of R_{HC} and R_{HD} and to be achieved the graph of R_H (cm³/C) versus temperature (K). In there, R_{HC} and R_{HD}, are Hall coefficients in cm³/C. t_s is the sample thickness in cm. B is the magnetic flux in gauss. I is current and V_1-V_8 are voltages using Table 3.2. The average Hall coefficient, R_{Avg} value can be calculated as follow (equation 3.9).

$$R_{Avg} = \frac{R_{HC} + R_{HD}}{2} \tag{3.9}$$

Table 3.2. Crosspoints for Hall voltage measurements

Voltage Designation	Flux	Crosspoints Closed (Column and Row)				Applied Current	Measured Voltage
V_1	+ B	2, 1	1, 3	3, 4	4, 2	1-3	4-2
V_2	+ B	2, 3	1, 1	3, 4	4, 2	3-1	4-2
V_3	+ B	2, 2	1, 4	3, 1	4, 3	2-4	1-3
V_4	+ B	2, 4	1, 2	3, 1	4, 3	4-2	1-3
V_5	- B	2, 1	1, 3	3, 4	4, 2	1-3	4-2
V_6	- B	2, 3	1, 1	3, 4	4, 2	3-1	4-2
V_7	- B	2, 2	1, 4	3, 1	4, 3	2-4	1-3
V_8	- B	2, 4	1, 2	3, 1	4, 3	4-2	1-3

We used van der Pauw method to measure the electrical resistivity, and to reveal majority charge carrier properties. The thickness of the film is very important parameter for this method. It is preferable that the sample is almost symmetrical for reduce the errors in calculations. The CZTS sample was cut into little rectangular shape with using a

diamond cutter. Film sheet resistance was measured between thin and small copper wire electrical contacts that were inserted on the film using silver paint (Figure 3.11).
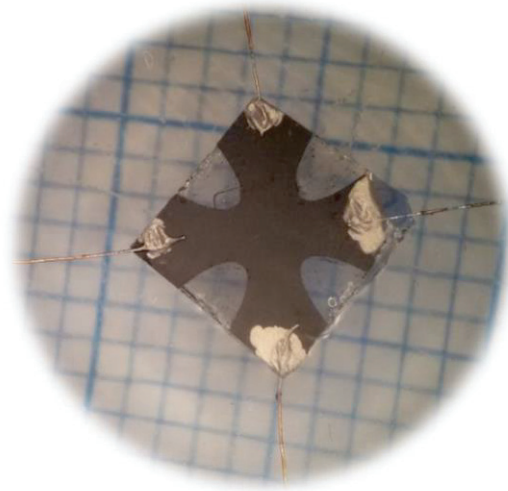
Figure 3.11. CZTS thin film on SLG substrate

0.01 mA and 1 mA current were applied for resistivity and Hall effect measurements, respectively. Then temperature of cryostat was decreased to 80K with liquid nitrogen.

CHAPTER 4

RESULTS AND DISCUSSION

In this part, we will discuss the results of samples in Table 4.1. Table 4.1 lists the growth parameters of sample.

Table 4.1. Table of growth parameters of discussed samples

	Substrate	Layer Ordering	Sulfurization Temperature	Sulfurization Duration
CZTS-A	SLG	Cu/Sn/ZnS	560	90 minute
CZTS-B	SLG	Cu/Zn/Sn/Cu	550	30 minute
CZTS-C	SLG	Cu/Zn/Sn/Cu	550	45 minute
CZTS-D	SLG	Cu/Zn/Sn/Cu	550	60 minute
CZTS-E	SLG	1st staking: CZTS-1 Cu/Zn/Sn/Cu 2nd staking: CZTS-2 Cu/Zn/Sn/Cu/CZTS-1	550	1st stacking 15 min 2nd stacking 15 min

4.1. Morphological and Compositional Analysis

In the prevent work, thicknesses of each elements were targeted through molecular weight and density calculation as theoretical for the CZTS compound material. Then, this values were supplied as experimental and the thicknesses of samples (SLG/Cu/Sn/Zn/Cu) were measured via the profilometer as 120, 290, 165 and 55 nm. In the beginning of the study, we fabricated CZTS structure on SLG with DC magnetron sputtering method and following process was sulfurization. For the deposition, we decided the optimum parameters such as sputtering power, times and layer ordering via compositional analysis which was results of EDX analysis. EDX measurement was observed stoichiometric case materials. Besides, we optimized the parameter of sulfurization owing to structural analysis. We fabricated about 250 CZTS thin films on different substrates, after the calibration of both stages. About 40 of them were deposited on SLG substrate. In this study, we focused on temperature dependence of electrical properties with SLG-CZTS.
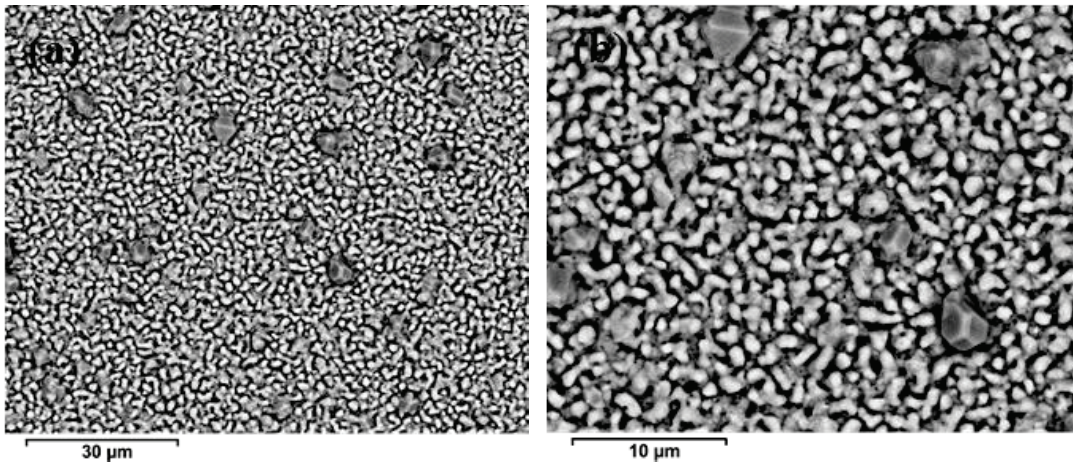
Figure 4.1. SEM images of CZTS-A (a) 5000 magnification (b) 10000 magnification

The SEM images in Figure 4.1 belong to sample CZTS-A. The precursor state of CZTS-A was deposited SLG/ZnS/Sn/Cu layer ordering. The SEM images of CZTS-A is shown dense and non-homogeny crystallization. Furthermore, distinct grains were found due to the secondary phases. For removing the secondary phases, the sample was etched via KCN. From the SEM results of the sample CZTS-A-after KCN (Figure 4.2), we can see lots of voids distributed in the surface. While the secondary phases removed, defects have been occurred on surface of the sample. Therefore, these defects have been effected electrical properties of the sample unfavorable.
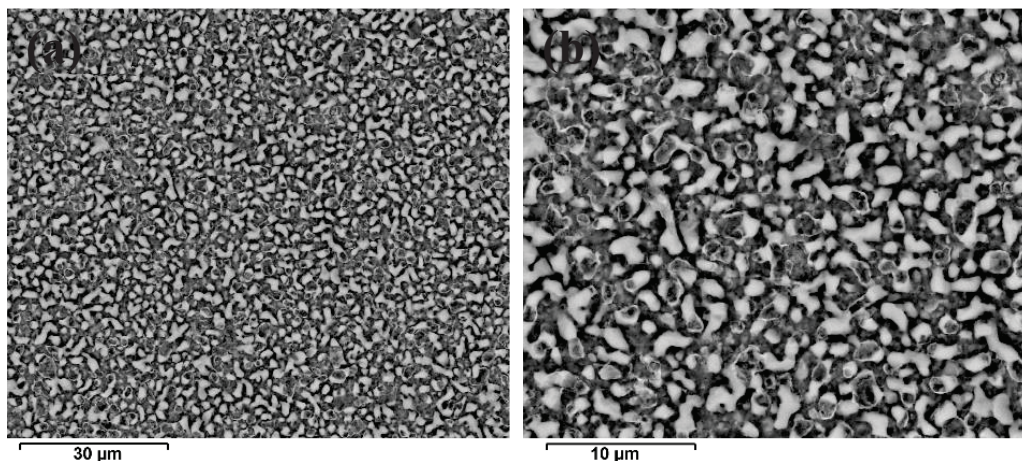
Figure 4.2. SEM images of CZTS-A-after KCN (a) 5000 magnification (b) 10000 magnification

On the other hand, when we look at the results of EDX analysis, compositional ratios of the CZTS-A-after KCN is better than. Table 4.2 lists the chemical composition and compositional ratios CZTS-A and CZTS-A-after KCN. It indicates that Cu rich, Zn

rich composition was obtained in CZTS-A. But CZTS-A-after KCN is better than. The compositional ratio of S/Metal for CZTS-A-after KCN demonstrated to be Cu poor Zn rich composition. In the literature, the CZTS samples with Cu/[Zn+Sn] lower ratio lead to higher conversion efficiency (Katagiri et al., 2001). Lower Zn/Sn ratio indicates that each film has poorer Zn content. For the reason that the composition is related to the sulfur content during sulfurization process, the ratio of S/[Cu+Sn+Zn] should be greater than the unity in the results of EDX. This ratio shows that the sulfurization process was not achieved efficiently before etching process.

Table 4.2. EDX results of CZTS-A and CZTS-A-after KCN

Sample	Chemical composition				Compositional ratio		
	Cu (at%)	Zn (at%)	Sn (at%)	S (at%)	Cu/ [Zn+Sn]	Zn/Sn	S/[Cu+Zn+Sn]
CZTS-A	29.53	13.65	11.77	45.06	1.16	1.15	0.82
CZTS-A after KCN	19.87	14.24	13.71	52.18	0.71	1.03	1.09

Due to the fact that using process for produced CZTS-A and another is quite long and not enough, we preferred to change deposition process before sulfurization stage. The sample CZTS-B, which is grown on SLG and deposited as SLG/Cu/Sn/Zn/Cu layer ordering by 30 min sulfurization. When looking at the images, we can see that the sample has dense and homogeny crystallization surface (Figure 4.3).
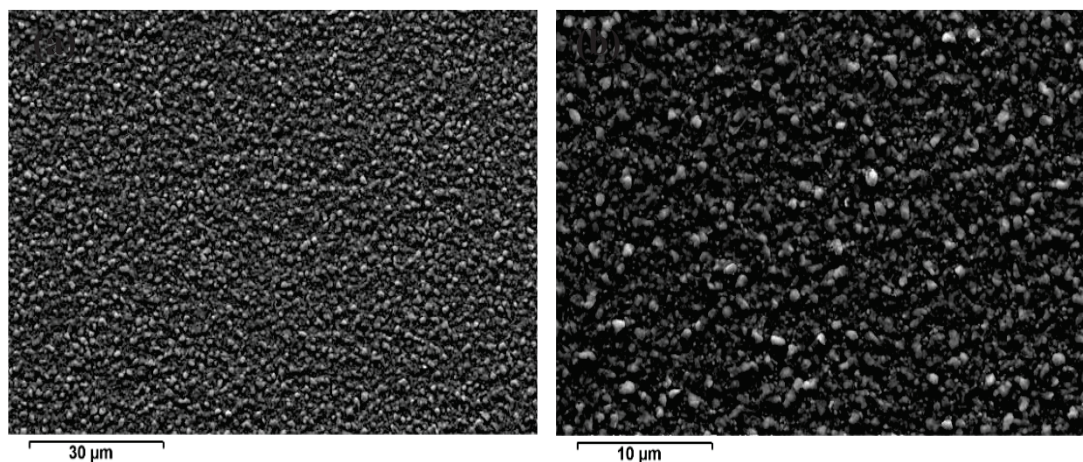
Figure 4.3. SEM images of CZTS-B (a) 5000 magnification (b) 10000 magnification

Table 4.3. EDX results of CZTS-B and CZTS-B prepared region for the Hall effect

Sample	Chemical composition				Compositional ratio		
	Cu (at%)	Zn (at%)	Sn (at%)	S (at%)	Cu/ [Zn+Sn]	Zn/Sn	S/[Cu+Zn+Sn]
CZTS-B	28.45	12.86	12.95	45.74	1.10	0.99	0.84
CZTS-B prepared region for the Hall effect	24.53	10.41	13.42	51.64	1.02	0.77	1.06

As can be seen in Table 4.3, CZTS-B is highly Cu rich, means deposition of metallic layer was not successful. EDX analysis of CZTS-B prepared region for the Hall effect revealed the slightly Sn rich composition. Namely, the sample CZTS-B has distributed non-uniform surface, even if the SEM images show homogeny crystallization. Hence, we have fabricated in the same way again with a difference of 45 minutes sulfurization to check whether this layer ordering is correct. And then, CZTS-C is grown on SLG and deposited as SLG/Cu/Sn/Zn/Cu layer ordering. Considering Figure 4.4, it can be clearly seen that the sample composed of packed grains densely and no voids on the surface. Despite of apart from bight needle shaped crystal formation, more uniform surface is dominant (Figure 4.4 (a)).
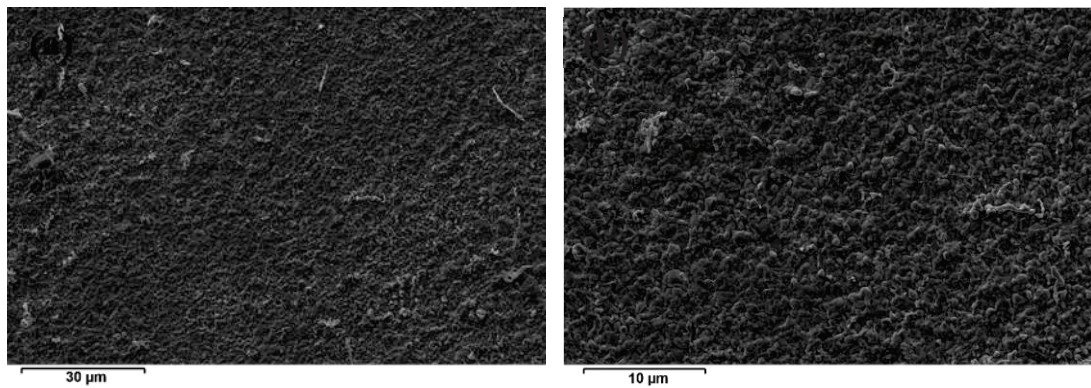
Figure 4.4. SEM images of CZTS-C (a) 5000 magnification (b) 10000 magnification

As shown in Table 4.4, the chemical composition ratio of Cu/[Zn+Sn], Zn/S and S/[Cu+Zn+Sn] for CZTS-C. It indicates that Cu poor composition was obtained, but Zn content was as same as Sn content. We also examined compositional and morphological

analysis of the sample prepared for the Hall effect. In the region, Cu poor and Sn rich composition was observed (Table 4.4).

Table 4.4. EDX result of CZTS-C and CZTS-C prepared region for the Hall effect

Sample	Chemical composition				Compositional ratio		
	Cu (at%)	Zn (at%)	Sn (at%)	S (at%)	Cu/ [Zn+Sn]	Zn/Sn	S/[Cu+Zn+Sn]
CZTS-C	23.07	12.46	12.62	51.85	0.91	0.98	1.07
CZTS-C prepared region for the Hall effect	21.76	11.98	14.26	52.00	1.98	0.84	1.08

According to the result, the Zn/Sn ratio was indicated poorer Zn content. Considering to S/[Cu+Zn+Sn] ratio, it can be seen that the sulfurization stage was successful. On the other hand, CZTS-C prepared for the Hall effect had Cu-rich and Sn-rich composition, although the sulfurization stage was successful. That is, the sample has not completely homogeny crystallization. So, we thought it would be better to extend the sulfurization time for CZTS-D, and then the same deposited precursor with others was annealed with sulfur atmosphere for 60 minutes.
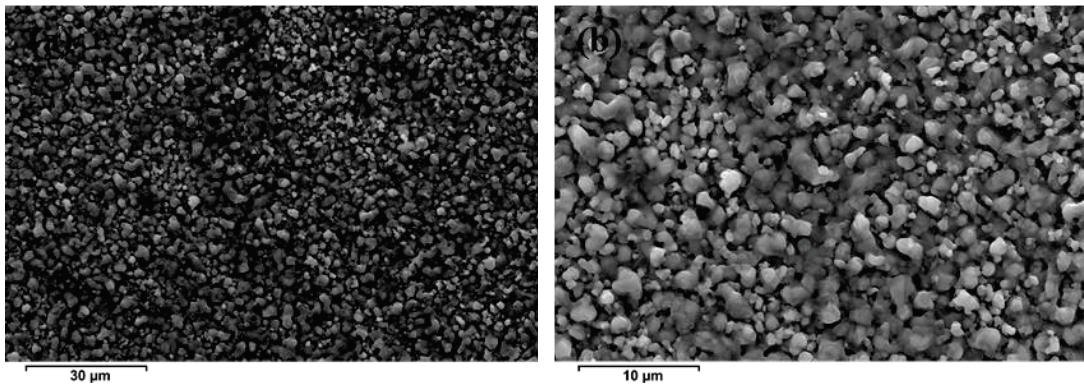
Figure 4.5. SEM images of CZTS-D (a) 5000 magnification (b) 10000 magnification

The sample CZTS-D, which is grown on SLG and again deposited as SLG/Cu/Sn/Zn/Cu layer ordering. In the Figure 4.5, we can see that the sample has distinct grains, dense and homogeny crystallization surface. Besides, CZTS-D prepared

region for Hall effect indicate that Cu poor Zn rich composition was obtained (Table 4.5). Considering to the EDX results, it can be seen that the sulfurization stage was successful.

Table 4.5. EDX result of CZTS-D and CZTS-D prepared region for the Hall effect

Sample	Chemical composition				Compositional ratio		
	Cu (at%)	Zn (at%)	Sn (at%)	S (at%)	Cu/ [Zn+Sn]	Zn/Sn	S/[Cu+Zn+Sn]
CZTS-D	21.14	12.04	13.80	53.02	0.81	0.87	1.12
CZTS-D prepared region for the Hall effect	22.34	13.58	13.25	50.83	0.83	1.02	1.03

The sample CZTS-E, which was grown on SLG and deposited as SLG/CZTS-1/CZTS-2 double layer. CZTS-1, which was deposited Cu/Sn/Zn/Cu on SLG with sulfurization at 550 °C. Then, the sample was grown on SLG/CZTS-1 as Cu/Sn/Zn/Cu layer ordering via sulfurization at 550 °C. In this procedure, sulfurization time was shorter, which is 15 minute, contrary to others.
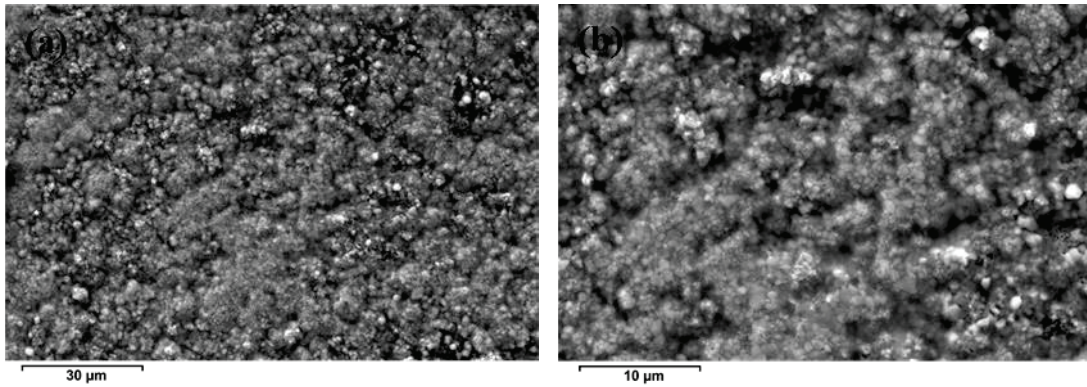
Figure 4.6. SEM images of CZTS-E (a) 5000 magnification (b) 10000 magnification

When we look at the Figure 4.6, we can see that the sample CZTS-E has smaller grain size, quite dense, no voids due to double layer and homogeny surface. EDX results of CZTS-E shows that Cu poor and Zn poor was occurred (Table 4.6), though the ratio of S/Metal was greater than the unity.

Table 4.6. EDX result of CZTS-E

Sample	Chemical composition				Compositional ratio		
	Cu (at%)	Zn (at%)	Sn (at%)	S (at%)	Cu/ [Zn+Sn]	Zn/Sn	S/[Cu+Zn+Sn]
CZTS-E	24.16	11.75	12.78	51.31	0.98	0.91	1.05
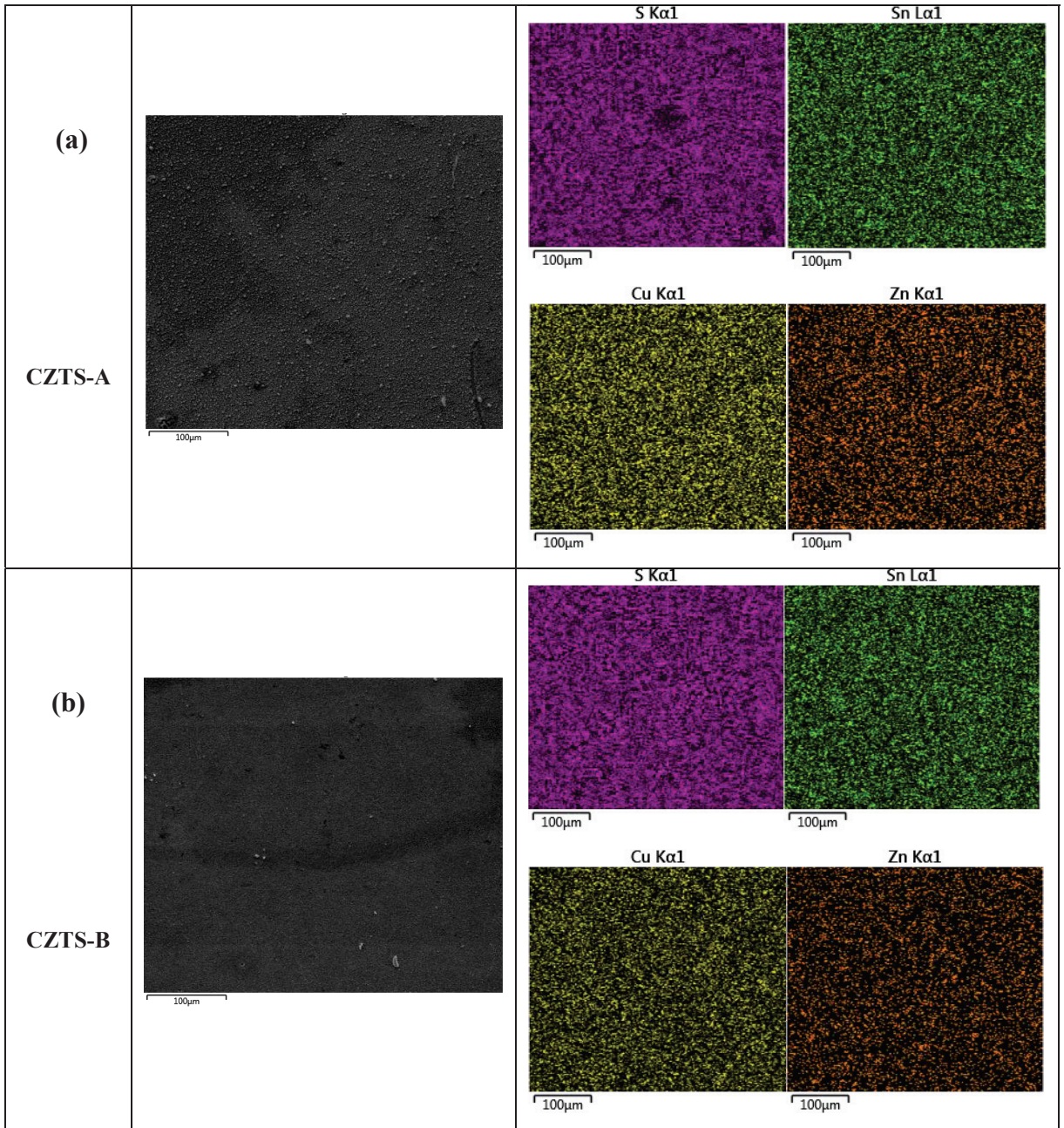
Figure 4.7. Mapping images of all CZTS samples prepared for the Hall effect at 1000 Magnification a) CZTS-A, b) CZTS-B, c) CZTS-C, d) CZTS-D, e) CZTS-E **(Cont. on next page)**
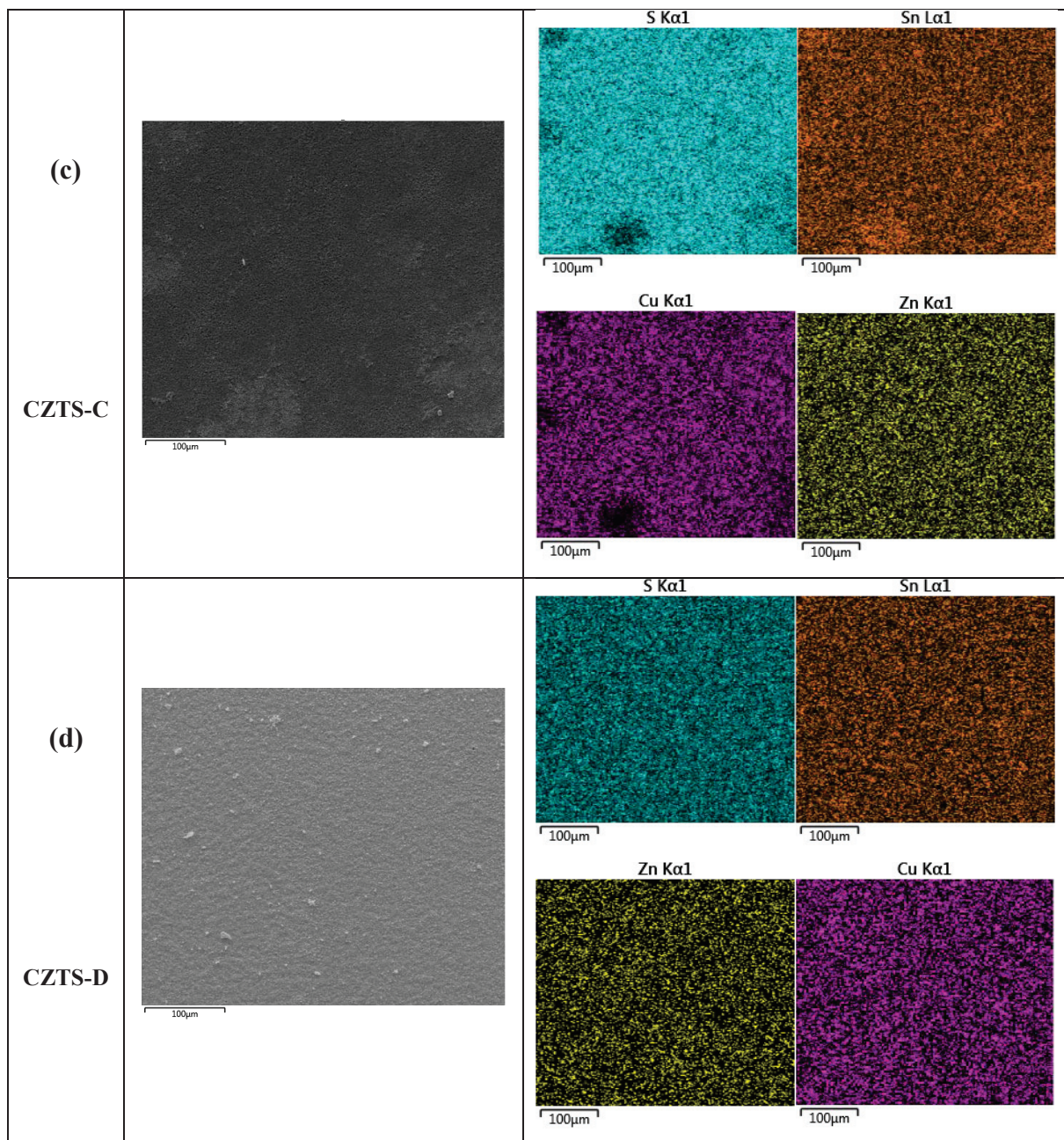
Figure 4.7. (**Cont. on next page**).

(e)
CZTS-E
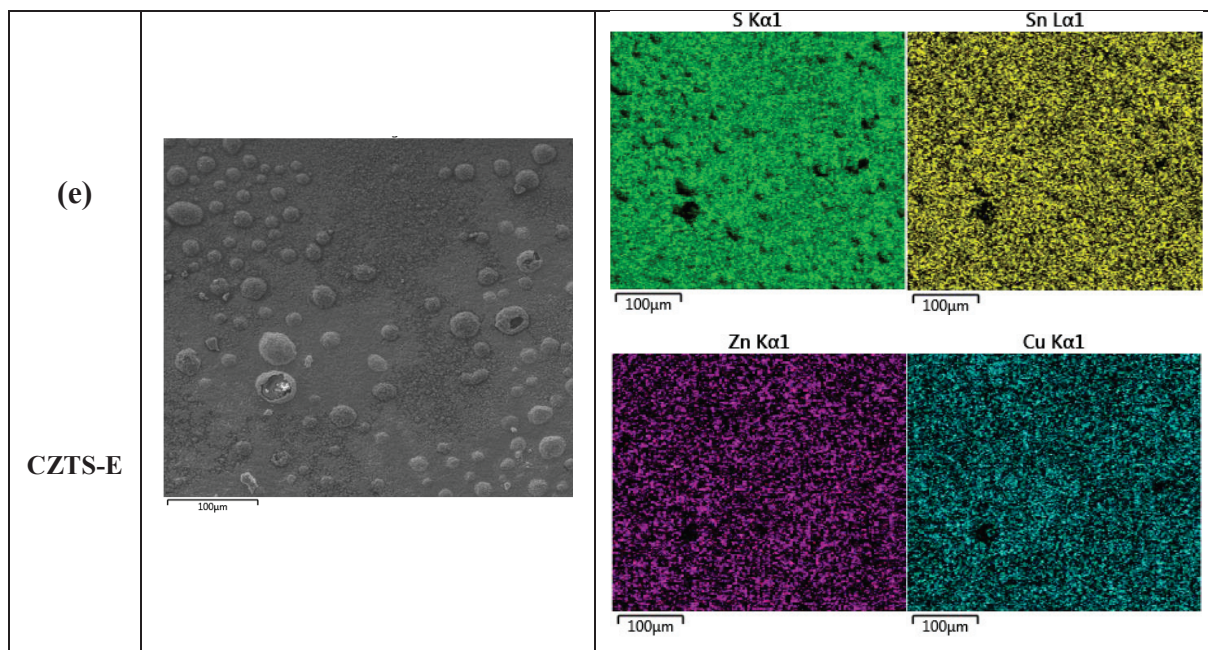
Figure 4.7. (cont.).

In the mapping images of CZTS samples at Figure 4.7, some regions are generally no uniform surface. When looking at Figure 4.7, we can see that striking different existed among the images of samples CZTS-C and CZTS-E. According to the images of CZTS-C, Sn-rich region was observed at left of the region. Besides, the bubbles on the surface of CZTS-E were obtained because of second sulfurization stage.

4.2. Structural Analysis

4.2.1. XRD Analysis

The crystal formations of the films were investigated by XRD analysis. However, it is well known that XRD analysis does not reveal information about the crystal structure of kesterite CZTS (JCPDS: 026-0575) with alone. For example, kesterite structure CZTS generally overlaps with having the same in-plane cell parameters and being the kesterite c parameter a multiple of the ZnS one, which is ZnS (JCPDS card number 00-05-0566) and Cu_2SnS_3 (JCPDS card number 00-027-0198) which having similar symmetry and lattice constant with CZTS (Figure 4.8). Therefore, complementary techniques to characterize CZTS samples like Raman spectroscopy analysis should be used.
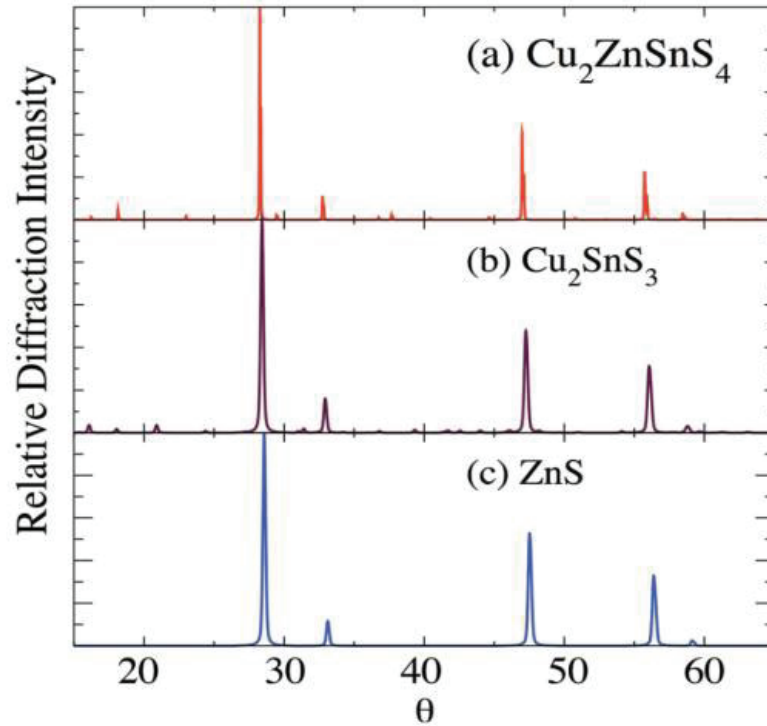
Figure 4.8. Overlapping of CZTS, Cu_2SnS_3 and ZnS XRD peaks (Source: Walsh et al., 2012).

CZTS has two principal structures which are stannite type and kesterite type as crystallographic. These two structures are similar except for the different orders of 'Cu' and 'Zn' atoms. However, CZTS material usually appears in kesterite structure because of thermodynamically more stable as compared to stannite type (Eren et al., 2014) (Ericson et al., 2012). X-ray diffraction peaks was generally observed for this material corresponds to the lattice planes (112), (200), (220/204), and (312/116) with preferred orientation along (112) (Olgar et al., 2016). Corresponding peaks which (002), (008), (101), (103), (105), (110), (211), (213), (224) and (332) planes were also reported (Fernandes et al. 2010; Friedlmeier 2001). Nevertheless, Secondary phases like Sn_xS_y compounds (SnS, SnS_2 and Sn_2S_3) can be easily identified by X-ray diffraction, which showing diffraction peaks clearly distinct from those of CZTS (Yazici et al., 2015).

In this work, the peaks of crystal structure were assigned by the X-Pert HighScore Plus where SearchMatch property embedded in it. When looking at the results of the XRD analyses, we can see that the well- matched diffraction peaks which of kesterite CZTS JCPDS (Joint Committee on Power Diffraction Standards) 026-0575 (Figure 4.10-15). In these figures, the sharp peaks of the thin films at $2\theta = 28.56°$, 29.6°, 32.99°, 47.3°, 56.2°, 58.97°,69. 30° and 76.44° corresponding to the diffraction of the (112), (103), (200),

(220), (312), (224), (008) and (332) planes of tetragonal, body centered, kesterite structure CZTS (JCPDS card number 026-0575) (Figure 4.9), respectively. Namely, the perfect kesterite structure of CZTS is indicated quite clearly. There are some secondary phases as well as the kesterite structure CZTS in the figures.
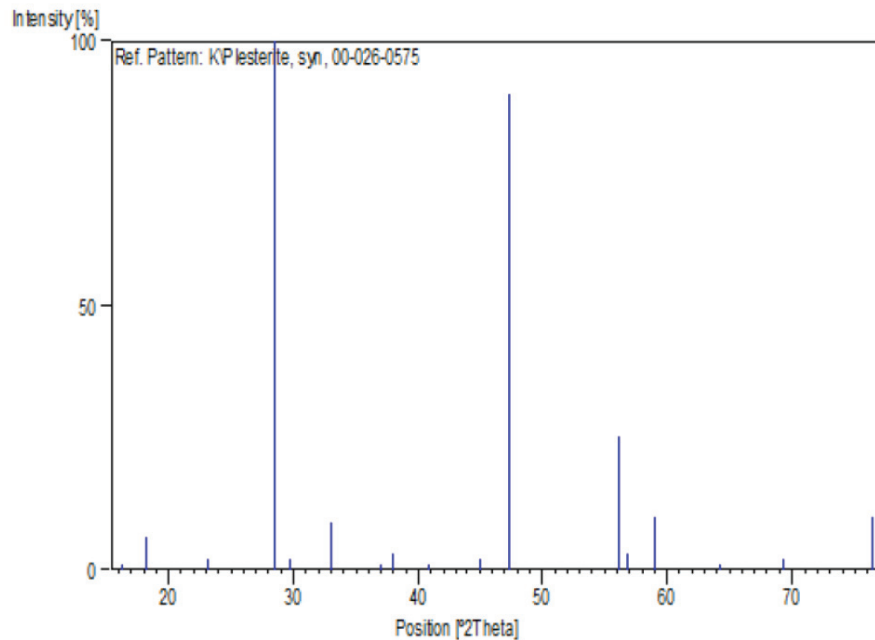
Figure 4.9. Reference XRD pattern of Kesterite CZTS
(Source: JCPDS card number 026-0575)

In Figure 4.10, the XRD patterns of CZTS-A was corresponding to the kesterite structure CZTS (JCPDS card number 026-0575). Additionally, it is show that Sn-rich composition leads to Sn-based binary secondary phase formations were observed in some regions.

Figure 4.11 shows that the XRD peaks relevant with the main peaks of kesterite structure CZTS. Furthermore, a few small peaks at 37.10^o (202), 38.00^o (211), 44.09^o (105) and the (213) peaks suggest the formation of the kesterite CZTS structure (Schorr, 2007). The main peaks were observed more distinct after the KCN etching, and also new peaks were occurred related to CZTS. On the other hand, Sn-rich composition leads to Sn-based binary secondary phase formations increased after the etching process.
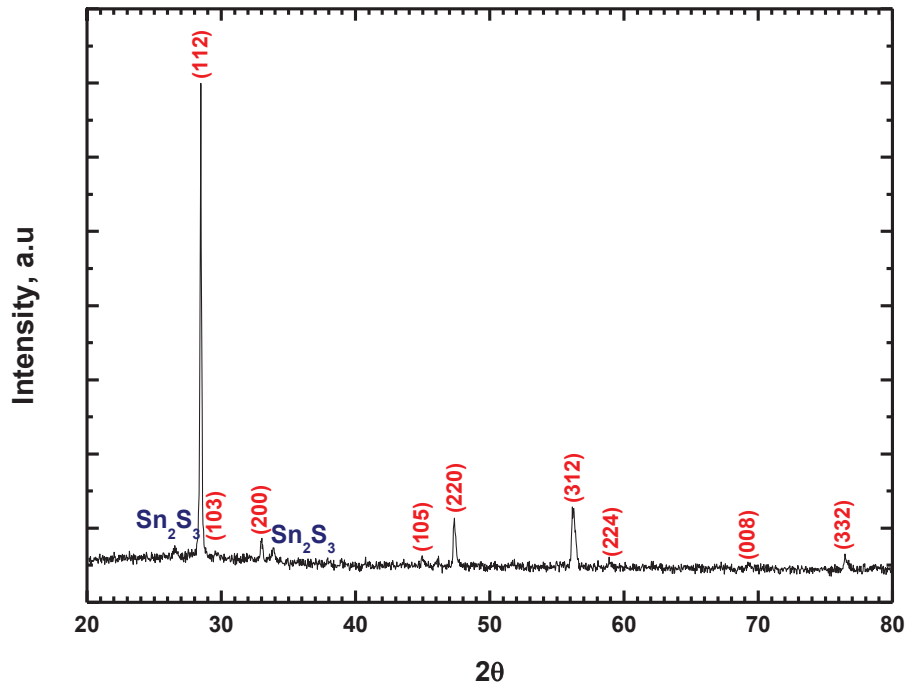
Figure 4.10. X-Ray Diffraction of CZTS-A
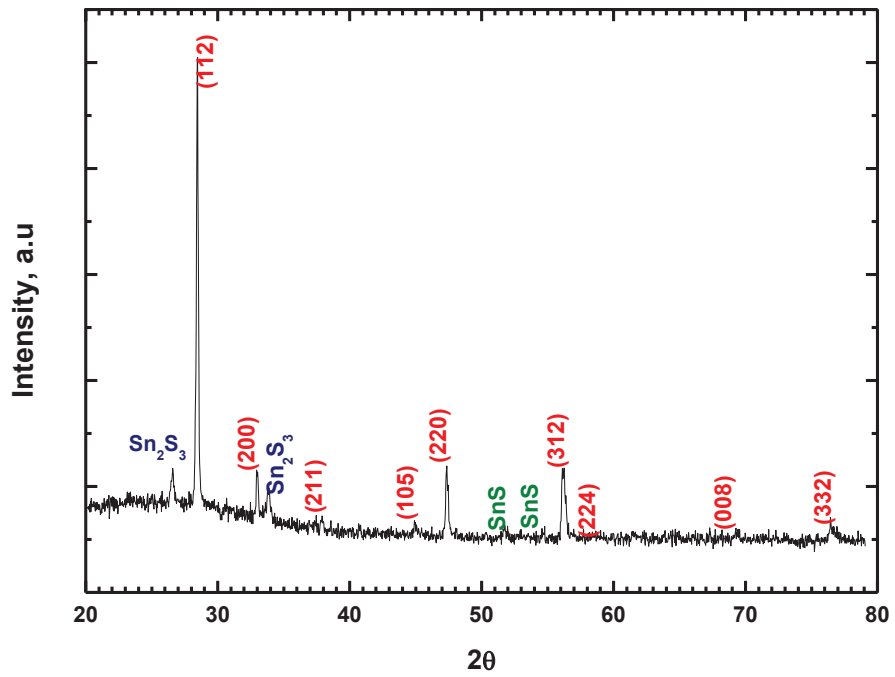
Figure 4.11. X-Ray Diffraction of CZTS-A- after KCN

47

In Figure 4.12, we observed a preferential orientation (112), and other peaks related to kesterite structure for CZTS-B sample. On the other hand, SnS_2 secondary phases were observed.
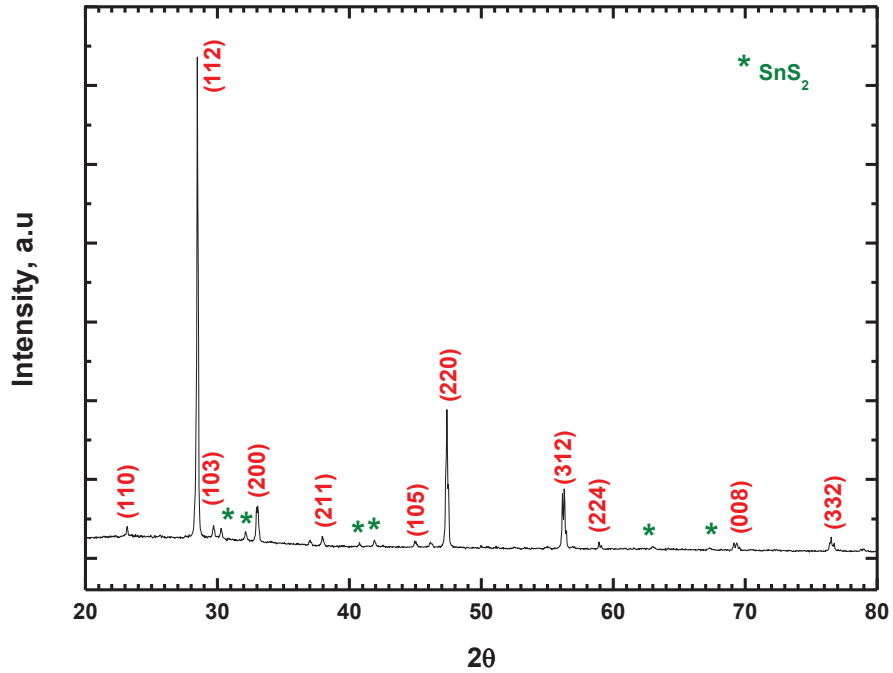
Figure 4.12. X-Ray Diffraction of CZTS-B

We can see that CZTS-C samples is not pure kesterite structure. The main peak (112) was observed at $\theta=28.57^\circ$. Also, this sample had secondary phases (Sn_2S_3) and oxide peak (SO_2), in Figure 4.13.

The preferential (112) peak and other CZTS structure related peaks for CZTS-D (Figure 4.14). This sample shows the existence of a crystalline SnS phase.
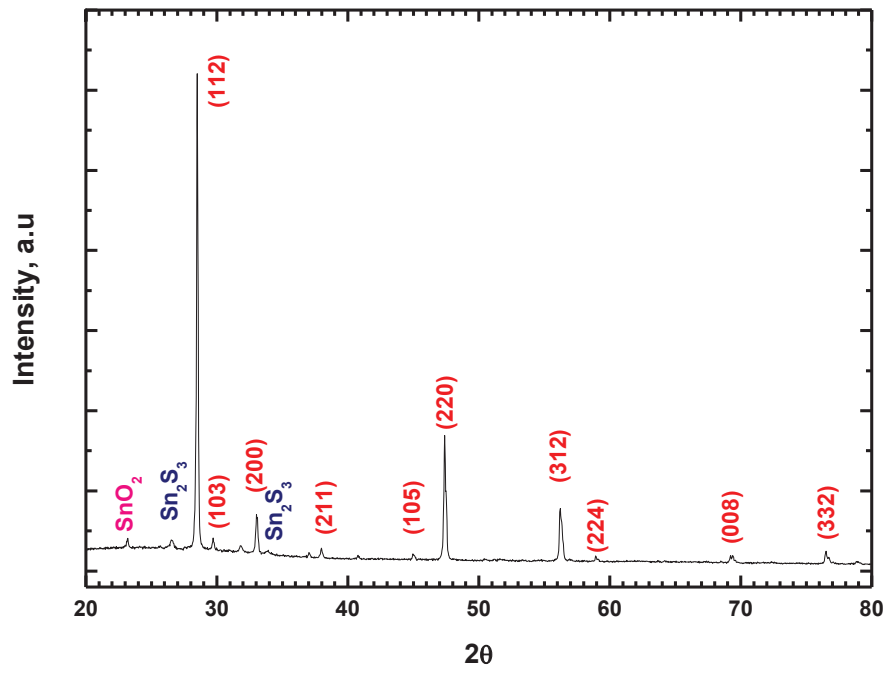
Figure 4.13. X-Ray Diffraction of CZTS-C
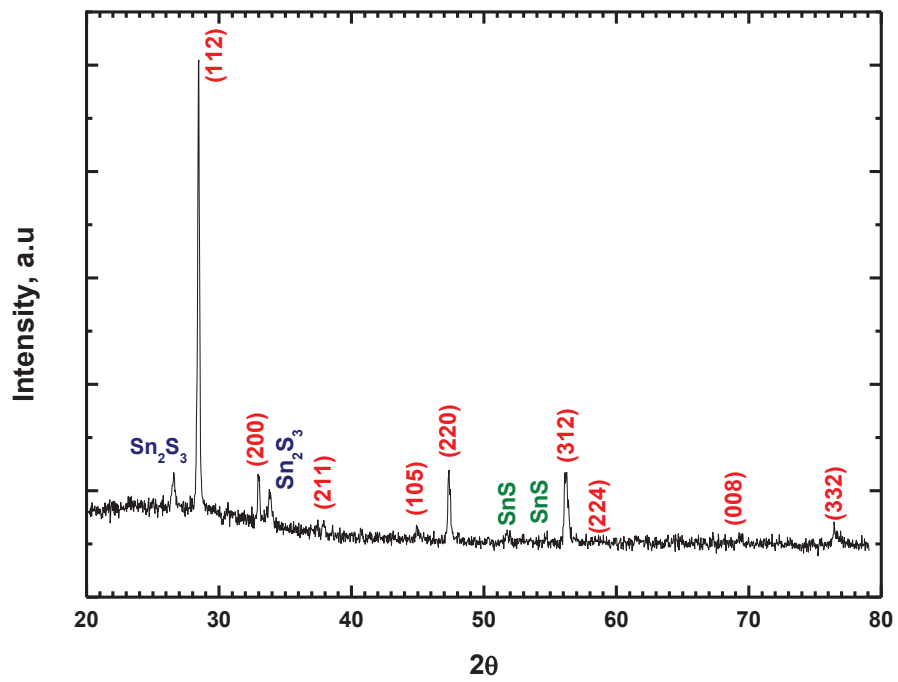
Figure 4.14. X-Ray Diffraction of CZTS-D
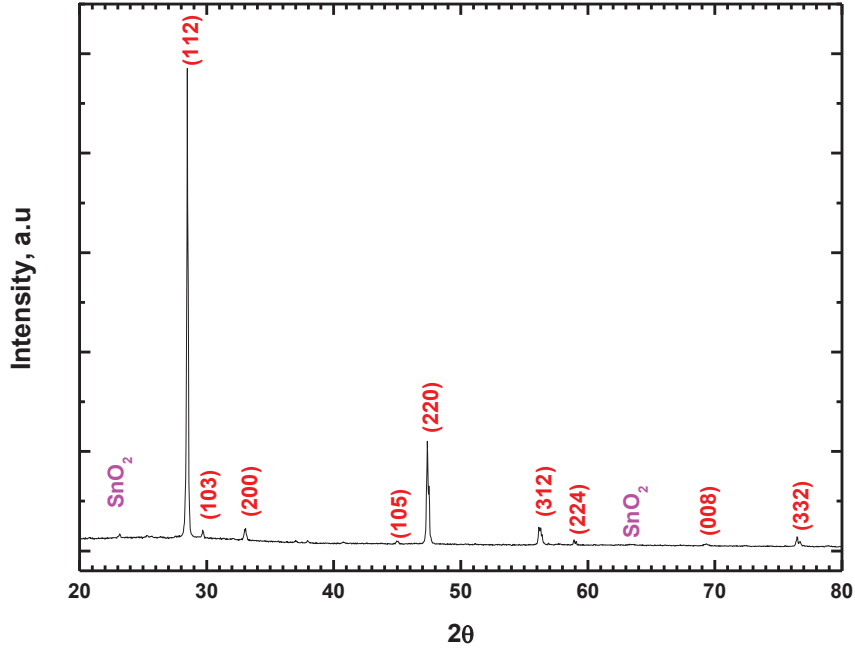
Figure 4.15. X-Ray Diffraction of CZTS-E

Figure 4.15 shows that the XRD peaks relevant with the main peaks of kesterite structure for CZTS-E. Also, we observed secondary phase as SnO_2.

4.2.2. Raman Spectroscopy Analysis

Before discussing the analysis of Raman spectroscopy, we should take into consideration which regions is occurred in Raman active or IR active for CZTS phases. The number of vibrational modes, their symmetries and the selection rules for IR absorption or Raman scattering could be determined using the basic group theoretical methods which may be employed to determine crystal selection rules. The vibrational properties are determined by calculating the Brillouin-zone-center phonon frequencies for the kesterite and stannite structures of CZTS. The structures have a total of 24 modes where there are eight atoms per primitive cell. Three of which are acoustic modes and also they are equal to zero at the zone center. We can write the representation of Brillouin-zone-center phonon modes in kesterite structure as

$$\Gamma = 3A \oplus 6B \oplus 6E \qquad (4.1)$$

for optical and

$$\Gamma_{ac} = 1B \oplus 1E \qquad (4.2)$$

for acoustic. Correlatively, it can be written for stannite structure as

$$\Gamma = 2A_1 \oplus 1A_2 \oplus 2B_1 \oplus 4B_2 \oplus 6E \qquad (4.3)$$

for optical and

$$\Gamma_{ac} = 1B_2 \oplus 1E \qquad (4.4)$$

for acoustic. In there, the E modes are doubly degenerate and other modes A, B, A_1, A_2, B_1, and B_2 are nondegenerate. In the kesterite structure, B and E modes are both infrared (IR) and Raman active. On the other hand, A mode is only Raman active. In the stannite structure, B_2 and E modes are both IR and Raman active, while modes A_1 and B_1 are only Raman active. Additionally, A_2 mode is neither IR nor Raman active. For this reason, the A_2 mode is known the silent mode.

Table 4.7 shows the data obtained from theoretical calculations for Kesterite and stannite CZTS structure (Gürel et al., 2011; Khare et al., 2012). In experimental Raman analysis, TO modes detect easier than LO modes. TO modes are detected from the surface, whereas LO modes are detected at deeper or inclined plane. When we investigate deeply, kesterite structure is more stable than stannite structure according to experimental results in the literature. Because A_1, A_2, B_1 and B_2 which are stannite structure modes show the splitting of structure.

Table 4.7. The calculated Γ-point phonon frequencies (in cm^{-1}) values for CZTS kesterite and stannite structure (Source: Gürel et al., 2011; Khare et al., 2012).

Kesterite			Stannite		
Symmetry	Wavenumber (cm^{-1})		Symmetry	Wavenumber (cm^{-1})	
A	340.04/335.2		A$_1$	334.08/332.7	
	284.30/309.0			277.12/309.1	
	272.82/302.1		A$_2$	263.11/304.3	
B(TO LO)	355.80/354.8	374.05/366.4	B$_1$	291.12/324.1	
	309.56/332.7	313.19/336.1		74.17/88.1	
	238.48/269.1	254.73/285.1	B$_2$(TO LO)	360.12/358.5	370.63/364.2
	166.65/179.6	168.21/179.9		277.08/306.2	291.82/320.6
	98.82/104.2	98.83/104.3		149.69/171.0	150.91/171.1
	86.70/92.3	87.51/93.1		95.85/96.4	95.86/96.4
E(TO LO)	351.55/341.4	366.35/353.2	E(TO LO)	346.01/341.3	364.87/353.7
	281.07/309.7	293.44/314.1		264.34/305.3	275.52/311.9
	250.26/278.2	257.85/289.8		235.41/268.7	246.58/283.3
	150.53/166.1	151.05/166.2		161.68/170.9	162.63/171.0
	105.93/101.4	106.00/101.4		97.34/106.9	97.38/106.9
	83.64/79.2	83.65/79.2		78.39/74.9	78.73/75.5

Compared to the previous experimental studies, the Raman measurements from CZTS semiconductor compounds obtained by different synthesized methods (Altosaar et al., 2008; Fernandes et al., 2009; Gürel et al., 2011; Mitzi et al., 2011; Khare et al., 2012; Yazici et al., 2015), the most intense A mode has been observed between 331 and 338 cm^{-1}. The most of recent studies show that kesterite structure is determined at 338 cm^{-1} for A mode CZTS (Altosaar et al., 2008; Fernandes et al., 2009; Cheng et al. 2011). Besides, the most recent publication related to the kesterite CZTS structure shows the presence of the intensive A mode centered at 336 cm^{-1} (Yazici et al., 2015). The structural problem like local inhomogeneity is changed the location of Raman spectra peak from 338 cm^{-1} to 331 cm^{-1} or 337 cm^{-1}. Moreover, this changing of the location at CZTS Raman peaks shows occurring some splitting at structure. Grossberg et al. reported the

investigation an extra Raman feature owing to CZTS polycrystalline and the coexistence of kesterite and disordered kesterite phases (Grossberg et al., 2012). Therefore, more works should be done to determine the shift of A mode and others.

It can be distinguished that the peaks belong to which are CZTS or secondary phases. For example, despite the fact that it is identified as cubic ZnS-(LO) by stronger peak at 352 cm^{-1} (Nilsen, 1969), it is most likely CZTS-B(TO) peak (Dumcenco and Huang, 2013) as W.G. Nilsen had investigated only ZnS. Nilsen had solely researched two elements, whereas we use the complex structure in our work, so we can see many Raman peaks corresponding CZTS structure and secondary phases. In order to analyze the presence of possible secondary phases with Raman spectrum, the specific Raman modes of these phases must be known. It was reported at some published that there are Raman peaks for SnS_2 at 215 and 315 cm^{-1} (Price et al., 1999), while SnS has three peaks at 160 cm^{-1}, 190 cm^{-1} and 219 cm^{-1} (Cheng et al., 2011; Price et al., 1999) and also Sn_2S_3 has a strong peak at 307 cm^{-1} (Price et al., 1999). When looked at our samples in this work, we can conclude that both EDS and XRD analysis revealed the existence of Sn based secondary phase formation. Thus, we should take this deduction to the account while examining the results of Raman analysis.

In this work, we observed the CZTS samples that are inhomogeneous surface. By investigating deeply, we made peak fitting by Gaussian line shape at the results of Raman analysis.

Table 4.8. The experimental calculated Γ-point phonon frequencies (in cm^{-1}) values for CZTS samples

CZTS-A		CZTS-B		CZTS-C		CZTS-D		CZTS-E	
Symmetry	Wavenumber (cm^{-1})	Symmetry	Wavenumber (cm^{-1})	Symmetry	Wavenumber (cm^{-1})	Symmetry	Wavenumber (cm^{-1})	Symmetry	Wavenumber (cm^{-1})
A	334 284 271	A	332 284 272	A	288 270	A	337 286 268	A	333 285 308
				A$_1$	331	A$_1$	328 308 277		
B(TO)	319 356	B(TO)	356	B$_1$	323	B(TO)	-	B(TO)	-
				B$_2$	356				
B(LO)	326 368	B(LO)	-	B(LO)	311	B(LO)	318 353 369	B(LO)	-
E(TO)	252 343	E(TO)	-	E(TO)	281 348	E(TO)	-	E(TO)	-
E(LO)	298	E(LO)	298	E(LO)	257 297	E(LO)	256 297 345 363	E(LO)	257

The Figure 4.16 belongs to CZTS-A and it shows the Raman modes with peak fitting. The most intense Raman mode is at 334 cm^{-1}, the full width at half maximum of the A$_1$ peak at 334 cm^{-1} is large W= 8.7 cm^{-1}, indicating a disorder in the phase related to this peak (Grossberg et al. 2012). The peak is observed the vibration of S atoms having A symmetry of the disordered kesterite structure. The A peak for the kesterite structure is shifted by 2 cm^{-1} due to the peak broadening of stannite structure peak. The second most intense Raman mode is at 284 cm^{-1}, the width of A mode is W=10.35 cm^{-1}, revealing the kesterite structure. Then the other most intense Raman peak located at 271 cm^{-1} and having the quite large width W=10.71 cm^{-1}. And the last more intense Raman peak is B(LO) symmetry (W=8.05 cm^{-1}) at 368 cm^{-1}. Although the calculated A mode of CZTS kesterite structure is an excellent match to the experimentally observed peak, the existence of the A$_1$ mode of stannite structure which is shifted from the A mode of kesterite structure cannot be ruled out due to peak broadening. According to the theoretical selection rules, the values of A symmetry are observed to be 334, 284 and 271 cm^{-1}; B(TO) symmetry are 319 and 356 cm^{-1}; B(LO) symmetry are 326 and 368 cm^{-1}; E(TO) symmetry are 252 and 343 cm^{-1}; E(LO) symmetry is 298 cm^{-1}. The results reveal the kesterite structure.
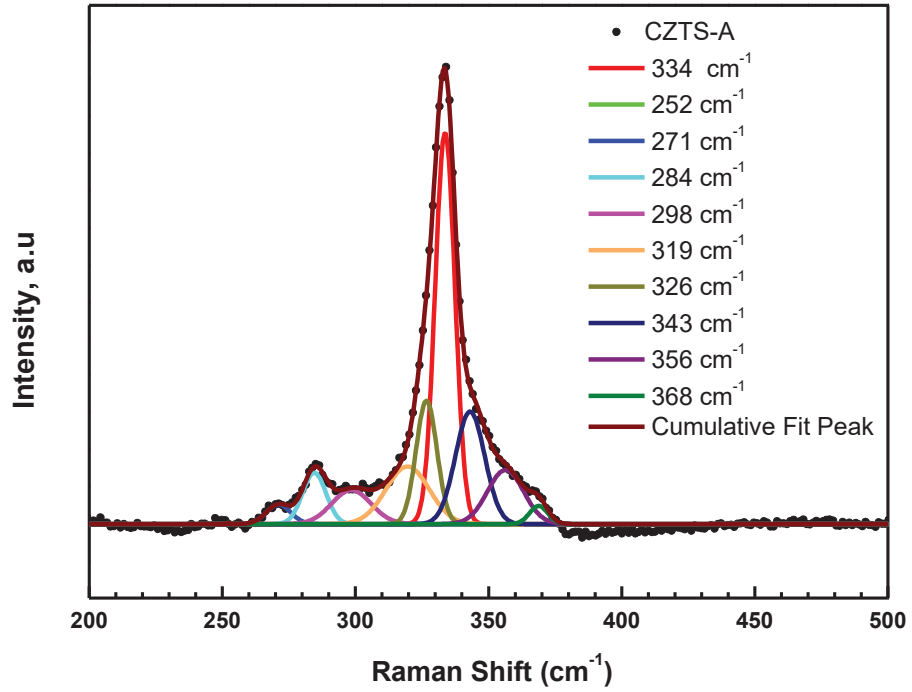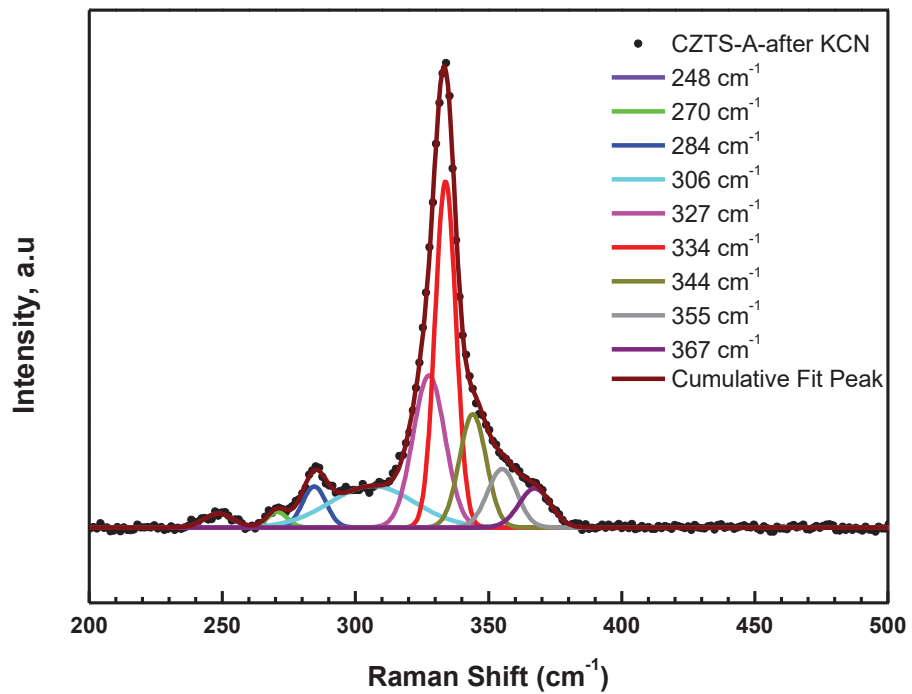
Figure 4.16. Raman Spectra of CZTS-A

Figure 4.17. Raman Spectra of CZTS-A- after KCN

Figure 4.17 shows the Raman scattering analysis of CZTS-A after etching KCN. Looking at the sample CZTS-A-after KCN, we observed that the positions of the main peaks did not change. But, the all peak positions are shifted about 1cm^{-1} owing to peak broadening.

Figure 4.18. Raman Spectra of CZTS-B

In Figure 4.18, the Raman main peak located at 332 cm^{-1}, the width of A mode is W=19.72 cm^{-1}. This peak can be attributed to the A mode of kesterite structure that is shifted by 3 cm^{-1} due to the peak boarding of stannite structure peak. Actually, the structure is disorder kesterite structure. Because other peaks are located at peak boarding of kesterite structure. According to the Raman analysis results, the value of A symmetry are observed 332, 284 and 272 cm^{-1}; B(TO) symmetry is 356 cm^{-1}; E(LO) symmetry is 298 cm^{-1}.

The Raman spectra of CZTS-C is shown in Figure 4.19. Since the shifting on the main peaks is quite large, we can say that this structure has a mixed rather than a disordered kesterite structure. Thus, the Raman scattering main peaks can be attributed to both A symmetry of kesterite structure at 339 cm^{-1} and A$_1$ symmetry of stannite structure at 331 cm^{-1}. The other main peaks can be attributed to A symmetry of kesterite structure

at 288 and 270 cm^{-1}; B(LO) symmetry is 311cm^{-1}; B$_1$ symmetry of stannite structure is 323 cm^{-1}; B$_2$ symmetry is 356 cm^{-1}; and E(TO) and E(LO) symmetries of kesterite structure are 281, 348 cm^{-1} and 257, 297 cm^{-1}, respectively. As a result of the Raman analysis, we estimate that the CZTS-C thin film is a mixture of 67% kesterite structure and 33% stannite structure.

Figure 4.19. Raman Spectra of CZTS- C

The Raman spectra for CZTS-D is given in Figure 4.20. The Raman scattering main peaks can be attributed to both A modes of kesterite structure at 337, 286 and 268 cm^{-1} and A$_1$ modes of stannite structure at 328, 308 and 277 cm^{-1}. The other peaks can be attributed to B(LO) modes of kesterite structure are 318, 353, 369 cm^{-1}; and E(LO) modes of kesterite structure are 256, 297, 345, 363 cm^{-1}. According to the Raman analysis, we estimate that the CZTS-D thin film is a mixture of 66% kesterite structure and 34% stannite structure.

Figure 4.20. Raman Spectra of CZTS-D

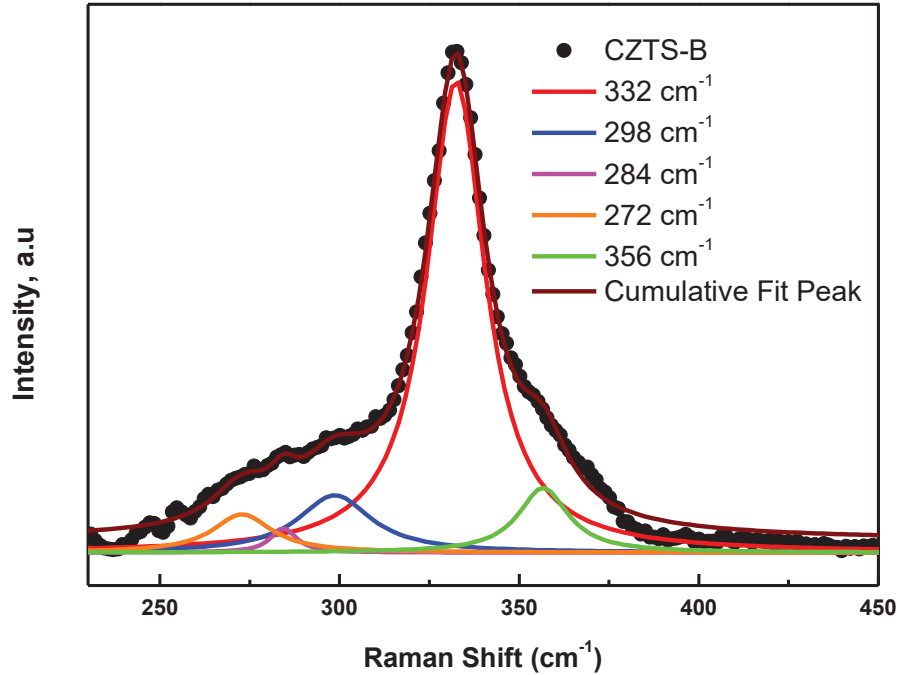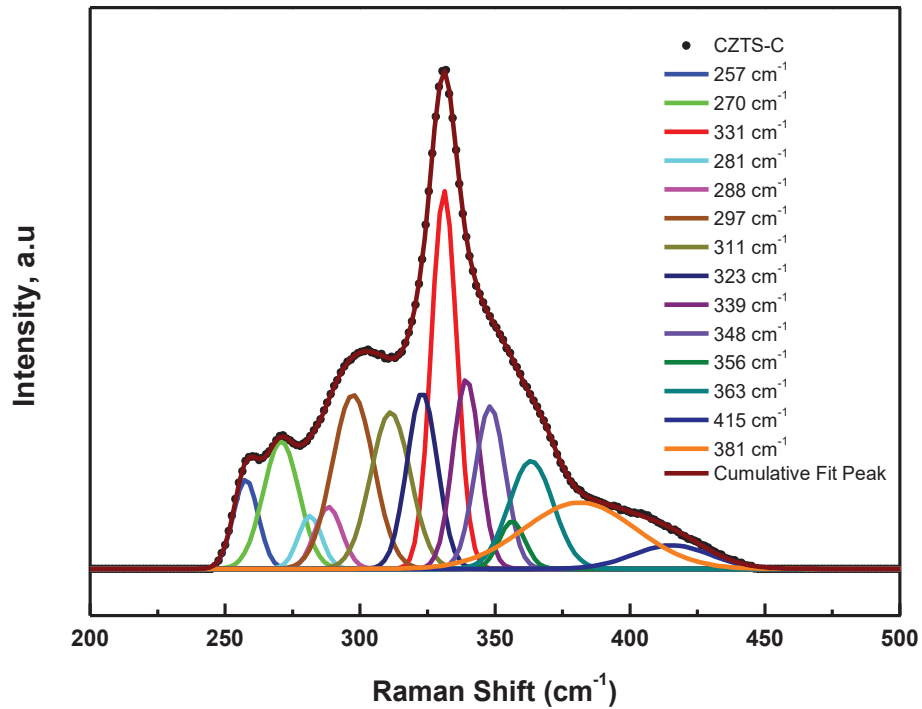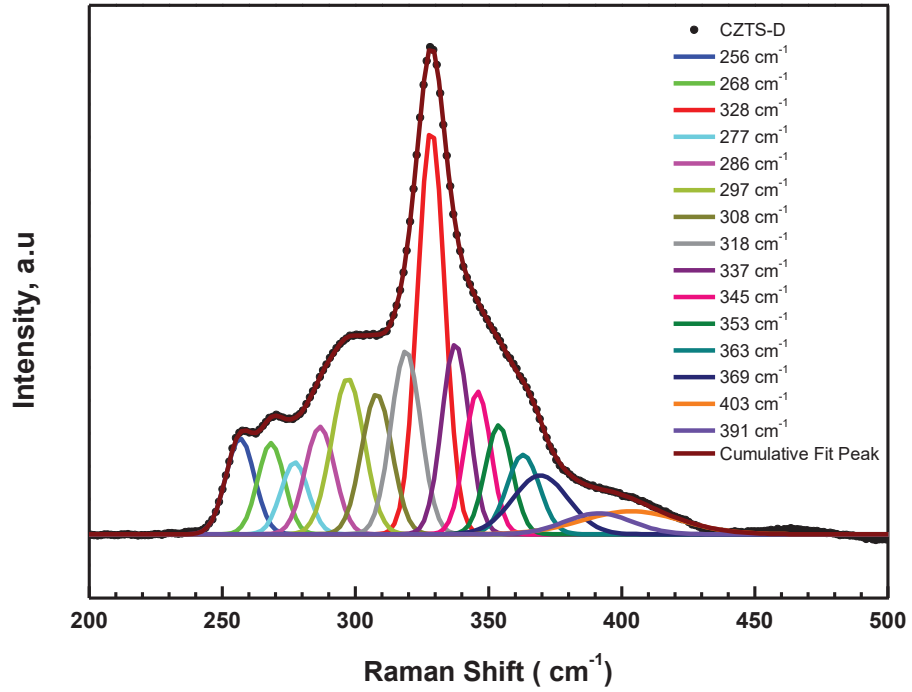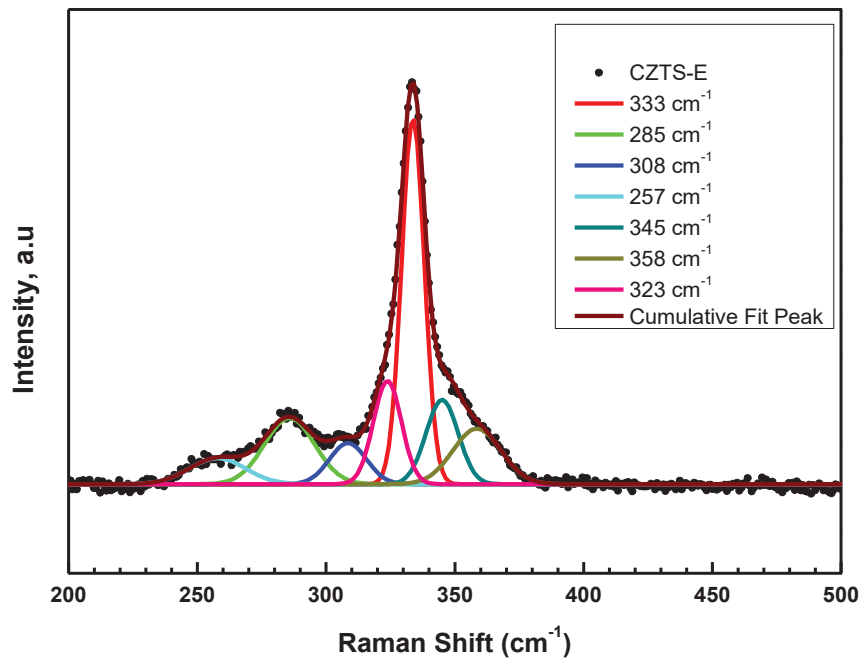Figure 4.21. Raman Spectra of CZTS-E

In Figure 4.21, the Raman main peak located at 333 cm^{-1}, the width of A mode is W=10.45 cm^{-1}. This peak can be attributed to either the A mode of kesterite at 335.2 cm^{-1} or the A$_1$ mode of stannite at 332.7 cm^{-1}. The second main intense Raman mode is at 285 cm^{-1}, the quite large width of A mode of kesterite is W=22.83 cm^{-1}.The other Raman peak is at 308 cm^{-1} and having the large width of A mode W=16.98 cm^{-1}. The last more intense Raman peak is E(LO) mode of kesterite (W=25.60 cm^{-1}) at 257 cm^{-1}.

4.3. Optical Properties

In this study, we estimated the optical and electrical properties of the absorber layer. The optical and electrical properties are substantial for the solar cell applications. Namely, the calculated values would be guide for deposition parameters. The optical band gap energy of the thin films was provided by transmittance and reflectance measurements at room temperature. The optical absorption coefficient (α) of CZTS samples are estimated using the following equation (Pankove, 1975);

$$\alpha = \frac{1}{t} \ln \left[\frac{(1-R)^2}{T} \right] \tag{4.5}$$

where t is thickness of the film, R is reflection and T is transmission data. The optical band gap energy is measured using at the 4.6 equation (Pankove, 1975);

$$(\alpha h\nu) = A\big[h\nu - E_g\big]^n \tag{4.6}$$

where α is optical absorption coefficient, A is a constant, E$_g$ is the band gap energy and n=1/2 for direct allowed transition. The optical energy band gap of CZTS thin films were determined plot of $(\alpha h\nu)^2$ vs. photon energy (Figure 4.22-26). The optical band gap of CZTS was observed to depend on sample compound and heat-treatment parameters. The straight line intercepting on the photon energy axis gives the optical band gap energy value, which is called E$_g$, as 1.58 eV for CZTS-A (Figure 4.22). The transmittance spectrum of CZTS-A is given as inset plot of Figure 4.22. According to transmittance versus wavelength graphs, while transmission of sample has 0.7–1.5% values in the

visible wavelength region, it is about 1.5–40% and approximately constant in the near infrared wavelength region.

Figure 4.22. The $(\alpha h v)^2$ versus photon energy plot for optical band gap determination; inset graph: the transmittance spectrum of a CZTS-A

Figure 4.23 shows that the optical band gap energy value (E_g) of CZTS-B is 1.50 eV. The transmittance spectrum of CZTS-B is given as inset plot of Figure 4.23. According to transmittance versus wavelength graphs, while transmission of sample has 0.01–0.23% values in the visible wavelength region, it is about 0.23–13.15% and approximately constant in the near infrared wavelength region.

Figure 4.24 refers to $(\alpha h v)^2$ versus hv plot of CZTS-C that the optical band gap energy value (E_g) is 1.59 eV. The transmittance spectrum of CZTS-C is given as inset plot of Figure 4.24. According to transmittance versus wavelength graphs, while transmission of sample has 0.01–1.10% values in the visible wavelength region, it is about 0.10–45.24% and approximately constant in the near infrared wavelength region.
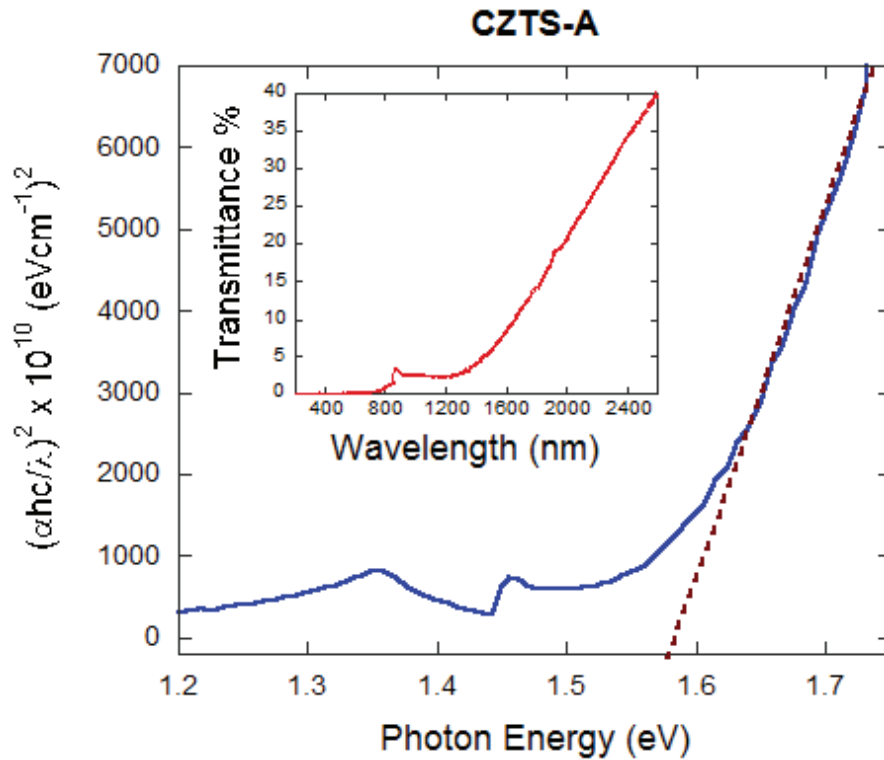
Figure 4.23. The $(\alpha h v)^2$ versus photon energy plot for optical band gap determination; inset graph: the transmittance spectrum of a CZTS-B

Figure 4.24. The $(\alpha h v)^2$ versus photon energy plot for optical band gap determination; inset graph: the transmittance spectrum of a CZTS-C

Figure 4.25 belongs to $(\alpha h\nu)^2$ vs. $h\nu$ plot of CZTS-D that the optical band gap energy value (E_g) is 1.57 eV. The transmittance spectrum of CZTS-D is given as inset plot of Figure 4.25. According to transmittance versus wavelength graphs, while transmission of sample has 0.02–2.37% values in the visible wavelength region, it is about 2.37–3.70% and approximately constant in the near infrared wavelength region.

In Figure 4.26, the optical band gap energy value, E_g, is obtained as 1.59 eV for CZTS-E. The transmittance spectrum of CZTS-E is given as inset plot of Figure 4.26. According to transmittance versus wavelength graphs, while transmission of sample has 0.01–1.72% values in the visible wavelength region, it is about 1.72–47.31% and approximately constant in the near infrared wavelength region.
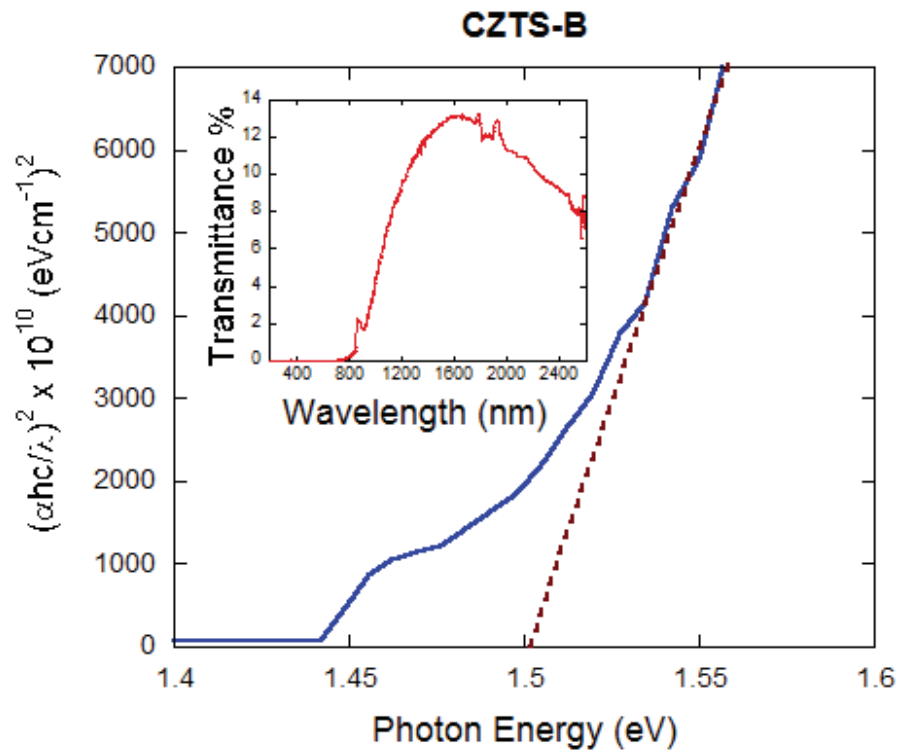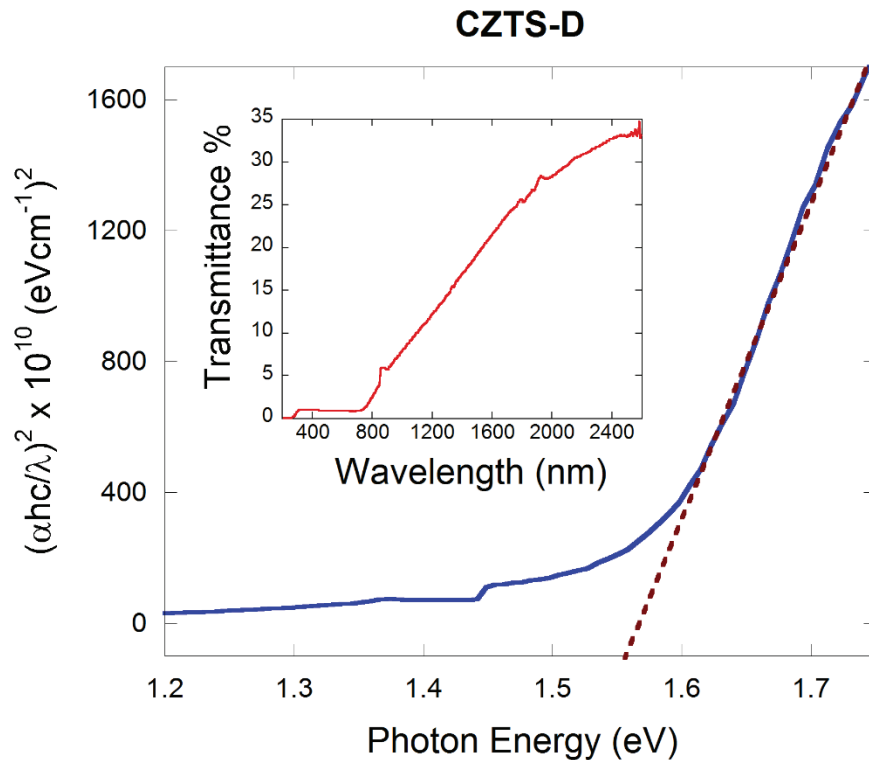

Figure 4.25. The $(\alpha h\nu)^2$ versus photon energy plot for optical band gap determination; inset graph: the transmittance spectrum of a CZTS-D
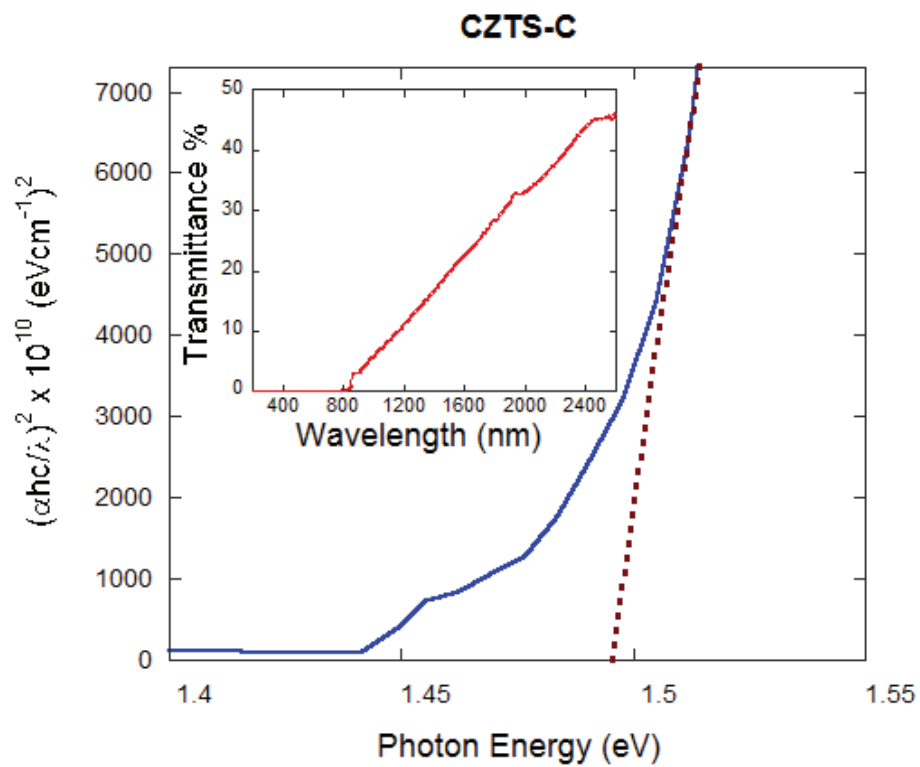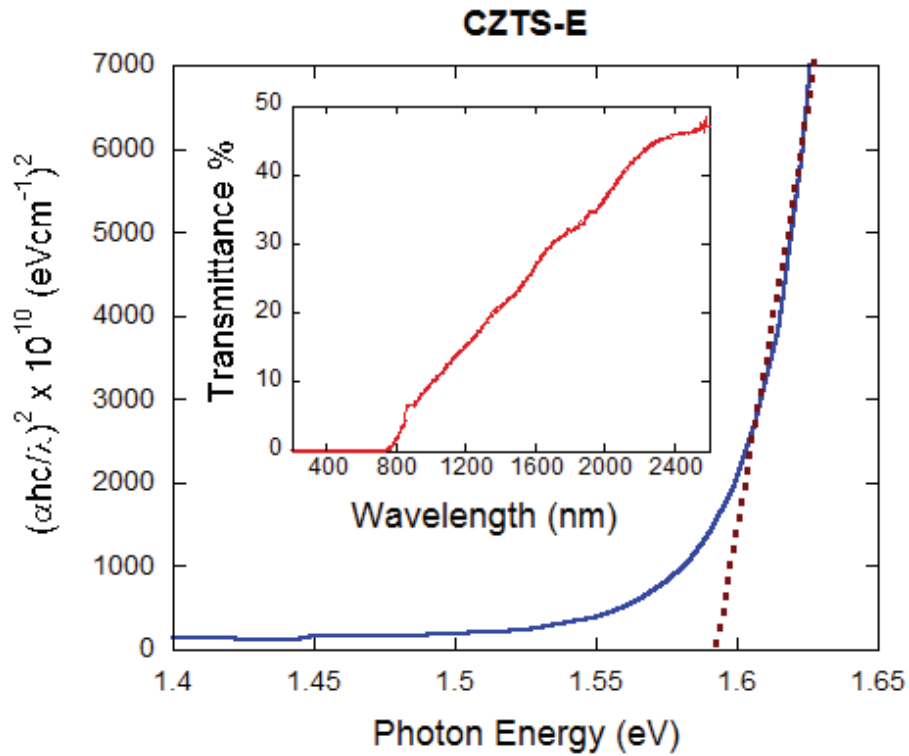
Figure 4.26. The $(\alpha h\nu)^2$ versus photon energy plot for optical band gap determination; inset graph: the transmittance spectrum of a CZTS-E

As a results, the optical properties were investigated and the optical band gap values were obtained about 1.5 eV. The value is in good agreement with the previously reported values (Li et al., 2012; Jimbo et al., 2007). It is well known that the presence of secondary phases with band gap energies higher than that of the pure CZTS thin film have an impact on the band gap energy of the CZTS thin film (Parenteau and Carlone, 1990). For the CZTS samples, the only secondary phases observed were tin sulfide compounds such as SnS, SnS_2 and Sn_2S_3. The acceptable E_g values of CZTS samples are most likely due to the low band gap energy of SnS, which has a direct band gap in the range of 1.3 - 1.42 eV and an indirect band gap of 1.1 eV (Tanusevski and Poelman, 2003). Besides, the band gap might be shifted due to formation of high band gap material, which is SnS_2 (2.2 eV), during the CZTS synthesis.

4.4. Electrical Characterization

In this section, temperature dependence of the resistivity and hall coefficient were studied in the temperature range of 80 - 300 K. We used van der Pauw method for resistivity and Hall effect measurements.

4.4.1. Measurement of Temperature Dependence Resistivity

We found that for all films resistivity versus temperature curve shows the expected semiconductor behavior. The lowest resistivity value that we found as 0.09 Ω.cm at room temperature and the highest resistivity value was found about 0.41 Ω.cm at 80 K for CZTS-A (Figure 4.27).

Figure 4.28 shows that the resistivity value of CZTS-B was estimated from 0.03 Ω.cm to 0.02 Ω.cm at 80 K to 300 K. The sample CZTS-B shows semiconductor behavior from 80 K to 220 K, and then metal behavior from 220 K to 300 K. We can say that the sample is composed highly Sn atoms. Namely, the sample is not pure kesterite structure. Thus, the defect negatively affects the electrical properties.

In Figure 4.29, the lowest resistivity value that we found as 182 Ω.cm at room temperature for CZTS-C. The highest resistivity value was found 1487 Ω.cm at 80 K. It can see clearly that the resistivity gradually increases with the decrease in temperature suggesting a semiconductor behavior.

Similarly, the resistivity gradually increases with the decrease in temperature suggesting a semiconductor behavior, in Figure 4.30. The lowest resistivity value is 0.53 Ω.cm at room temperature for CZTS-D. The highest resistivity value of CZTS-D sample is 2.11 Ω.cm at 80 K.

Figure 4.31 belongs to the samples CZTS-E-1st layer and CZTS-E. We can see that both the resistivity versus temperature curve gives a property of semiconductor behavior. In Figure 4.31 (a), the lowest resistivity value is 0.33 Ω.cm at room temperature and the highest value is 0.48 Ω.cm at 80 K. In Figure 4.31 (b), at room temperature, the lowest resistivity value is 0.56 Ω.cm. The highest resistivity value is 2.01 Ω.cm at 80 K.
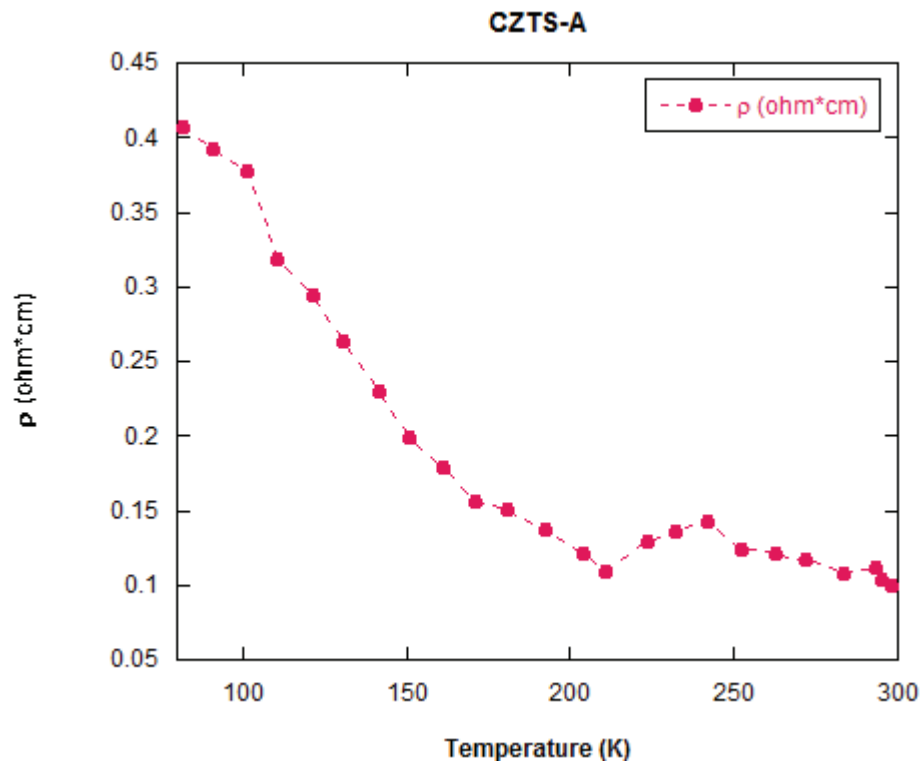
Figure 4.27. The resistivity versus temperature curve for CZTS-A
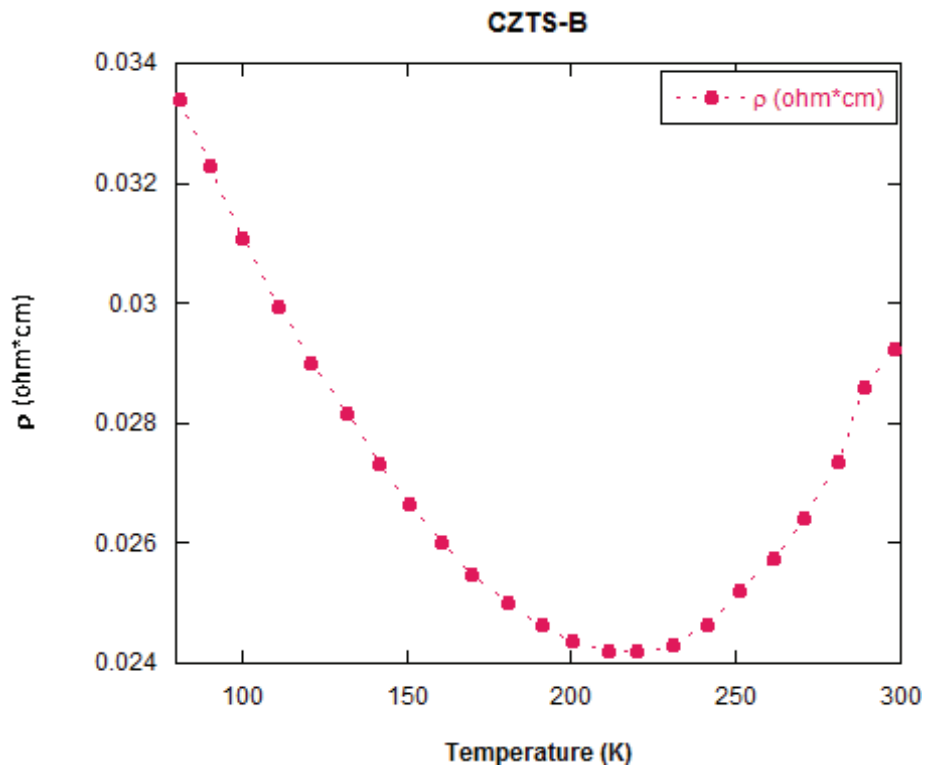
Figure 4.28. The resistivity versus temperature curve for CZTS-B
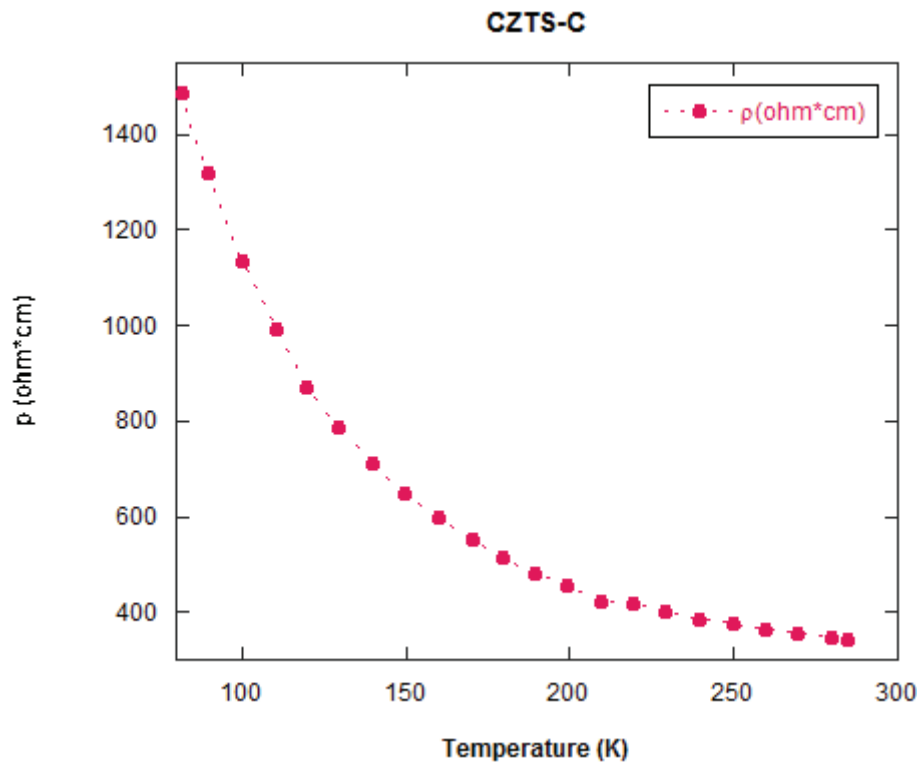
Figure 4.29. The resistivity versus temperature curve for CZTS-C

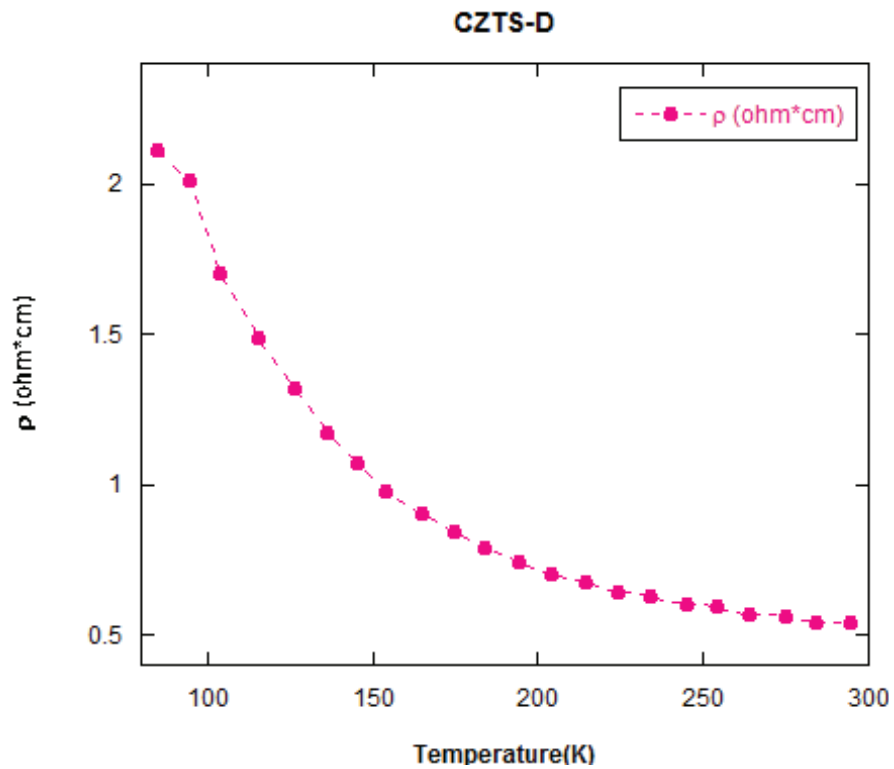Figure 4.30. The resistivity versus temperature curve for CZTS-D
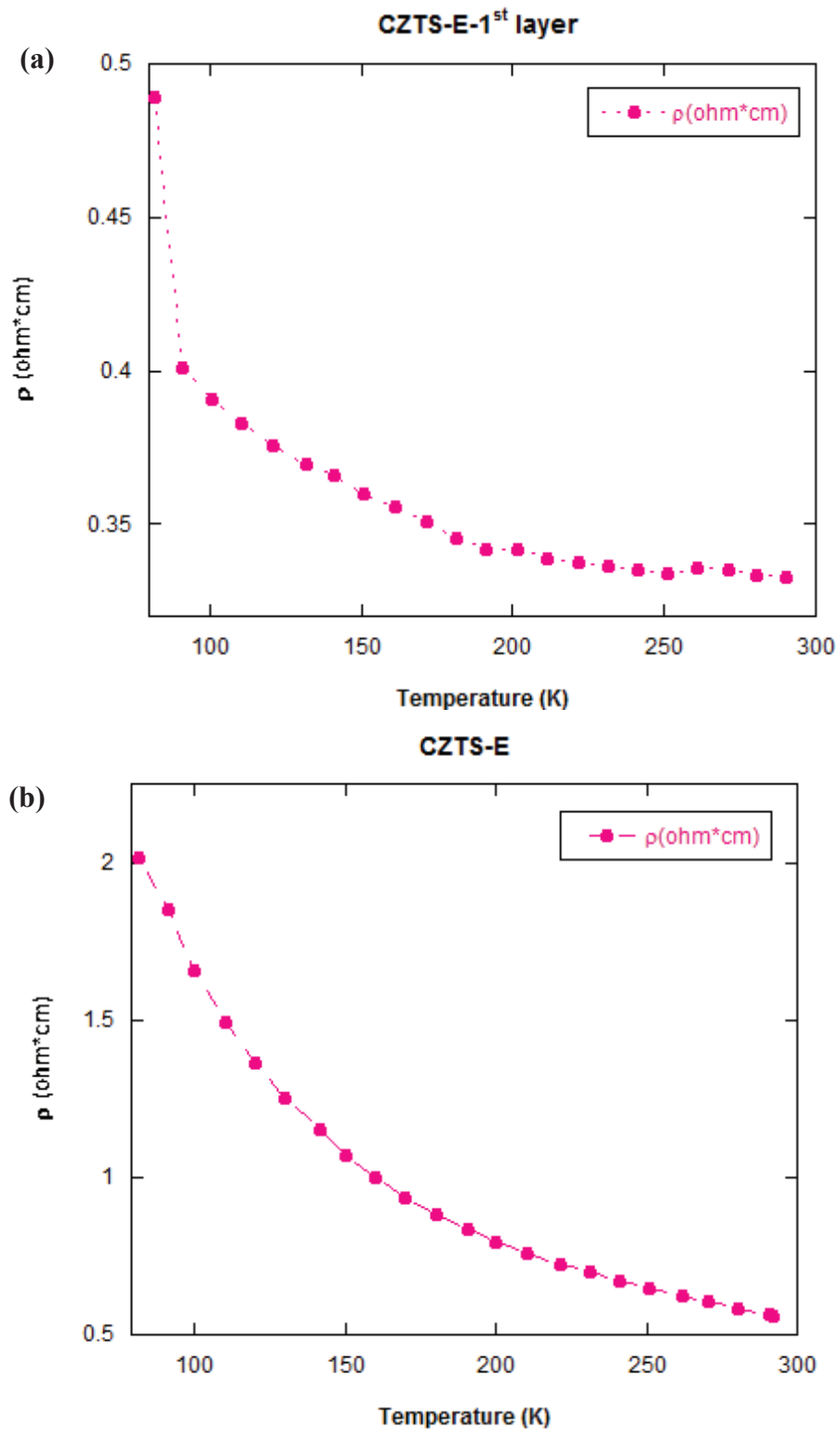
Figure 4.31. The resistivity versus temperature curve for (a) CZTS-E-1st layer (b) CZTS-E

The effect of defects (such as impurity, voids), grain size and grain boundary, etc. can be changed the resistivity values of semiconductor materials. Either decreasing or increasing in the value can be change behaviors. For example, because of impurity the

high resistivity value of CZTS-C sample shows behavior like insulator. Thus, we can say that this sample is without grain boundary because of the dense surface. On the other hand, sample CZTS-A, D and E show semiconductor behavior as suitable literature.

4.4.2. Variation of Hall Coefficient with Temperature

Temperature dependence of CZTS thin films we measure Hall coefficient by changing temperature from 80 K to room temperature using van der Pauw configuration. The Hall coefficient data were calculated using LabVIEW program (Figure 4.38).
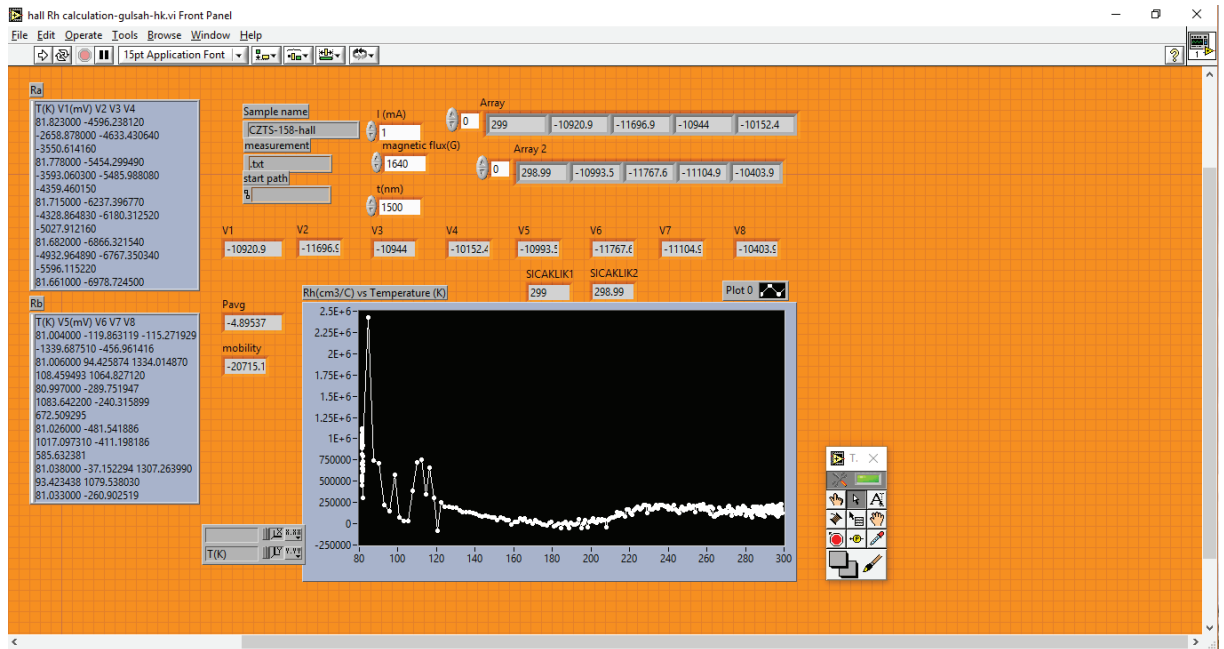
Figure 4.38. The image of labview program for Hall coefficient calculation

All Hall coefficient vs temperature graphs were done polynomial curve fitting. Different degree polynomials curves were occurred for each graph. These were second degree polynomial curve for CZTS-A, ninth degree polynomial curve for CZTS-B, third degree polynomial curve for CZTS-C, eighth degree polynomial curve for CZTS-D and fourth degree polynomial curve for CZTS-E. Namely, we can say that the graphs for all sample are nonlinear and they have irregular fluctuations.

On the other hand, positive values of measured Hall coefficient demonstrated that all samples were p-type. The Hall coefficient almost linearly decreases with the increase

in temperature suggesting p-type semiconductor behavior, in Figure 4.39. The Hall coefficient value of CZTS-A sample is 2.34 cm^3/C at room temperature.
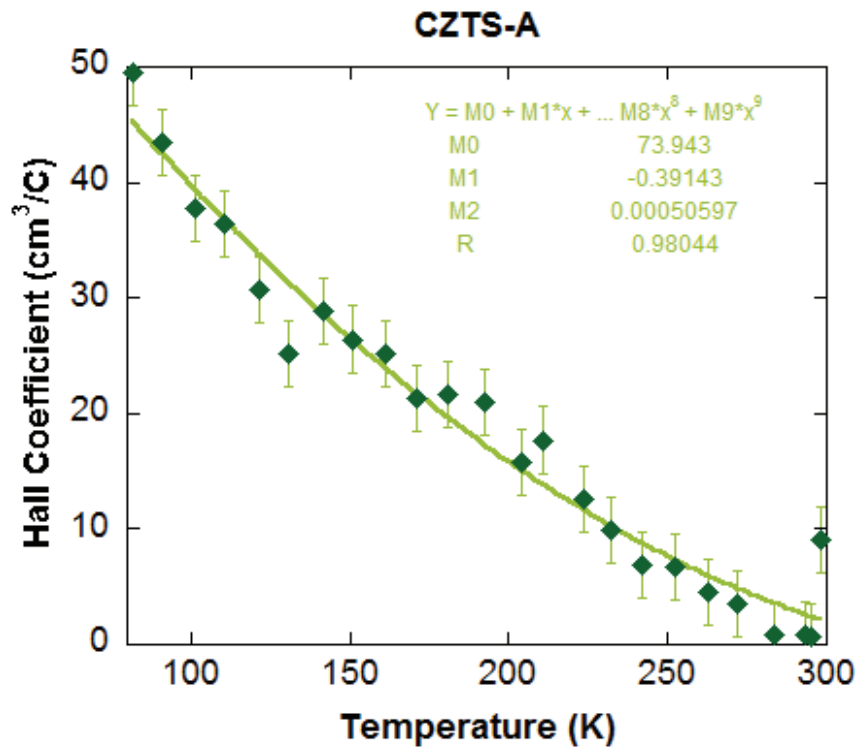
Figure 4.39. Hall coefficient versus temperature curve for CZTS-A

The Hall coefficient dramatically decreases (except among 140 K and 210 K) with the increase in temperature suggesting p-type semiconductor behavior (Figure 4.40). At room temperature, Hall coefficient value is 0.29 cm^3/C for CZTS-B.

We observed that the Hall coefficient decreased till 180K, which slowly increased until the room temperature with the measured temperature (Figure 4.41). Since CZTS-C thin film is p-type semiconductors as the graph. Also, the Hall coefficient value is 111.18 cm^3/C at room temperature.
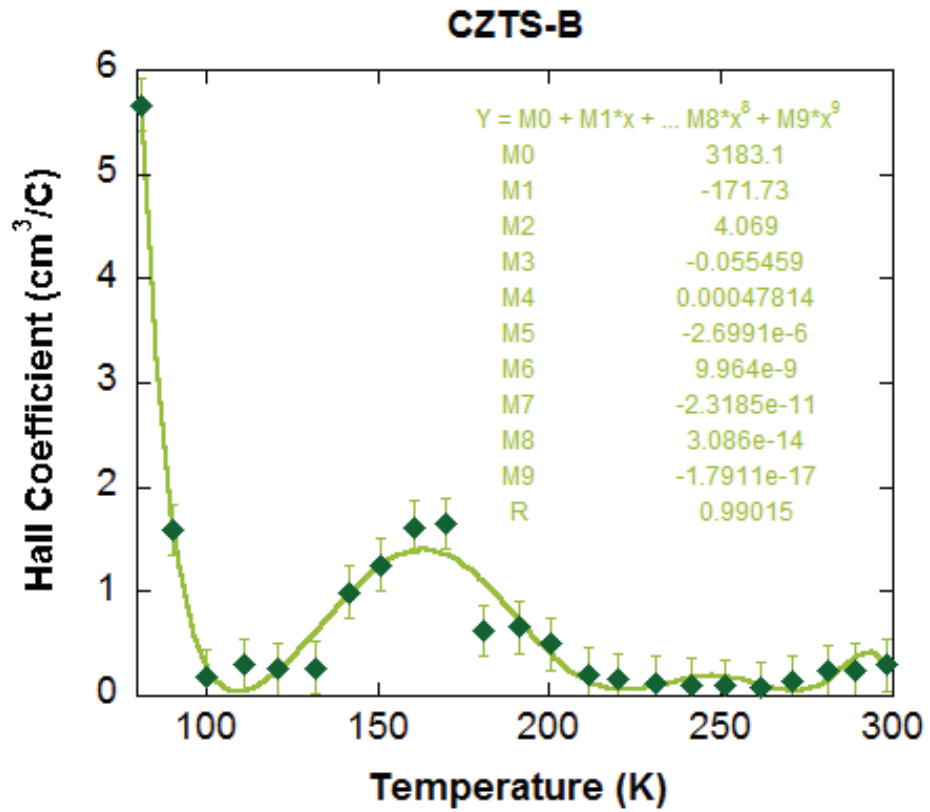
Figure 4.40. Hall coefficient versus temperature curve for CZTS-B
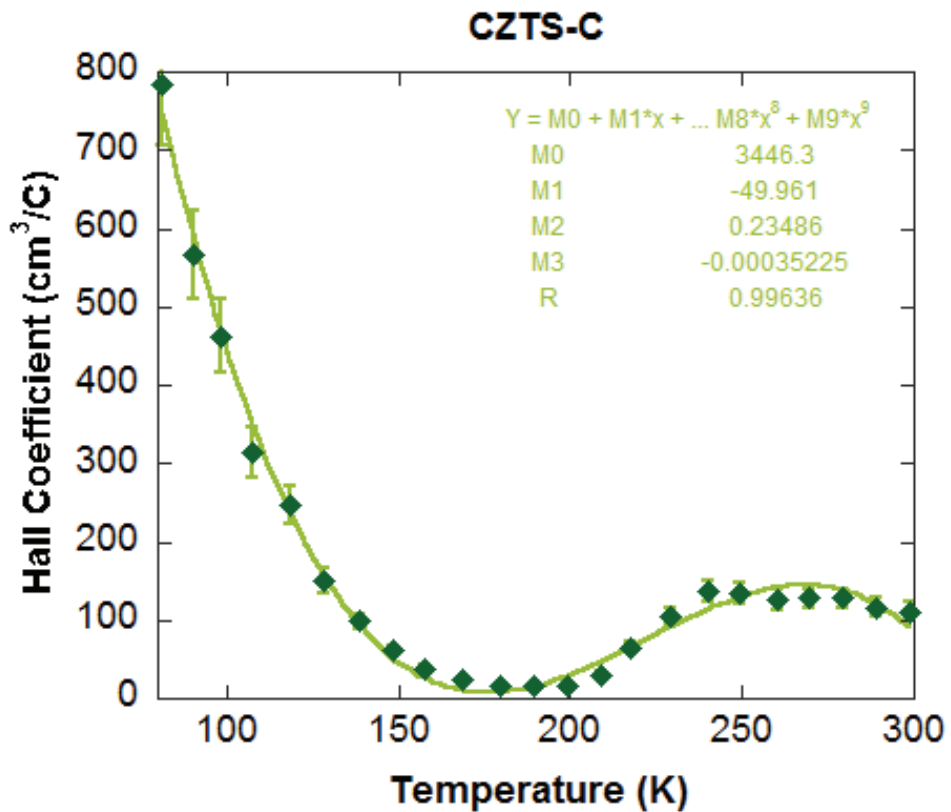
Figure 4.41. Hall coefficient versus temperature curve for CZTS-C
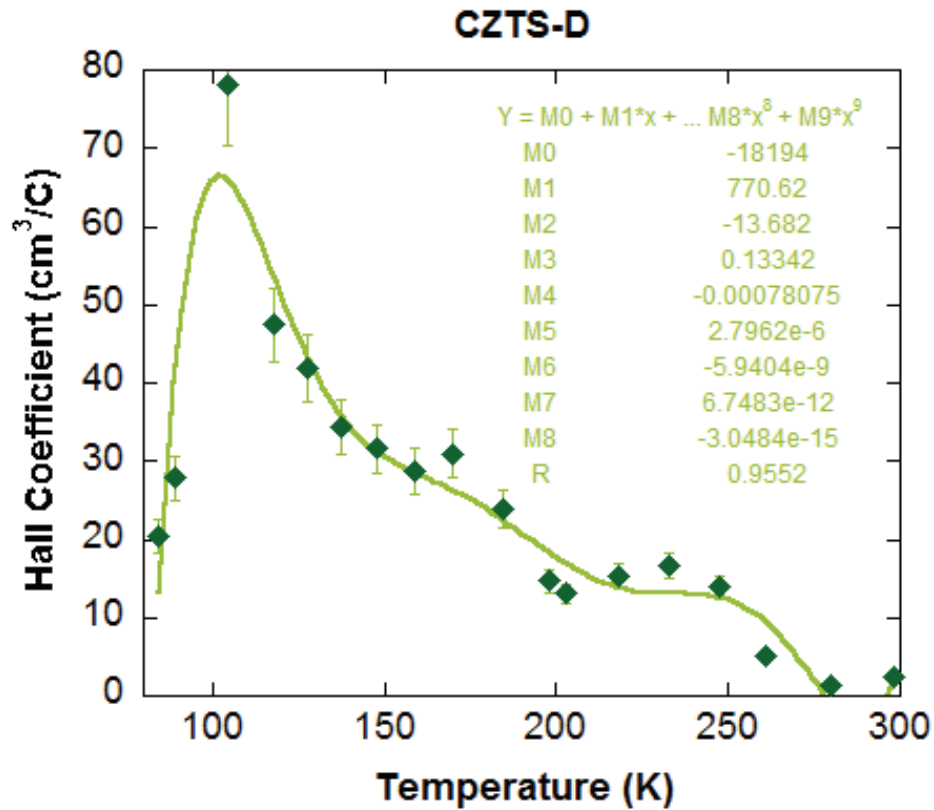
Figure 4.42. Hall coefficient versus temperature curve for CZTS-D

In Figure 4.42, after the curve at 100 K, the Hall coefficient almost linearly decreases with the increase in temperature suggesting p-type semiconductor behavior for CZTS-D sample. At room temperature, the Hall coefficient value is 2.56 cm^3/C.

Figure 4.43 shows the Hall coefficient fluctuating increase with the increase in temperature for CZTS-E-1st layer, and the Hall coefficient almost linearly decreases with the increase in temperature for CZTS-E, also suggesting p-type semiconductor behavior. For 1st layer, hall coefficient value is 60.48 cm^3/C (Figure 4.43 (a). Conversely, CZTS-E sample has 0.02 cm^3/C Hall coefficient at room temperature (Figure 4.43 (b).
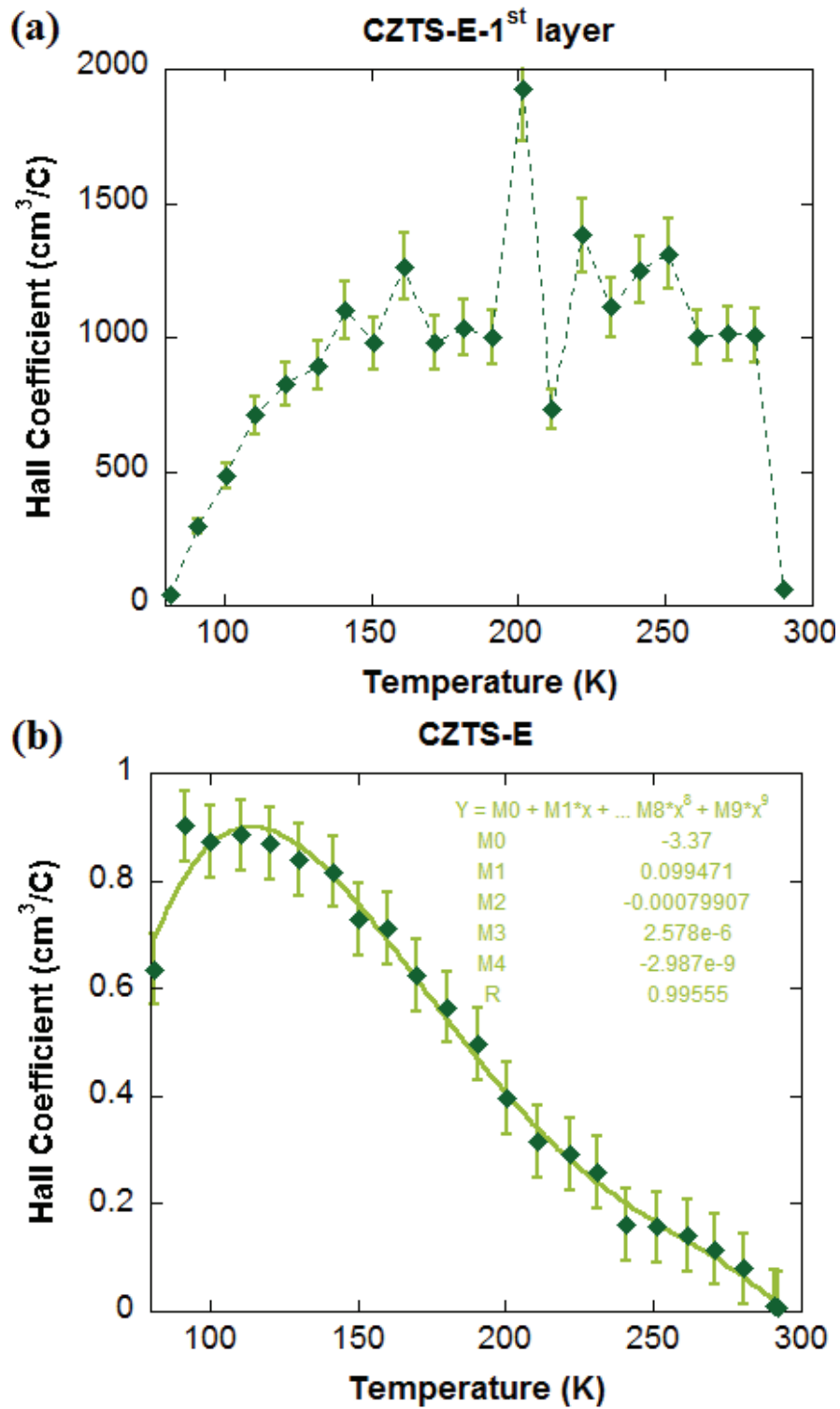
Figure 4.43. Hall coefficient versus temperature curve for (a) CZTS-E-1st layer (b) CZTS-E

4.4.3. Temperature Dependence of Carrier Concentration and Hall Mobility

Hall effect measurement results showed that the hole mobility of CZTS changed from lower than 1 to as high as 0.01 cm^2/V.s at room temperature in this work, while most published values were in the range of 1 to 10 cm^2/V.s at room temperature (Rajeshmon et al., 2011; Ito and Nakazawa, 1988; Liu et al., 2010; Chan et al., 2010; Xinkun W et al., 2012). On the other hand, some published works figured out the hole mobility values as 0.1- 60 cm^2/V.s (Ito, 2015; Zhao et al., 2017). Lower mobility indicates that the optimized thickness of absorber layer in CZTS thin film solar cells. Hall mobility and carrier concentration of CZTS thin films calculated using results of Hall coefficient measurement for approximately 1500 nm thick samples. The carrier concentration was calculated considering the formulation of $R_H = 1/(n*e)$ where R$_H$ is hall coefficient and n is an electron charge which is 1.602×10^{19} Coulombs. Table 4.9 shows the hole mobility, carrier concentration and resistivity values of all CZTS samples in our work at room temperature.

Table 4.9. The hole mobility, carrier concentration and resistivity values for CZTS samples at room temperature

Samples	CZTS-A	CZTS-B	CZTS-C	CZTS-D	CZTS-E
Mobility (cm^2/V.s)	5.74	10.04	0.32	4.74	0.04
Carrier Concentration (cm^{-3})	1.04×10^{19}	2.12×10^{19}	5.62×10^{16}	2.44×10^{18}	2.83×10^{20}
Resistivity (Ω.cm)	0.09	0.02	182	0.53	0.56

For CZTS-A sample, the lowest hole mobility value was measured as 5.74 cm^2/V.s at room temperature and the highest hole carrier concentration value was found 1.04×10^{19} cm^{-3}. A decrease in value of hole mobility was seen and contrary to an increase in value of carrier concentration was observed (Figure 4.44).

Figure 4.44. Variation of carrier concentration and Hall mobilities with temperature for CZTS-A
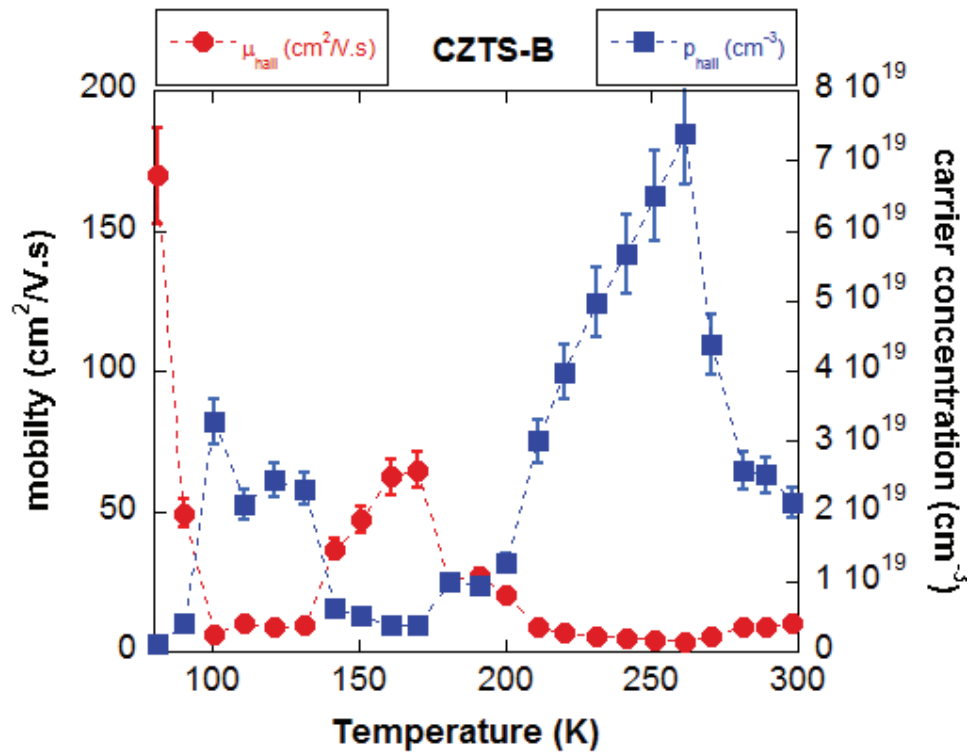
Figure 4.45. Variation of carrier concentration and Hall mobilities with temperature for CZTS-B

Carrier mobility and concentration versus temperature graphs depend on impurities on sample structure (Zhao et al., 2017). Namely, secondary phases impresses the electrical properties, negatively. Therefore, an irregular fluctuation was observed at Figure 4.45. The hole mobility value was measured as 10.04 cm^2/V.s at room temperature. The carrier concentration value was estimated 2.12×10^{19} (cm^{-3}) at room temperature.

It was observed that the carrier concentration increases until nearly 180 K and then which decreases to the room temperature seen in Figure 4.46. On the other hand, the hall mobility was observed decreases until about 180 K after then increases Figure 4.46. For CZTS-C sample, the hole mobility value was measured as 0.32 cm^2/V.s and the hole carrier concentration value was found 5.62×10^{16} cm^{-3} at room temperature.
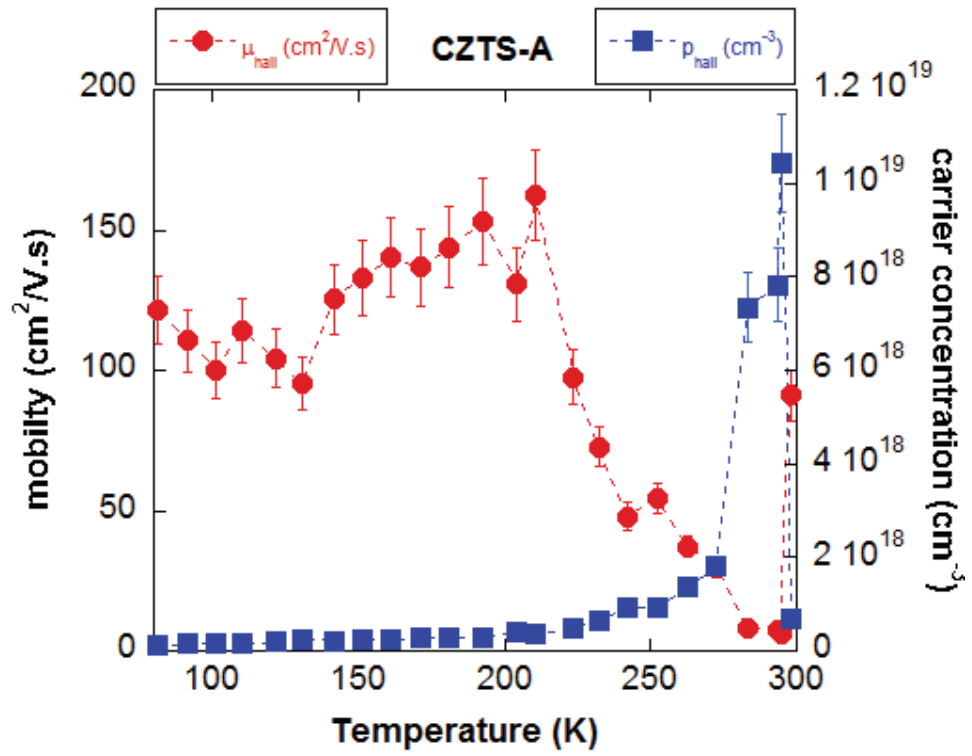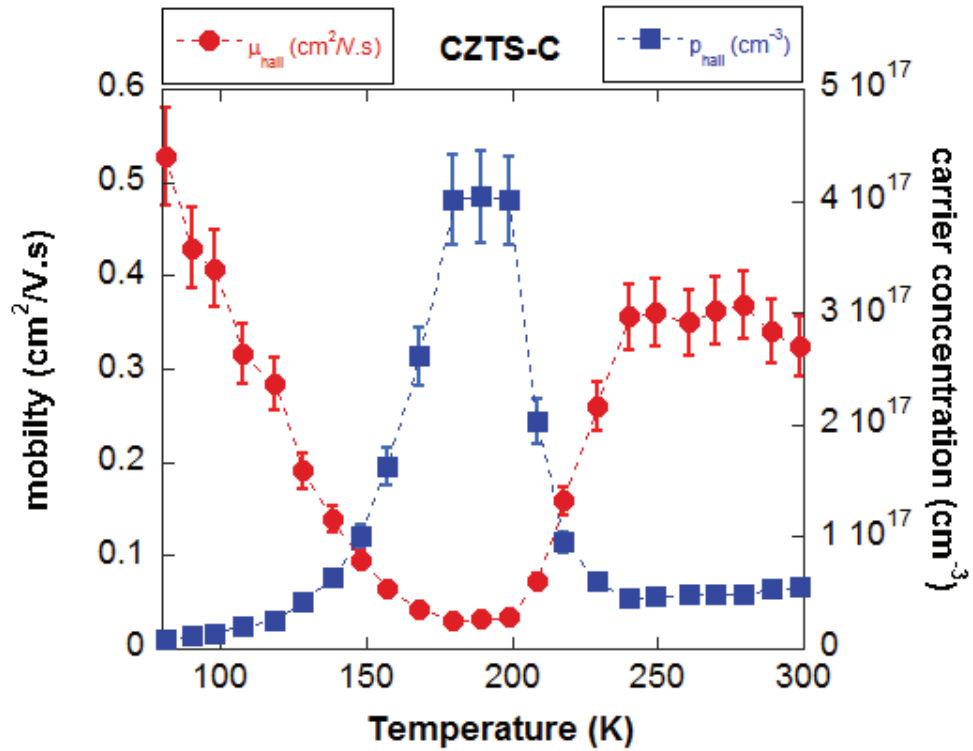

Figure 4.46. Variation of carrier concentration and Hall mobilities with temperature for CZTS-C
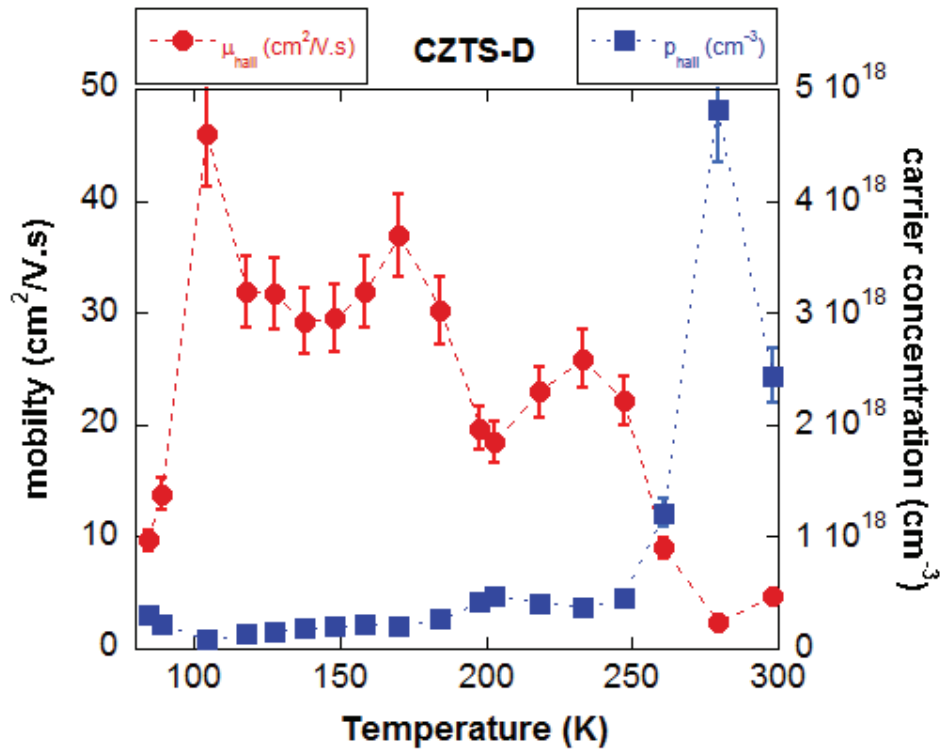
Figure 4.47. Variation of carrier concentration and Hall mobilities with temperature for CZTS-D

For CZTS-D sample, the hole mobility value was found as 4.74 cm^2/V.s and the hole carrier concentration value was measured 2.44×10^{18} cm^{-3} at room temperature. The hole mobility dramatically decreases and carrier concentration increases with the increase in temperature were shown at Figure 4.47.

In Figure 4.48 (a), the hole mobility value is 182 cm^2/V.s and the hole carrier concentration value is 1.03×10^{20} cm^{-3} at room temperature for CZTS-E 1st layer. Moreover, the hole mobility lowest value was found as 0.04 cm^2/V.s and the hole carrier concentration highest value was measured 2.83×10^{20} cm^{-3} at room temperature for CZTS-E. The hole mobility dramatically decreases after 150 K and carrier concentration increases with the increase in temperature were shown at Figure 4.48 (b).
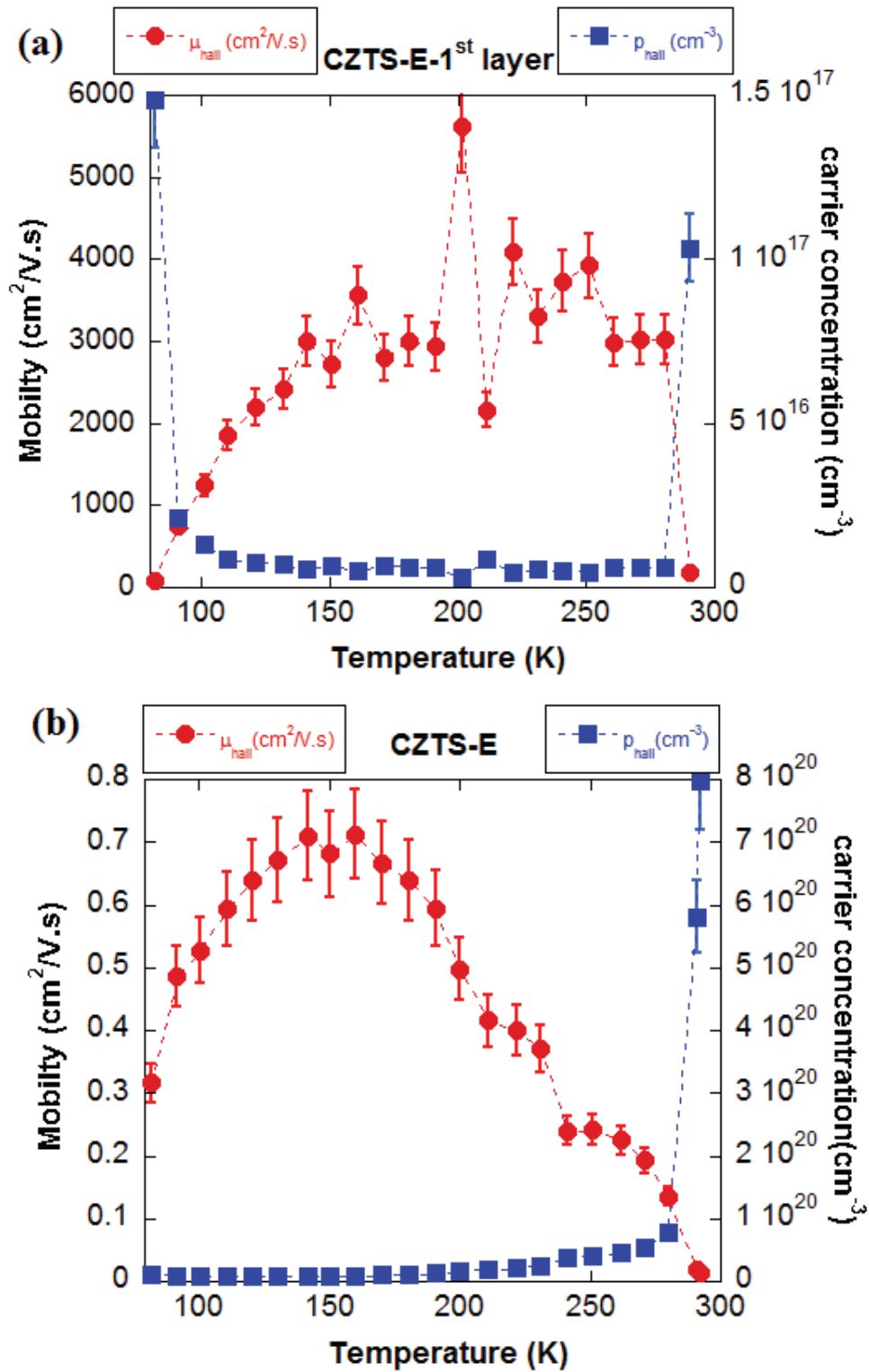
Figure 4.48. Variation of carrier concentration and Hall mobilities with temperature for (a) CZTS-E-1st layer (b) CZTS-E

According to using the Hall effect card for Hall effect measurement, due to noise, natural warming after cooled cryostat and the selection of high or low resistivity, some errors can occur. The following Figure 4.49 shows the deviation in values for Variation

of carrier concentration and hall mobilities depend on temperature measurements of results taken at two times for CZTS-E.
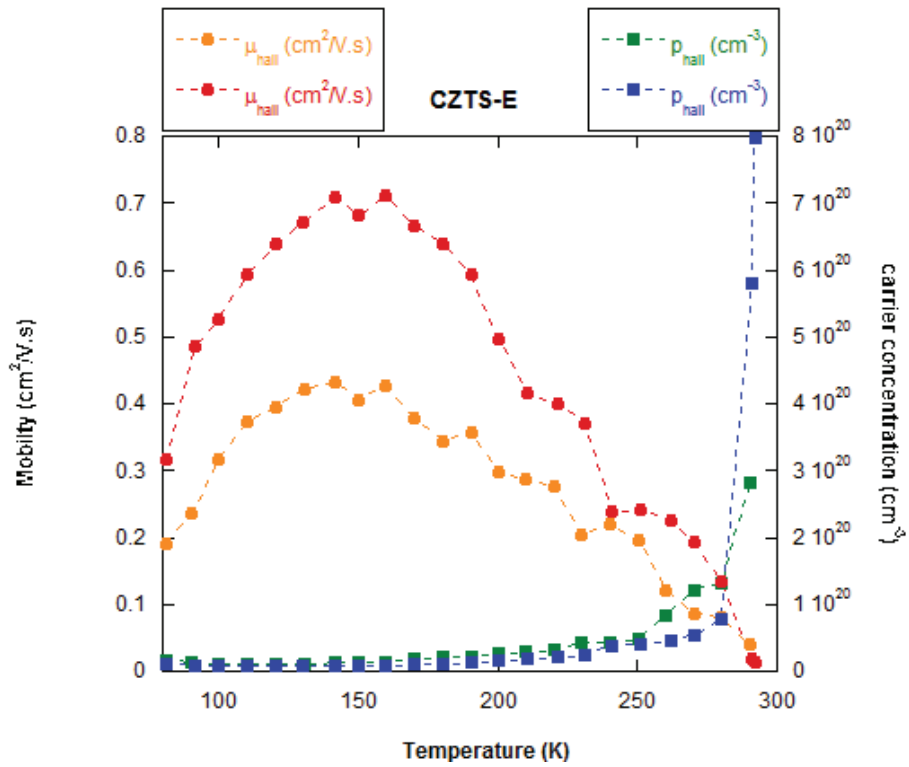
Figure 4.49. Variation of carrier concentration and Hall mobilities with temperature measurements of results taken at different times for CZTS-E

Table 4.10. The hole mobility, carrier concentration, resistivity and Hall coefficient values for CZTS samples at room temperature

Samples	CZTS-A	CZTS-B	CZTS-C	CZTS-D	CZTS-E	CZTS-E 1st layer
Mobility (cm²/V.s)	5.74	10.04	0.32	4.74	0.04	182
Carrier Concentration (cm⁻³)	1.04×10^{19}	2.12×10^{19}	5.62×10^{16}	2.44×10^{18}	2.83×10^{20}	1.03×10^{17}
Resistivity (Ω.cm)	0.09	0.02	182	0.53	0.56	0.33
Hall Coefficient (cm³/C)	2.34	0.29	111.18	2.56	0.02	60.48

Table 4.10 shows electrical properties for all samples at room temperature. According to results on the table, CZTS-D and E demonstrate nearly same parameter for

resistivity value but different mobility and carrier concentration values. For CZTS- E, double layer stacking improved carrier concentration. It is know that if the carrier concentration increase, the hall mobility decrease.

According to Grimm–Sommerfeld rule, in compound semiconductors lattice defects of "cation vacancy" and "anion interstitial" may form acceptor states, resulting in p-type conductivity semiconductors at room temperature. In CZTS and CZTSe (Cu_2–II–IV–VI_4), the p-type conductivity is attributed to the antisite defect center of Cu_{Zn} (Cu_{II}), that is to say a Cu atom at the Zn (group II) site, in CZTS and CZTSe (Cu_2–II–IV–VI_4) quaternaries (Chen et al., 2010a; Chen et al., 2010b; Nagoya et al., 2010). Since Cu has a valence of 1^+ and Zn (group II) has a valence of 2^+, such antisite defect center of Cu_{Zn} (Cu_{II}) can be computation the origin of p-type conductivity. Therefore, we can say that p-type conductivity can increase because of Cu vacancy.

When we consider the scattering mechanism (for instance, ionized impurity scattering, neutral impurity scattering, grain boundary scattering, lattice scattering, carrier scattering and optical phonon scattering, etc.), due to the fact that carrier scattering at the grain or particle boundaries in polycrystalline or nanocrystalline sample generally greatly reduce carrier mobility. For this reason, we can also say that there is a direct proposition between crystalline size and carrier mobility. Moreover, one or more of them, which are grain boundary, lattice, ionized impurity, dislocation scattering mechanisms, can limit mobility.

At low temperatures, carriers move more slowly, thus there is more time for them to interact with charged impurities. The changing mobility values depend on impurity on films. If impurity scattering increases with temperature decreases, the mobility decreases or the opposite state is possible. For p-type semiconductors, most of the free holes with temperature decreases are recaptured by the acceptors. The holes do not have enough thermal energy to be excited from the acceptor levels to valence band and the band conduction becomes less important, that is, hole hopping directly between the acceptor states in the impurity band will be the main contributor to the conduction mechanism (Ma et al., 2005; Miller and Abrahams, 1960).

CHAPTER 5

CONCLUSION

CZTS quaternary semiconductor is a promising candidate solar absorber material as an alternative. Because CZTS is non-toxic, earth abundance, low cost and environmental friendly material. Moreover, theoretical efficiency value is more than 30%. Although this value is higher, current efficiency value is lower than other thin film absorber layer such as CIGS, CdTe and CIS. For these materials, there are restriction on the usage of heavy metals such as Cd and, the limitation in supplies for In and Te. CZTS has been extensively examined as an alternative PV material due to its similarity in material properties with CIGS and relatively abundance of raw materials.

In this thesis, we studied growth and characterization of CZTS thin films grown by DC magnetron sputtering. Growing process occur under high vacuum condition that is among 10^{-6} Torr. And then, all samples were formed by sulfurization process at Ar and S atmosphere. Duration and temperature of sulfurization are critical parameters in the thermal process. So, we just tried different sulfurization duration time and investigated its effect on structural and electrical properties of samples. Hence, structural, optical characterization, temperature dependence electrical properties such as Hall effect and R-T measurements were done. Scanning Electron Microscopy (SEM), X-Ray Diffraction (XRD), Raman Analysis and Cryostat were used to characterize samples. Our aim was figure out effect of the temperature on film properties. Especially, we focused on electrical properties depend on temperature such as resistivity, hall coefficient, hole mobility and carrier concentration. van der Pauw method was used for these electrical measurement.

According to the morphological and structural analysis results, all samples were all Cu-poor and Zn-rich compared to stoichiometry, in general. The composition was generally uniform within the precursors, only the surfaces showed some gradients due to Sn-rich regions. Large grain size is a desired quality for better conductivity in an absorber layer of a solar cell. For this reason, we can consider the best sample CZTS-D for good crystallinity and large grain size. Even though it was not possible to assign all XRD peaks to certain phases, crystalline phases were found kesterite structure. To conclusion was that the precursors tend to loose Sn at high temperature when sulfurization process. EDX

measurements showed tin-sulfide conglomerates at some region on surfaces. Briefly, Sn-based binary secondary phase formations were shown all analysis results. For the results of Raman analysis, we recommend that the main peak at about 334 cm^{-1} can be attributed to the disordered kesterite which can also be close to the stannite structure. Nevertheless, we do not know the exact atomic displacements and cannot exactly say which kind of ordering is present in the studied CZTS polycrystalline structures.

In the optical properties of using samples at our study, the optical band gap energy of the films was determined as about 1.56 eV. Even though, we have seen that this value is consistent with the literature, band gap values of all samples were different. These reasons could that a fundamental structural rearrangement of the CZTS phase between stannite and kesterite, which have been shown theoretically to have different band gaps. And also, this state could be concerned the possibility that a Sn-containing secondary phase was responsible for the optical properties of the film.

In this work, we focused on measuring the temperature dependence of the Hall effect. Hall effect measurements were carried out at 80-300 K under a about 1640 G magnetic field in the van der Pauw geometry. When the electrical properties are examined, all samples showed p-type semiconductor behavior. Based on the Hall effect measurement at 300 K, the resistivity, carrier concentration and hole mobility of the CZTS samples are estimated as listed a table. The resistivity value is 0.02-182 Ω.cm. The carrier concentration is equal to 10^{16}–10^{20} cm^{-3}, the hole mobility is 0.04–10.04 cm^2 /V. s. The low grain boundary, defect density and defects like secondary phases should be responsible for the high hole mobility and resistivity observed in the CZTS samples.

The CZTS solar cell device was produced on Mo coated SLG. The maximum solar cell efficiency value was estimated almost 1.15%.

CZTS-E had the lowest mobility and the highest carrier concentration value among the others. The sample was grown as double stacking. We can fabricate pure or nearly pure kesterite CZTS structure with this stacking. Consequently, the less impurity the better electrical properties are shown.

Finally, the Hall measurements should also be determined at high temperature to compare with theoretical calculations. To increase the solar cell efficiency, electrical properties should be improved. Since the electrical properties are very important for solar cell efficiency value. For that too, the absorber layer should be dense structure, no void and without secondary phases.

REFERENCES

Altamura Giovanni, 2014. Development of CZTSSe thin lms based solar cells, PhD Thesis, Material chemistry. Université Joseph-Fourier - Grenoble I.

Altosaar M., Raudoja J., Timmo K., Danilson M., Grossberg M., Krustok J. and Mellikov E.. $Cu_2Zn_{1-x}Cd_xSn(Se_{1-y}S_y)_4$ solid solutions as absorber materials for solar cells. Physica Status Solidi (a), 205 (2008), 167–170.

Chan C. P., Lam H. and Surya C., Preparation of Cu_2ZnSnS_4 films by electrodeposition using ionic liquids, Sol. Energy Mater. Sol. Cells, 94 (2010), 207-211.

Chen S., Gong X. G., Walsh A., and Wei S.-H., "Defect physics of the kesterite thin-film solar cell absorber Cu_2ZnSnS_4," Appl. Phys. Lett. 96 (2010a), 021902-1–3

Chen S., Yang J.-H., Gong X. G., Walsh A., and Wei S.-H., "Intrinsic point defects and complexes in the quaternary kesterite semiconductor Cu_2ZnSnS_4," Phys. Rev. B 81 (2010b), 245204-1–10

Cheng, A-J., M. Manno, A. Khare, C. Leighton, S. A. Campbell, E. S. Aydil, Imaging and Phase Identification of Cu_2ZnSnS_4 Thin Films Using Confocal Raman Spectroscopy, Journal of Vacuum Science & Technology A: Vacuum, Surfaces, and Films 29 (5) (2011), 051203.

Dumcenco D. and Huang Y.-S., The vibrational properties study of kesterite Cu_2ZnSnS_4 single crystals by using polarization dependent Raman spectroscopy, Opt. Mater. 35 (2013), 419–425

Eren B., Marot L., Gunzburger G., P.O. Renault, Th. Glatzel, R. Steiner and E. Meyer. Hydrogen-induced buckling of gold films. J. Phys. D: Appl. Phys., 47 (2014), 025302

Ericson T., Kubart T., Scragg J. J. and Platzer-Björkman C.. Reactive sputtering of precursors for Cu_2ZnSnS_4 thin film solar cells. Thin Solid Films, 520(0) (2012), 7093–7099.

Fernandes P. A., Salomé P. M. P. and Cunha A. F. da. A study of ternary Cu_2SnS_3 and Cu_3SnS_4 thin films prepared by sulfurizing stacked metal precursors. Journal of Physics D: Applied Physics, 43(21) (2010) 215403.

Fernandes P. A., Salomé P. M. P. and Cunha A. F. da. Growth and Raman scattering characterization of Cu_2ZnSnS_4 thin films. Thin Solid Films, 517(7) (2009), 2519–2523

First Solar Press Release, First solar sets world record for CdTe solar cell efficiency. 〈http://investor.firstsolar.com/releases.cfm〉 (accessed February 25, 2014).

Flammersberger, Hendrik. 2010. "Experimental Study of Cu_2ZnSnS_4 Thin Films for Solar Cells",M.Sc. Thesis, Uppsala University

Friedlmeier T. A. M.. 2001, Multinary Compounds and Alloys for Thin-Film Solar Cells: Cu_2ZnSnS_4 and $Cu(In,Ga)(S,Se)_2$. PhD thesis, Stuttgart University, Institut für Physikalische Elektronik.

Grossberg M., Krustok J., Raudoja J., Raadik T., The role of structural properties on deep defect states in Cu_2ZnSnS_4 studied by photoluminescence spectroscopy, Appl. Phys. Lett. 101 (2012), 102102

Gürel Tanju, Sevik Cem and Çağın Tahir, Characterization of vibrational and mechanical properties of quaternary compounds Cu_2ZnSnS_4 and $Cu_2ZnSnSe_4$ in kesterite and stannite structures, Physical Review B 84 (2011), 205201

Ito K. and Nakazawa T., Electrical and optical properties of stannite type quaternary semiconductor thin films, Jpn. J. Appl. Phys., 27(11) (1988), 2094-97.

Ito Kentaro, Copper Zinc Tin Sulfide-Based Thin-Film Solar Cells, 2015

Jackson Philip, Hariskos Dimitrios, Wuerz Roland, Wischmann Wiltraud, Powalla Michael, Compositional investigation of potassium doped $Cu(In,Ga)Se_2$ solar cells with efficiencies up to 20.8%, Phys. Status Solidi Rapid Research Letter, 8, 3 (2014), 209–292

Jimbo Kazuo, R. Kimura, T. Kamimura, S. Yamada, W. S. Maw, H. Araki, K. Oishi, H. Katagiri, Cu_2ZnSnS_4-Type Thin Film Solar Cells Using Abundant Materials, Thin Solid Films, 515 (15) (2007), 5997–99.

Katagiri H., Saitoh K., Washio T., Shinohara H., Kurumadani T., Miyajima S., Development of thin film solar cell based on Cu_2ZnSnS_4 thin films, Sol. Energy Mater. Sol. Cells 65 (1) (2001), 141–148

Kato T., Hiroi H., Sakai N., Muraoka S., Sugimoto H., Charaterization of front and back interfaces on Cu_2ZnSnS_4 thin-film solar cells, 27th EU PVSEC, 10.4229/27th EUPVSEC2012-3CO.4.2 (2012) 2236-2239

Khare Ankur, Himmetoglu Burak, Johnson Melissa, Norris David J., Cococcioni Matteo, and Aydil Eray S., Calculation of the lattice dynamics and Raman spectra of copper zinc tin chalcogenides and comparison to experiments, Journal of Applied Physics, 111 (2012), 083707

King R. R., Fetzer C. M., Colter P. C., Edmondson K. M., Ermer J. H., Cotal H. L., Yoon H., Stovrides A. P., Kinsey G., Krut D. D., Karam N. H., 29th IEEE Photovoltaic Specialists Conference, (2002), 776-781

Lewerenz, H.-J.; Jungblut, H.: Photovoltaik - Grundlagen und Anwendungen. Springer-Verlag, (1995)

Li X., Wang D., Du Q., Liu W., Jiang G., Zhu C., Growth of Cu_2ZnSnS_4 thin films by sulfurization of co-sputtered metallic precursors, Adv. Mater. Res. 418–420 (2012), 67–71.

Liu F., Li Y., Zhang K., Wang B., Yan C., Lai Y., Zhang Z., Li J. and Liu Y., In situ growth of Cu_2ZnSnS_4 thin films by reactive magnetron co-sputtering, Sol. Energy Mater. Sol. Cells, 94(12) (2010), 2431-34.

Luque A., S.H., ed. Handbook of photovoltaic science and engineering. 2003, John Wiley & Sons, Ltd.

Ma J., Wang Y., Ji F., Yu X. and Ma H., UV–violet photoluminescence emitted from SnO_2:Sb thin films at different temperature, Mater. Lett. 59 (2005), 2142

Miller A. and Abrahams E., Impurity Conduction at Low Concentrations, Phys. Rev. 120 (1960), 745

Mitzi, David B, Gunawan O., Todorov T. K, Wang K., Guha S., Solar Energy Materials & Solar Cells The Path towards a High-Performance Solution-Processed Kesterite Solar Cell $, 95 (2011), 1421–36.

Mkavi E. M., Ibrahim K., Ali M. K. M., and Mohamed A. S., Dependence of Copper Concentration on the Properties of Cu2ZnSnS4 Thin Films Prepared by Electrochemical Method, In t. J. Electrochem. Sci., 8 (2013), 359-368.

Morales-Acevedo Arturo, Solar Cells - Research and Application Perspectives, InTech, 2013

Nagoya A., Asahi R., Wahl R., and Kresse G., "Defect formation and phase stability of Cu_2ZnSnS_4 photovoltaic material," Phys. Rev. B 81 (2010), 113202-1–4

Nilsen W.G., Raman Spectrum of Cubic ZnS, Phys. Rev., 182 (1969), 838

Olekseyuk, I. D., Dudchak I. V., Piskach L. V., Phase Equilibria in the Cu_2S-ZnS-SnS$_2$ System, Journal of Alloys and Compounds, 368 (2004), 135-143.

Olgar M.A., Klaer J., Mainz R., Levcenco S., Just J., Bacaksiz E. Unold, T., Effect of precursor stacking order and sulfurization temperature on compositional homogeneity of CZTS thin films, Thin Solid Films 615 (2016), 402–408

Pankove J.I., Optical Processes in Semiconductors, Dover Inc., New York, 1975.

Parenteau Martin and Carlone Cosmo, Influence of temperature and pressure on the electronic transitions in SnS and SnSe semiconductors, Phys. Rev. B, 41 (1990), 5227

Price L. S., Parkin I. P., Hardy A. M. E. and Clark R. J. H.. Atmospheric Pressure Chemical Vapor Deposition of Tin Sulfides (SnS, Sn_2S_3 and SnS_2) on Glass. Chem. Mater., 11(7), (1999) 1792-1799

Rai G. D., Non-Conventional energy sources. New Delhi: Khanna, 2002

Rajeshmon V. G., Sudha Kartha C., Vijayakumar K. P., Sanjeeviraja C., Abe T. and Kashiwaba Y., Role of precursor solution in controlling the opto-electronic properties of spray pyrolysed Cu_2ZnSnS_4 thin films, Sol. Energy, 85 (2011), 249-255.

Riha S.C., Parkinson B.A., Prieto A.L., Solution-based synthesis and characterization of Cu_2ZnSnS_4 nanocrystals, J. AM. CHEM. SOC. 131 (2009), 12054-12055.

Schorr, S., Structural Aspects of Adamantine like Multinary Chalcogenides, Thin Solid Films 515 (15) (2007), 5985–91.

Scragg, Jonathan James. 2010. "Studies of Cu2ZnSnS4 Films Prepared by Sulfurisation of Electrodeposited Precursors.

Shockley W. and Queisser H. J., Detailed Balance Limit of Efficiency of p-n Junction Solar Cells, J. Appl. Phys. 32 (1961), 510-519

Tanusevski A. and Poelman Dirk, Optical and photoconductive properties of SnS thin films prepared by electron beam evaporation, Solar Energy Materials and Solar Cells, 80(3) (2003), 297-303

Tuna O., Selamet Y., Aygun G. and Ozyuzer L., High quality ITO this films grown by DC and RF sputtering without oxygen, J. Phys. D: Appl. Phys., 43 (2010), 055402.

Walsh A., Chen S., Wei S.-H. and Gong X.-G., Kesterite thin-film solar cells: Advances in materials modelling of Cu_2ZnSnS_4, Adv. Energy Mater., 2(4) (2012), 400–409.

Wang W., Winkler M.T., Gunawan O., Gokmen T., Todorov T.K. , Zhu Y., Mitzi D.B., Device characteristics of CZTSSe thin film solar cells with 12.6% efficiency, Adv. Energy Mater. 4 (2014) 1301465

Wurfel Peter. Physics of Solar Cells: From Principles to New Concepts. Weinheim: Wiley, 2005

Xinkun W., Wei L., Shuying C., Yunfeng L. and Hongjie J., Photoelectric properties of Cu2ZnSnS4 thin films deposited by thermal evaporation, J.Semicond., 33 (2012), 022002.

Yazici Sebnem, Olgar M. Ali, Akca F. Gulsah, Kurt Metin, Aygun Gulnur, Yanmaz Ekrem and Ozyuzer Lutfi, Growth of Cu_2ZnSnS_4 absorber layer on flexible metallic substrates for thin film solar cell applications, Thin Solid Films, 589 (2015), 563–573

Zhao J., Jeon I., Yi Q., Jain M., Rummeli M. H., Song P., Zou G. and Matsuo Y., An efficient organic solvent-free solution-processing strategy for high-mobility metal chalcogenide film growth, Green Chem., 19 (2017), 946-951